Title

Into the Abyss: Assessing Meridional Heat Transport, Turbulent Mixing and the Effects of Warming in the Deep Ocean

Author

Lele, Ratnaksha

Publication Date

2023

Peer reviewed|Thesis/dissertation

UNIVERSITY OF CALIFORNIA SAN DIEGO

Into the Abyss: Assessing Meridional Heat Transport, Turbulent Mixing and the Effects of Warming in the Deep Ocean

A dissertation submitted in partial satisfaction of the
requirements for the degree Doctor of Philosophy

in

Oceanography

by

Ratnaksha Lele

Committee in charge:

Sarah G. Purkey, Chair
Sarah T. Gille
Jan P Kleissl
Jennifer A. MacKinnon
Matthew R. Mazloff
Lynne D. Talley

2023

The Dissertation of Ratnaksha Lele is approved, and it is acceptable in quality and form for publication on microfilm and electronically.

University of California San Diego

2023

DEDICATION

To my Parents for their unwavering
supporting throughout my life...

... and to some expected and other
serendipitous events that bring me to this juncture.

EPIGRAPH

The sea, the great unifier is man's only hope.
Now, as never before the old phrase has a literal meaning:
We are all in the same boat

Jacques Yves Cousteau

TABLE OF CONTENTS

LIST OF FIGURES

LIST OF TABLES

ACKNOWLEDGEMENTS

First and foremost, I would like to express my deepest gratitude to my advisor, Sarah Purkey. Her guidance and mentorship through the years have truly helped me grow as a scientist and as a person. I have undoubtedly appreciated the freedom to pursue different avenues of research, generous feedback on streamlining and focusing those scientific questions into tangible outcomes and support for me to explore career development opportunities outside of the academic realm. Our open and clear communication, regular weekly check-ins made it smoothly sailing over the occasional turbulent waters of navigating Graduate study, and life in general over the past few years.

I would like to thank my quasi-co-advisor Jennifer MacKinnon, for being a limitless source of knowledge on all things turbulent mixing and for giving this thesis crucial bearings when it seemed forlorn and adrift at sea. I am grateful to Jonathan Nash for his jovial outlook and much needed guidance on interpreting χ-Pod data and for trusting me work on χ-Pod deployment on the P06 cruise in 2017. I would not have guessed in 2017 that the χ-Pod data we collected would underpin large chunks of this dissertation. Sincere thanks to my committee members Sarah Gille, Matt Mazloff, Lynne Talley and Jan Kleissl for being an invaluable resource and providing additional guidance to me on this work. Additional thanks to Maddie Hamann, Lynne Talley and Bob Pickart for involving me in incredible opportunities at sea to witness first-hand and forever drilling into my psyche the vast undertaking it is- *observing* the Ocean. Special thanks to John Toole and Sylvia Cole at WHOI for introducing the world of observational physical oceanography to a clueless mechanical engineering major from India, safe to say- changed the trajectory of my life.

Thank you to the administrative staff at Scripps- Gilbert, Shelley, Tomomi for constantly working on behalf of the students, helping us navigate departmental requirements and coordinating funding resources. Special mention to the UCSD's Research Cluster for providing excellent hassle-free cloud compute resources for major compute-intensive portions of this work. Additionally thanks to NASA FINESST and NSF-OCE grants for providing funding resources to accomplish

this work.

I would like to thank my family and and friends for support during this period. I am grateful to the 2016 PO and CS cohort- Jacob, Jessica, Julia, Luke, Margaret, Mike, Curly Mike and Will a.k.a The Yaks for the collective learning, shenanigans and camaraderie during our first year and years since. My parents and my sister for being my true anchor and support system from ten thousand miles away. Lastly my wife, Ariel for being my ball of joy and our two dogs Casper and Cusco for being the best bubbies one could ever have.

Chapter Two, in full, is a reprint of the material as it appears in the Journal of Physical Oceanography, 2021. R. Lele, S. G. Purkey, J. D. Nash, J. A. MacKinnon, A. M. Thurnherr, C. B. Whalen, S. Mecking, G. Voet and L. D. Talley(2022) Abyssal Heat Budget in the Southwest Pacific Basin *Journal of Physical Oceanography*, 51(11):3317–3333, 2021
The dissertation author was the primary investigator and author of this paper.

Chapter Three, is currently being prepared for submission for publication of the material. J.N. Nash, R. Lele, S.G. Purkey and J. A. MacKinnon, Ocean Mixing Measured by Fast-Response Thermistors on Traditional Shipboard CTDs: Sources of Uncertainty and Bias (In Preparation). The dissertation author was a co-investigator and co-author of this material and contributed to Sections 3, 4 5 and 6.

Chapter Four, in full, is a reprint of the material submitted to the Journal of Geophysical Research: Oceans. R. Lele, S.G. Purkey, J.A. MacKinnon and J.D. Nash. Global Patterns of Bias in Ocean Mixing Parameterization Identified Through Unsupervised Machine Learning *Journal of Geophysical Research: Oceans*. The dissertation author was the primary investigator and author of this material.

Chapter Five, is currently being prepared for submission for publication of the material. R. Lele and S.G. Purkey, A Full-Depth Sea Level Rise Budget in the Southwest Pacific Basin using Deep Argo (In Preparation, Preliminary Title). The dissertation author was the primary investigator and author of this material.

VITA

2016	Bachelor of Technology in Mechanical Engineering, VIT University, India
2018	Master of Science in Oceanography, University of California San Diego
2023	Doctor of Philosophy in Oceanography, University of California San Diego

PUBLICATIONS

Ratnaksha Lele , Sarah G. Purkey, Jonathan D. Nash, Jennifer A. MacKinnon, Andreas M. Thurnherr, Caitlin B. Whalen, Sabine Mecking, Gunnar Voet and Lynne D. Talley "Abyssal Heat Budget in the Southwest Pacific Basin " Journal of Physical Oceanography, 51(11):3317–3333, 2021, https://doi.org/10.1175/JPO-D-21-0045.1

Sylvia T Cole, John M Toole, Ratnaksha Lele, Mary-Louise Timmermans, Shawn G Gallaher, Timothy P Stanton, William J Shaw, Byongjun Hwang, Ted Maksym, Jeremy P Wilkinson, Macarena Ortiz, Hans Graber, Luc Rainville, Alek A Petty, Sinéad L Farrell, Jackie A Richter-Menge, Christian Haas "Ice and ocean velocity in the Arctic marginal ice zone: Ice roughness and momentum transfer " Elementa: Science of the Anthropocene, 5:55, 2017, https://doi.org/10.1525/elementa.241

ABSTRACT OF THE DISSERTATION

Into the Abyss: Assessing Meridional Heat Transport, Turbulent Mixing and the Effects of Warming in the Deep Ocean

by

Ratnaksha Lele

Doctor of Philosophy in Oceanography

University of California San Diego, 2023

Sarah G. Purkey, Chair

The ocean's overturning circulation is a large-scale conveyor belt responsible for transporting mass, heat and tracers around the global oceans driven primarily by heat and density gradients between different water masses. Two distinct cells of the global MOC have been proposed based upon observations guided by physical constraints, the upper cell (u-MOC) associated with waters sinking to lower to mid-depth in the northern reaches of the North Atlantic Ocean, and the lower or bottom cell (b-MOC) which is linked to the sinking of waters formed around Antarctica to abyssal depths. The deep and abyssal oceans are responsible for absorbing a significant fraction of the global heat budget. Processes that govern the sequestration of heat and carbon in the

deep ocean and its redistribution into the interior ocean have huge consequences for the large scale circulation, sea level rise, and the global climate system as a whole. Studying the abyssal ocean depths below 2000 m has historically been limited due to the paucity of high-quality observational data. Only in recent decades have advances in autonomous float technologies, satellite remote sensing, and regular ship-based observational programs begun to reduce the existing data deficit. This thesis uses data from decades of ship-based observations, thousands of profiles from autonomous Argo floats worldwide, and other novel instrumentation to understand and characterize some of the fundamental questions regarding the contemporaneous changes in the abyssal ocean and its impact on climate.

In Chapter 2, we construct a heat budget in the Southwest Pacific Basin and utilize ship-based observations gathered over three decades to understand the changes in the large-scale abyssal circulation in the basin. We further calculate the estimates of turbulent mixing in the basin, reconciling them using three different techniques of backing out the turbulent diffusivities in the basin. In Chapter 3, we demonstrate a methodology deploying a novel turbulence profiler called χ-Pod and develop a method to reduce spikes in the error-prone data. In Chapter 4, we use a novel unsupervised machine learning technique to characterize different internal wave spectra observed in the ocean, using observations from 15 repeat hydrographic sections around the globe. Lastly, in Chapter 5 we quantify the rate of sea level rise and the contribution of the warming in the abyssal ocean in the Southwest Pacific Basin using data from 4954 profiles from Deep Argo floats. These chapters provide a detailed view of critical processes in the abyssal ocean measured by novel instrumentation to better understand the role of the oceans in a changing global climate.

Chapter 1

Introduction

The meridional overturning circulation (MOC) of the ocean is a global heat engine associated with large-scale transport of water, heat, carbon, nutrients, and other tracers poleward from the tropics, and the equatorward return flow of colder dense water formed near the polar ice-caps. Two distinct cells of the global MOC have been proposed based on observations and guided by physical constraints (Wunsch & Ferrari, 2004; Talley et al., 2011; Marshall & Speer, 2012), the upper cell (u-MOC) is associated with waters sinking to lower to mid-depth in the northern reaches of the North Atlantic ocean, and the lower or bottom cell (b-MOC) which is linked to sinking of waters formed around Antarctica to abyssal depths (Figure 1.1). Furthermore, for the circulation to be sustained and to complete the cycle, these dense cold water masses must eventually upwell to the surface. The bulk of the upwelling in the ocean is accomplished through processes in the ocean that result in turbulent mixing of these cold waters with warmer waters thereby causing gain in its buoyancy (Munk, 1966; Bryan, 1987; Munk & Wunsch, 1998a; Wunsch & Ferrari, 2004).

The role of turbulent mixing in the dynamics of the global MOC, its sources and sinks as well the magnitude and geographical distribution has been long pondered and is a fundamental question in the field of physical oceanography. The strength of this large-scale diapycnal transformation of waters is often expressed in terms of the diapcynal diffusivity κ (m^2/s) and the rate of dissipation of turbulent kinetic energy ϵ (W/kg). From a 1-D idealized

perspective computed using an advective-diffusive balance, Munk (1966) postulated that the observed stratification in the deep ocean required an average diapycnal diffusivity $K = \mathrm{O}(10^{-4}$ $\mathrm{m^2\ s^{-1}})$ for waters to upwell through the main thermocline, given the rate of deep and bottom water being produced in the northern and southern polar regions, later corroborated by idealized numerical experiments, heat budgets and inverse estimates (Bryan, 1987; Lumpkin & Speer, 2007; Macdonald et al., 2009). However, measurements in the open-ocean thermocline from microstructure instrumentation and tracer release experiments have revealed broad-scale mixing rates weaker by an order of magnitude $K = \mathrm{O}(10^{-5}\ \mathrm{m^2\ s^{-1}})$ (Gregg, 1987; Ledwell et al., 2000, 1998a; Kunze et al., 2006a), than those suggested by the idealized theoretical frameworks.

This paradox of the "missing mixing" is largely reconciled in the modern two-cell global MOC framework in which abyssal waters in both hemispheres (Figure 1.1, blue arrows) are largely upwelled to mid-depths (~3000 m) by vigorous turbulence, primarily driven by breaking internal waves, upon which they are drawn to the surface in a largely adiabatic pathway into the Southern Ocean's Antarctic Circumpolar Current (ACC) region (Figure 1.1) (Toggweiler, 1994; Lumpkin & Speer, 2007; Marshall & Speer, 2012). The upwelling is induced by northward Ekman transport from westerly winds in the ACC region and enables a pathway from the interior abyssal ocean to the surface facilitating the communication of abyssal waters to return to the surface, thus eliminating the constraints posed by unobserved large thermocline diffusivities (Sverdrup, 1933; Doos & Webb, 1994; Toggweiler & Samuels, 1995, 1998; Talley, 2013).

While observational evidence of weak mixing in the stratified interior away from boundaries and topography is robust, measurements from decades of microstructure and tracer release experiments have shown that turbulent mixing two to three orders of magnitude higher than the interior ocean occurs in the abyssal ocean near rough topography, seamounts and, hydraulically controlled passages and canyons (Lueck & Mudge, 2009; Ferron et al., 1998; Kunze & Toole, 1997; St. Laurent et al., 2001; Polzin et al., 1997; Roemmich et al., 1996) driven primarily by dissipation of turbulent kinetic energy through non-linear internal wave-wave interaction (Garrett & Munk, 1979). Although these observations indicate that these regions of

elevated turbulence are highly localized and spatially and temporally variable, mixing plays a critical role in enabling water-mass transformation in the deep and abyssal ocean, but also in balancing the kinetic energy budget of the ocean. Global power input to the internal wave field is derived primarily from winds, tides and geostrophic currents of roughly 3-3.5 TW (Wunsch & Ferrari, 2004). The dissipation resulting from internal wave-driven turbulence acts as a sink to balance the energy budget with tidally generated internal waves contributing roughly 1 TW (Egbert & Ray, 2000; Nycander, 2005), near-inertial dissipation from time-varying wind stress input of roughly between 0.3-1.4 TW (M. H. Alford, 2003; Jiang et al., 2005; Simmons & Alford, 2012; Nikurashin & Ferrari, 2010) and finally dissipation related to internal lee wave generation of roughly 0.2-0.7 TW (Nikurashin & Ferrari, 2011; Scott et al., 2011; Wright et al., 2014; Nikurashin et al., 2014) (Figure 1.2). Ultimately, complex and convoluted processes governing the generation, propagation and dissipation of internal waves shape the overall distribution of the turbulent mixing globally (Kunze et al., 2006a; Whalen, Talley, & MacKinnon, 2012; Waterhouse et al., 2014a; Kunze, 2017b), drive the MOC, shaping many of its characteristics and in turn the global climate system. The modeled magnitude and structure of the MOC is tightly coupled with the horizontal and vertical distribution of mixing, an indication of its importance for setting the MOC's observed properties (Oka & Niwa, 2013; Melet et al., 2016; Hieronymus et al., 2019).

The distribution and magnitude of internal wave-driven mixing in the ocean has broader effects on the climate system. Parameterizations to capture spatio-temporal variability of internal wave-driven mixing are being developed (MacKinnon et al., 2017a) since they it is not captured adequately in current global ocean and climate models. Studies report that even small perturbations in the magnitude or distribution of the diffusivity in global models can lead to substantial changes in the air-sea fluxes, stratification and circulation in the models (Melet et al., 2016; Hieronymus et al., 2019). Models are highly sensitive to mixing as it alters spatial distributions of fundamental properties of the ocean such as temperature and salinity and thereby induces changes in density, stratification and large-scale circulation and dynamics (Tatebe et al., 2018; Zhu & Zhang, 2019; Jochum et al., 2013; Stanley & Saenko, 2014). Further, this can

lead to downstream effects of variations in sea surface temperatures (SSTs), mixed layer depth, and air-sea fluxes in the model representations (Melet et al., 2013a, 2014; Zhu & Zhang, 2019; Jochum et al., 2013) and thereby perturbing effects on air temperatures, sea-ice concentrations, atmospheric circulation, and precipitation. These substantial effects of the representation of internal wave-driven mixing in the ocean are critical not only for understanding ocean circulation and dynamics but also have wide-ranging impacts for global climate models and accurate representation of the climate system and therefore are the next frontier in understanding and interpreting the importance of diapycnal mixing in the ocean.

The role of the deep and abyssal ocean is at the forefront of inquiry in observing, understanding and modeling the impacts of global atmospheric radiative imbalance (global warming) resulting from an increase in greenhouse gas concentrations (Meyer et al, 2014). Over the past few decades the oceans have absorbed between 80% - 90% of the excess heat gain from the radiative imbalance with about 10% sequestered into the abyssal ocean below 4000 m (Levitus et al., 2000; Purkey & Johnson, 2010; von Schuckmann et al., 2022), primarily due to its large mass and high heat capacity, and therefore, dominates the heat inventory of the Earth (Von Schuckmann et al., 2016; Cheng et al., 2017, 2019). (Figure 1.3). While high-quality observations of the abyssal ocean are greatly limited in spatio-temporal coverage and are mostly derived from decadal or semi-decadal hydrographic observations in various basins, the recent rise in earth observations from remote sensing through satellite altimetry (Cazenave et al., 2009; Dieng et al., 2015; Llovel & Lee, 2015) and gravimetry (Tapley et al., 2004; Chambers, 2006; Böning et al., 2008; Chambers & Willis, 2010; Tapley et al., 2019) as well as from autonomous floats profiling the ocean called Argo and Deep Argo (Wong et al., 2020) have greatly added to the inventory of data to better understand the ocean's role in a warming climate.

Basins adjacent to Antarctica and tied to Antarctic Bottom Water formation regions have shown signs of consistently higher warming rates than most ocean basins to the north (Purkey & Johnson, 2010; Desbruyères et al., 2016; Purkey et al., 2019; G. C. Johnson et al., 2020; G. C. Johnson, 2022). The warming seen in the AABW formation region is exacerbated through

positive feedback by causing changes in the rate of formation of AABW through increased meltwater from ice shelves around Antarctica and has a potential to slow down to the point of collapse in future climate scenarios (Gunn et al., 2023; Lago & England, 2019; Li et al., 2023) and leading to further atmospheric warming (Liu et al., 2020). This has critical implications for global sea-level rise projections through thermosteric effects as well as sea-level rise due to additional melt from polar ice-caps and glaciers from the warming oceans (Cazenave et al., 2018; Trenberth & Fasullo, 2009; Purkey & Johnson, 2012a; Cazenave et al., 2018). Estimates of the altimetry-based global mean sea level have shown that sea level has risen at an average rate of 3.1 $\pm$ 0.3 mm yr^{-1} and has been accelerating recently in the satellite altimeter era since 1993 (Church & White, 2006; Nerem et al., 2018). Since direct observation of heat content changes in the deep ocean below 2000 m are extremely sparse, most methods have relied on indirect methods utilizing altimetry along with its constituent components (thermosteric from Argo observations and gravimetry-based ocean mass) to constrain this elusive piece of the puzzle. However, the errors remain too large to provide robust estimates of the deep ocean contributions to sea level rise and ocean heat content (Von Schuckmann et al., 2016; G. C. Johnson & Chambers, 2013; Watson et al., 2015; Dieng et al., 2015).

This thesis, consisting of 4 main chapters, is a scientific foray into some of the aforementioned larger outstanding questions concerning large-scale circulation of the deep and abyssal ocean. The inquiry is probed primarily with the use of high-quality observations obtained from ship-based surveys, autonomous floats in the ocean and from remote sensing. *Chapter 2* begins with an investigation into the bottom limb of the overturning circulation (b-MOC) in the Southwest Pacific Basin, which is driven primarily through the northward flow of cold waters formed in the Southern Ocean and diffusion-driven upwelling from oceanic turbulence, both of which are difficult to measure and quantify accurately. This chapter aims to reconcile different methods of measuring the overturning in a large ocean basin by 1) inferring the mixing required to sustain the overturning using long-term observations of inflow and outflow heat fluxes from a time-dependent heat budget and 2) direct/indirect observations of mixing within the basin. While

our results show the consistency of the basin-averaged mixing estimates from several different methods, this study also highlights the need to make sustained oceanic observations of mixing and circulation to further reduce uncertainty in the estimates.

Chapter 3 is centered around methodological development and testing of novel instrumentation to estimate the turbulent dissipation rate ϵ by obtaining measurements of the dissipation rate of temperature variance χ from fast-response FP07 thermistors mounted on a standard shipboard conductivity, temperature and depth (CTD) rosette, called the CTD-χpod (J. N. Moum & Nash, 2009). Until recently direct observation of deep-ocean mixing has required special free-falling profiling instruments, which was one of the reasons for sparse mixing observation in the ocean (Waterhouse et al., 2014a). This chapter describes a relatively new technique for obtaining ocean mixing by measuring very small-scale temperature fluctuations during traditional CTD operation. From data gathered on over 200 profiles in the SW Pacific basin along the P06 transect, we develop a methodology to accurately filter out spurious, noisy and contaminated turbulence data- a routine occurrence when sampling on unstable profiling platforms tethered to rocking oceanic vessels. The method is shown to not be significantly biased, which provides support for making continued observations within the global repeat hydrography programs, data from which are utilized in both Chapters 2 and 4.

In *Chapter 4*, we employ a novel framework using unsupervised machine learning to investigate multi-dimensional coherent patterns and covariances in oceanic properties used to predict the rate of turbulent mixing from internal waves in the ocean. As an alternative to obtaining in-situ measurements of mixing such as described in Chapter 3, simplified parameterized models (finescale parameterizations) to estimate the rate of mixing are widely used by incorporating relatively easily collected oceanic properties such as temperature and velocity as inputs (Polzin et al., 1995). However, inaccuracies in predictions by these simplified models arise when certain assumptions in the model are violated. In this study, by incorporating data collected from a global suite of ship-based observations from 15 hydrographic sections, we use a data-driven approach to identify the spatial distribution of two distinct regions in the ocean where large biases

in the predictions by the simplified models are possible. These patterns exhibit distinct spatial patterns globally which are likely a result of the underlying circulation and dynamics unresolved in these finescale parameterizations of mixing (e.g., Waterman, Polzin, Naveira Garabato, Sheen, Forryan, Garabato, et al., 2014; Takahashi & Hibiya, 2018). Extending this approach, future studies could potentially identify the underlying causes of such disparities to further improve models of turbulent mixing in the ocean.

Finally, in *Chapter 5* we investigate the contemporary warming in the deep and abyssal ocean and quantify its contribution to the steric component of the sea level budget using data from autonomous floats (Deep Argo) in the Southwest Pacific Basin. Distinct from the "core" Argo fleet of floats which sample only the top 2000 m of the ocean, Deep Argo floats are capable of sampling the full ocean depth ($\sim$ 6000 m) and provide extremely valuable bi-monthly sampling of primary oceanographic properties of roughly 50% of the ocean's volume, otherwise impossible without ship-based observations. Using data gathered from 56 floats and roughly 5000 full-depth profiles between 2014 and the Present in the Southwest Pacific Basin, we find large warming signals in the abyssal ocean primarily concentrated below 3000 m in depth with the rate of the warming maximal between 4500 m and 5500 m. We quantify that the warming ocean in this basin is contributing on average roughly 1.3 millimeters per decade to the sea level rise in the basin. Finally, we use this new estimate of the full-depth steric sea level signal to provide better closure in the sea level budget. At a relatively high resolution of $5^o \times 5^o$, the incorporation of the deep steric component observed by Deep Argo along robust estimates from the upper ocean from "core" Argo (Roemmich & Gilson, 2009), results in an improvement of roughly 5% in explaining sea level variability in a limited region of the Southwest Pacific basin.

These four chapters in their totality explore a wide range of observational datasets gathered from a variety of instrumentation. They incorporate a span of analysis frameworks and encompasses a wide range of scales and inter-woven processes in the MOC. In *Chapter 2* we use hydrographic observations in the Southwest Pacific basin to constrain estimates of turbulent mixing with a heat budget and compare it to inferred and in-situ measurements from finescale

parameterizations and CTD-χpods. *Chapter 3* tests a methodology to effectively deploy sensitive temperature microstructure instrumentation onboard a CTD rosette, quantifies biases in the measurements, and develops an approach to flag, filter and quality-control spurious measurements of turbulence. We use unsupervised machine learning to combine hydrographic data and finescale parameterizations of turbulent mixing to gain insight into the spatial characteristics of biases in these paramterizations along 15 global sections in *Chapter 4*. Lastly considering the accumulation of heat in the deep ocean, *Chapter 5* quantifies the role of steric contribution of the deep ocean below 2000 m in the overall sea level budget in the Southwest Pacific basin using data from Deep Argo floats. Given the lack of high quality in-situ observations of the deep and abyssal oceans, investigating these questions and expanding on the results obtained from these studies is critical to further our understanding of the ocean's role in today's rapidly changing climate system.

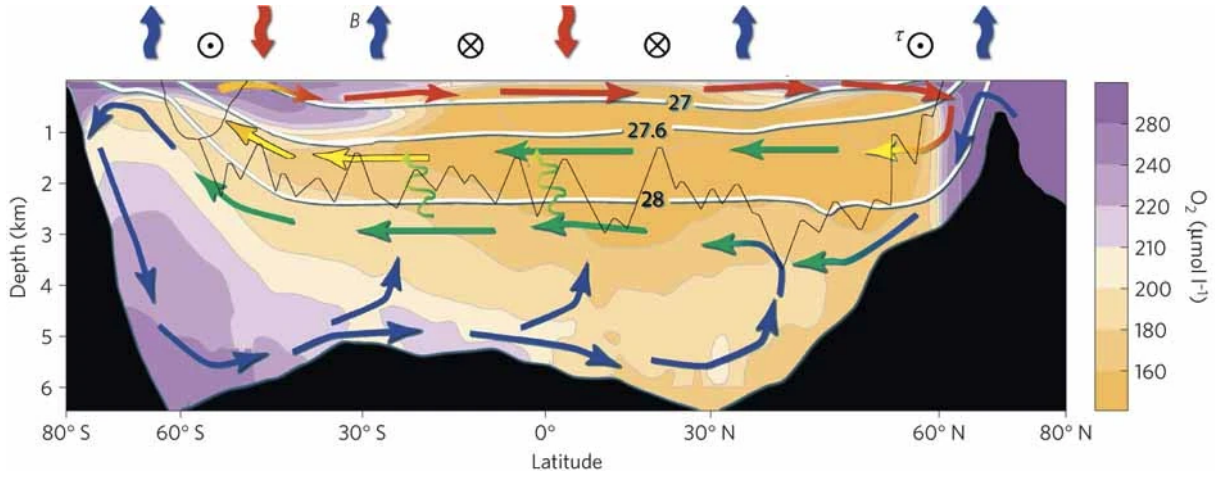

Figure 1.1. A schematic diagram of the Upper Cell and Lower Cell of the global MOC in a zonal mean framework formed in the northern and southern polar seas. The bottom MOC (b-MOC) cell (blue arrows) shows formation of Antarctic Bottom Water (AABW) near Antarctica, sinking to abyssal depths and upwelling and entrainment into mid-depths. In the Northern Hemisphere, formation of North Atlantic Deep Water (NADW) and southward movement (green arrows) are shown where the entrained AABW and NADW are mixed together and rise to the surface along isopycnals in a largely adiabatically driven upwelling in the Southern Ocean's Antarctic Circulpolar Current (ACC) region. Average neutral density (γ_n) of the corresponding layers is labeled and colored contours corresponding to dissolved oxygen concentration relating the relative age of the waters are also shown. Figure from Marshall & Speer (2012).

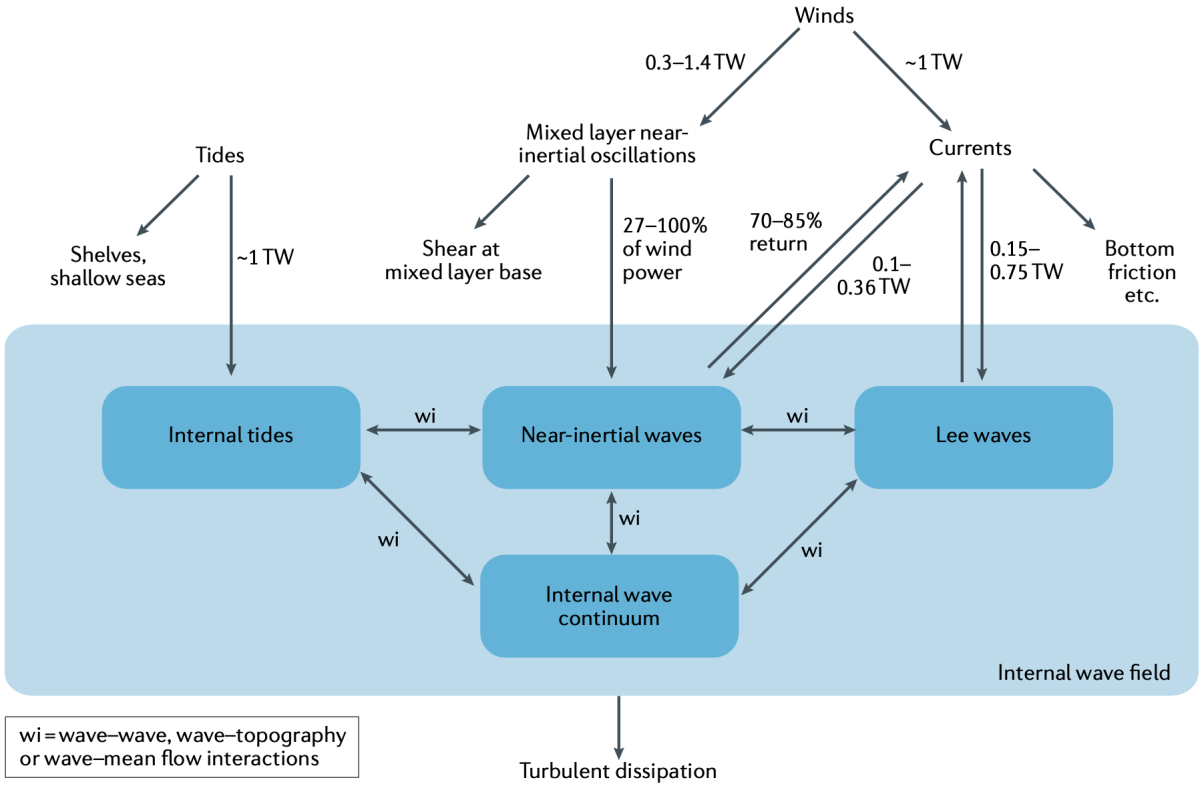

Figure 1.2. A schematic showing the simplified global internal wave energy budget. Included are the sources of internal wave energy and the pathways of energy transfer until turbulent dissipation. Figure from Whalen et al. (2020).

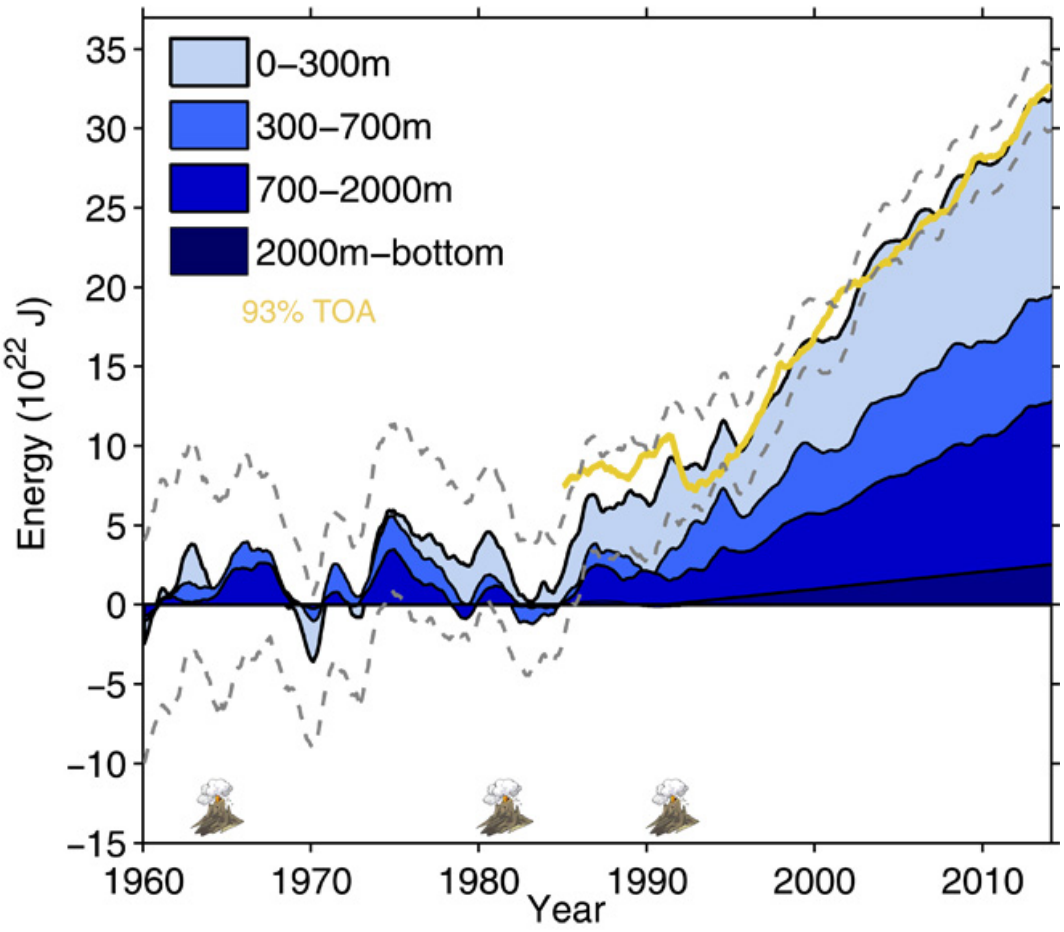

Figure 1.3. The energy budgets are relative to the 1958–1962 base period. The integrated net radiative imbalance from Allan et al. (65) estimated from the TOA is included in yellow and is multiplied by 0.93 to be comparable with the ocean energy budget. The TOA radiation is adjusted to the value of OHC within 2013–2014. The dashed gray lines encompass the 95% confidence interval. Figure from Cheng et al. (2017).

Chapter 2

Abyssal Heat Budget in the Southwest Pacific Basin

Abstract

The abyssal Southwest Pacific Basin has warmed significantly between 1992-2017, consistent with warming along the bottom limb of the meridional overturning circulation seen throughout the global oceans. Here we present a framework for assessing the abyssal heat budget that includes the time-dependent unsteady effects of decadal warming and direct and indirect estimates of diapycnal mixing from microscale temperature measurements and finescale parameterizations. The unsteady terms estimated from the decadal warming rate are shown to be within a factor of 3 of the steady state terms in the abyssal heat budget for the coldest portion of the water column and therefore, cannot be ignored. We show that a reduction in the lateral heat flux for the coldest temperature classes compensated by an increase in warmer waters advected into the basin has important implications for the heat balance and diffusive heat fluxes in the basin. Finally, vertical diffusive heat fluxes are estimated in different ways: using the newly available CTD-mounted microscale temperature measurements, a finescale strain parameterization, and a vertical kinetic energy parameterization from data along the P06 transect along 32.5°S. The unsteady-state abyssal heat budget for the basin shows closure within error estimates, demonstrating that (i) unsteady terms have become consequential for the heat balance in the isotherms closest to the ocean bottom and (ii) direct and indirect estimates from full depth GO-SHIP hydrographic transects averaged over similarly large spatial and temporal scales can capture the basin-averaged abyssal mixing needed to close the deep overturning circulation.

2.1 Introduction

The meridional overturning circulation (MOC) regulates global climate through the exchange and distribution of heat, carbon and nutrients throughout the global oceans (Meehl et al., 2006). The overturning structure and strength of the deep and bottom cells of the MOC are set by the balance between surface buoyancy loss at high latitudes that produces deep water, and diapycnal mixing throughout the global ocean driven by internal wave breaking and geothermal heating (Nikurashin & Ferrari, 2013; Talley, 2013; MacKinnon et al., 2017a; Lumpkin & Speer, 2007; Marshall & Speer, 2012).

In the Southwest Pacific (SWP) Basin, the bottom limb of the MOC is fed by a mix of Antarctic Bottom Water (AABW), originating primarily from the Antarctic continental shelf, and Lower Circumpolar Deep Water (LCDW), primarily made up of deep waters originating from the North Atlantic that have been modified in the Antarctic Circumpolar Current. The pathways of bottom water in the SWP Basin have been relatively well observed, with this modified AABW mixture entering the SWP Basin through an intensified deep western boundary current (DWBC) south of New Zealand that continues north along the Tonga-Kermadec Ridge (Reid, 1997; Wijffels et al., 2001; Whitworth et al., 1999). The majority of the flow bottlenecks through the Samoan Passage before filling the entirety of deep North Pacific Ocean (e.g., Roemmich et al., 1996; Voet et al., 2016).

The inflow of cold deep water is largely balanced by vertical transfer of heat from above through diapycnal mixing. Direct observations of diapycnal mixing in the deep ocean are sparse in space and time, despite their critical importance in understanding large-scale ocean dynamics and closing the ocean heat budget (Waterhouse et al., 2014a; MacKinnon et al., 2017a). Observations from a pilot program to equip CTD rosettes used on decadally-occupied GO-SHIP repeat hydrographic sections with χ-pods – self-contained instruments that measure temperature microstructure and package motion (see Nash et al. submitted) – offer a new means for estimating deep-ocean mixing. Here we use these CTD χ-pod data collected on the Global

Ocean Ship-based Hydrographic Investigations Program (GO-SHIP) hydrographic transect P06 to estimate the vertical heat transfer from turbulent mixing into the abyssal ocean.

When assessing the deep ocean heat budget, it is important to note that the deep ocean is not currently in steady state, but instead has been warming significantly in recent decades. Below 2000 m, the global oceans have warmed at a rate equivalent to a downward heat flux of 0.065 ± 0.040 Wm^{-2} over the entire surface of the Earth between the 1990s and 2000s, with the strongest warming rates found in the Southern Ocean closest to AABW formation sites (Purkey & Johnson, 2010; Kouketsu, Doi, et al., 2011; Desbruyères et al., 2016). This warming is likely being driven by a slowdown in AABW production and communicated globally on decadal time scales by deep planetary waves (Fukasawa et al., 2004; Kouketsu et al., 2009; Masuda et al., 2010; Purkey & Johnson, 2012a). In the SWP Basin, the deep waters below 4000 m have warmed at a mean rate of 1.26 ± 0.19 °mC yr^{-1} between the 1990s and 2010s, with a possible stronger warming rate of 2.0°mC yr^{-1} between the 2000s and 2010s (Purkey et al., 2019). Furthermore, the new Deep Argo array suggests an even larger warming rate of 3°mC yr^{-1} between 2014-2019 (G. C. Johnson et al., 2019).

Here, we present an in-depth analysis of the unsteady-state abyssal heat budget of the Northern half of the SWP Basin between 1992 and 2017 in order to assess our ability to directly measure all aspects of the local MOC. Using available ship-based hydrographic, mooring and Deep Argo data within the SWP Basin (Section 2.2), we quantify all terms in the heat budget of the abyssal ocean to test our current ability to directly monitor the processes controlling the MOC (Section 2.3). Geostrophic velocity is calculated from four repeat hydrography sections along 32.5°S in the South Pacific and from velocity measurements in the Samoan Passage (Roemmich et al., 1996; Rudnick, 1997; Voet et al., 2016) to estimate advective heat flux and compare this to new estimates of vertical heat flux from both microscale temperature measurements and finescale parameterizations of eddy diffusivity (κ). In Section 2.4 we compare results of the full unsteady-state heat budget which accounts for the observed warming in the abyssal SWP basin to a simple steady state heat budget calculation by ignoring the temporal variation which has

previously been incorporated in various studies (e.g., WHITEHEAD & WORTHINGTON, 1982; Morris et al., 2001; Heywood et al., 2002). Lastly, in the framework of the abyssal heat budget, we discuss how changes in advective and diapycnal heat fluxes could drive abyssal warming by changing the MOC, and how well we can currently monitor and quantify each component (Section 2.5).

2.2 Data

We use CTD, Lowered Acoustic Doppler Current Profiler (LADCP), and microscale temperature data collected during one or more of the four occupations of the zonal repeat hydrographic line P06 across the Pacific at 32.5°S (Figure 2.1). The line was first occupied in 1992 as part of the World Ocean Circulation Experiment (WOCE) and repeated in 2003, 2009, and 2017, first under the Climate Variability and Predictability (CLIVAR) program and later under the Global Ocean-Based Hydrographic Investigations Program (GO-SHIP). Stations sample from the surface to within 10-20 m of the ocean bottom or to 6000 m depth and are nominally spaced roughly every 55 km along the section, with closer spacing in regions of rough topography, trenches and boundary currents.

All four occupations include 2 dbar-binned Temperature (T), Salinity (S) and Pressure (P) data with accuracy to 0.002°C, 0.002 PSS-78 and 3 dbar, respectively (Joyce 1991). Salinity data were calibrated to the International Association of the Physical Sciences of the Oceans (IAPSO) standard seawater, and any batch-to-batch offsets between standards were applied (Kawano et al., 2006). All temperature measurements were converted to the International Temperature Scale (ITS-90) and salinity is given in Practical Salinity Scale 1978 (PSS-78). Potential Temperature (θ) and neutral density (γ_n) are calculated following Jackett & McDougall (1997).

LADCP data are available for the 2003, 2009 and 2017 occupations, but the 2003 and 2009 data are characterized by high noise owing to only having a downward looking 300kHz LADCP instrument, while the 2017 occupation had both an upward and downward looking

LADCP. For this reason, only the LADCP data from the 2017 occupation are used for the finescale parameterization.

In addition, microstructure measurements of the dissipation rate of temperature variance (χ) were made along the 2017 occupation of the P06 section (Nash et al., submitted). Two χ-pods, self-contained instruments that measure microscale temperature fluctuations using fast-response FP07 thermistors sampled at 100 Hz (J. N. Moum & Nash, 2009) were mounted on the outer ring of the CTD rosette and extended above the top of the cage to avoid influence of the wake generated by the CTD package. Data were also collected from a downward-looking χ-pod mounted near the CTD and LADCP head; however measurements from this sensor were often contaminated (possibly by wake shed from the LADCP head), so are not used here.

Eight months of full depth CTD profiles collected from three Deep Argo floats (Figure 2.1) deployed along the P06 line in 2017 at 168°W (float ID:6030, WMO ID: 5902528), 160°W (float ID:6031, WMO ID: 5902529), and 152°W (float ID:6032, WMO ID: 5905161) are also used to assess temporal variability of the geostrophic flow over the abyssal plain. Each float took full depth profiles every 10 days, sampling continuously in the upper 500 dbar and discretely every 2 dbar to 50 dbar between 500 dbar and the bottom. As seen in Figure 2.1, the floats considered in this study (Figure 2.1, pink lines) stayed close to the initial deployment location along P06 over the course of the eight-month period, hence the measurement records are considered as stationary time series here.

Finally, time series of heat and volume transport through the Samoan Passage based on moored observations between 1992-1994 (Rudnick, 1997) and 2012-2014 (Voet et al., 2016) are used to estimate deep meridional outflow from the North SWP Basin.

2.3 Methods

We formulate a heat budget for the North SWP Basin. We distinguish the North SWP Basin from the rest of the SWP Basin as the geographical region north of 32.5°S. The cold waters

considered here are isolated zonally by the Tonga-Kermadec Ridge along its western boundary and the East Pacific Rise along its eastern flank. The eastern and western sides of the deep basin are bounded by the 4000-m isobath running along the East Pacific Rise and Tonga-Kermadec Ridge, the northern edge bounded at 10°S by Samoan Passage and the P31 zonal hydrographic section and southern end along the GO-SHIP P06 hydrographic section along 32.5°S (Figure 2.1).

The unsteady-state abyssal heat budget follows Morris et al. (2001) (Figure 2.2). In this framework, the time rate of change of heat (Q) and the divergence of advective heat fluxes into a defined volume are balanced by a diffusive heat flux and geothermal heating:

$$\frac{\partial Q}{\partial t} + \nabla \cdot (Q\vec{\mathbf{u}}) = \nabla \cdot (\kappa \nabla Q) \tag{2.1}$$

where $\vec{\mathbf{u}}$ is the 3 dimensional velocity field and κ is the eddy diffusivity. The first term in Equation 2.1, the unsteady term (Q_t), is often neglected in abyssal heat budgets; however we will show this term to be leading order in the coldest temperature classes (that are bounded by isotherms) and therefore include it here. This term represents the observed abyssal warming.

The heat budget calculation includes 41 isothermal layers (hereafter, layers) (0.6°C to 1°C in increments of 0.01°C) within the deep basin. The spatial extent of each layer is defined by the climatological position of a top and bottom bounding isotherm from the 1 degree × 1 degree WOCE hydrographic climatology (Gouretski & Koltermann, 2004). First, the WOCE climatology potential temperature-pressure profiles are interpolated onto a fine (0.01°C) isotherm grid between 0.6°C to 1°C. The volume (V) and top and bottom isotherm surface area S_{top} and S_{btm} of each layer can then be calculated by integrating spatially over the North SWP Basin. Note that the volume (V) and top and bottom surface areas of each layer (i) represent the "mean" volume and surface area of each of 41 layers over the climatological period of 1980-2004 (Gouretski & Koltermann, 2004). While V is constant in time, below we will introduce a V′ term (defined as dV/dt) in the heat budget calculation reflecting the observed temporal changes in the

volume of each layer in the basin (Figure 2.2).

We integrate Equation 2.1 over the layer volume (V) and expand the terms by applying divergence theorem to get

$$\iiint_V \frac{\partial Q}{\partial t}\,dx\,dy\,dz + \oiint_S (Q\vec{\mathbf{u}})\cdot\hat{\mathbf{n}}\,dS = \iint_{S_{top}} \kappa\frac{\partial Q}{\partial z}dS - \iint_{S_{btm}} \kappa\frac{\partial Q}{\partial z}dS - Q_g \tag{2.2}$$

The last term in equation 2.2 is the geothermal heating term (Q_g) and is defined as Q_g = Q_o × FA × SA, a mean abyssal geothermal heat flux (Q_o; 0.05 W/m^2) times the fraction area (FA) of the total bottom bounding surface area (SA) of each defined layer in contact with the bottom. We then separate velocities in equation (2.2) into the vertical velocities (w) and the horizontal inflow velocity along P06 (u_{P06}) and outflow velocity through Samoan Passage (u_{sp}).

$$\int_V \frac{\partial Q}{\partial t}\,dx\,dy\,dz + \left(\int_{S_{south}} -Qu_{\mathrm{P06}}dS + \int_{S_{north}} Qu_{\mathrm{SP}}dS + \int_{S_{top}} QW_{adv}dS - \int_{S_{btm}} QW_{adv}dS\right) = \int_{S_{top}} \kappa\frac{\partial Q}{\partial z}\,dS - \int_{S_{btm}} \kappa\frac{\partial Q}{\partial z}\,dS - Q_g \tag{2.3}$$

Using Leibniz rule for the unsteady term in (2.3) whose integral bounds are changing in time, we can transform using

$$\frac{d}{dt}\int_{z_1(t)}^{z_2(t)} Q(z,t)\,dz = Q(z_2,t)\frac{\partial z_2(t)}{\partial t} - Q(z_1,t)\frac{\partial z_1(t)}{\partial t} + \int_{z_1}^{z_2}\frac{\partial Q}{\partial t}dz \tag{2.4}$$

where z_2 and z_1 are top and bottom bounds of the layer in the vertical. We use the transformation in Equation (2.4) to split the unsteady term into 3 different terms and substitute into Equation 2.3 to get

$$\begin{aligned}\frac{d}{dt}\int_V Q\,dx\,dy\,dz - \int_{S_{top}} Q(z_2,t)\frac{\partial z}{\partial t}dS + \int_{S_{btm}} Q(z_1,t)\frac{\partial z}{\partial t}dS + \\ \left(\int_{S_{south}} -Qu_{P06}dS + \int_{S_{north}} Qu_{SP}dS + \int_{S_{top}} Qw_{adv}dS - \int_{S_{btm}} Qw_{adv}dS\right) + Q_g = \\ \int_{S_{top}} \kappa\frac{\partial Q}{\partial z}\,dS - \int_{S_{btm}} \kappa\frac{\partial Q}{\partial z}\,dS.\end{aligned} \tag{2.5}$$

Further, we replace heat (Q) with $\rho c_p \bar{\theta}$ where ρ, c_p, $\bar{\theta}$ are the density, heat capacity and average potential temperature of the layer respectively. Using mass conservation we replace $W_{adv_{top}} = (U_{P06} - U_{SP})_i$ and $W_{adv_{btm}} = (U_{P06} - U_{SP})_{i-1}$ corresponding to upward advection through the top and bottom isotherms respectively, where W and U now represent volume transports instead of velocities. Further, on solving the integral in term 1 on the LHS of Equation 2.5, it is transformed into the time derivative of the product of two functions that represent the average temperature and average volume of the layer respectively, where the change in the volume is due to the movement of the top and bottom bounding isotherms of the layer i.e. $\rho c_p \frac{d}{dt}\bar{\theta}(t) \times V(t)$. We use the product rule for derivatives to get

$$\begin{aligned}V\rho c_p\frac{d\bar{\theta}_i}{dt} + \rho c_p\bar{\theta}_i\left(\left.\frac{dz}{dt}\right|_{top} S_{top} - \left.\frac{dz}{dt}\right|_{btm} S_{btm}\right) \\ -\rho c_p\theta_{top}\left.\frac{\partial z}{\partial t}\right|_{top} S_{top} + \rho c_p\theta_{btm}\left.\frac{\partial z}{\partial t}\right|_{btm} S_{btm} \\ -\rho c_p\bar{\theta}_i U_{P06} + \rho c_p\bar{\theta}_i U_{SP} + \rho c_p\theta_{top}(U_{P06} - U_{SP})_i - \rho c_p\theta_{btm}(U_{P06} - U_{SP})_{i-1} + Q_g = \\ \int_{S_{top}} \rho c_p\kappa\frac{\partial\theta}{\partial z}\,dS - \int_{S_{btm}} \rho c_p\kappa\frac{\partial\theta}{\partial z}\,dS.\end{aligned} \tag{2.6}$$

We split Term 2 in Equation 2.6 into two terms as follows

$$V\rho c_p \frac{d\bar{\theta}_i}{dt} + \rho c_p \frac{dz}{dt}\Big|_{top}(\bar{\theta}_i - \theta_{top})S_{top} - \rho c_p \frac{dz}{dt}\Big|_{btm}(\bar{\theta}_i - \theta_{btm})S_{btm} -$$
$$\rho c_p \bar{\theta}_i U_{P06} + \rho c_p \bar{\theta}_i U_{SP} + \rho c_p \theta_{top}(U_{P06} - U_{SP})_i - \rho c_p \theta_{btm}(U_{P06} - U_{SP})_{i-1} + Q_g = \tag{2.7}$$
$$\int_{S_{top}} \rho c_p \kappa \frac{\partial \theta}{\partial z}\, dS - \int_{S_{btm}} \rho c_p \kappa \frac{\partial \theta}{\partial z}\, dS$$

We rearrange the unsteady terms in Equation 2.7 to get

$$V\rho c_p \frac{d\bar{\theta}_i}{dt} - \rho c_p \frac{dz}{dt}\Big|_{top}(\theta_{top} - \bar{\theta}_i)S_{top} - \rho c_p \frac{dz}{dt}\Big|_{btm}(\bar{\theta}_i - \theta_{btm})S_{btm} -$$
$$\rho c_p \bar{\theta}_i U_{P06} + \rho c_p \bar{\theta}_i U_{SP} + \rho c_p \theta_{top}(U_{P06} - U_{SP})_i - \rho c_p \theta_{btm}(U_{P06} - U_{SP})_{i-1} + Q_g = \tag{2.8}$$
$$\int_{S_{top}} \rho c_p \kappa \frac{\partial \theta}{\partial z}\, dS - \int_{S_{btm}} \rho c_p \kappa \frac{\partial \theta}{\partial z}\, dS.$$

Each term of the abyssal heat budget in Equation (2.8) can now be evaluated within the North SWP Basin from observational data. From left to right, the first three terms are unsteady terms representing the energy needed to change the mean temperature within each layer (Term 1; $V\rho c_p \frac{d\bar{\theta}_i}{dt}$) and the energy associated with increasing or decreasing the volume of water within each temperature class through the vertical heave of the upper or lower bounding isotherm (Terms 2 and 3; $\rho c_p \frac{dz}{dt}\big|_{top}(\theta_{top} - \bar{\theta}_i)S_{top}$ and $\rho c_p \frac{dz}{dt}\big|_{btm}(\bar{\theta}_i - \theta_{btm})S_{btm}$). Terms 4-7 of Equation 2.8 are simply the advective terms accounting for the loss or gain of energy through the horizontal inflow (term 4; $\rho c_p \bar{\theta}_i U_{P06}$; Section 2.32.3.2), horizontal outflow (Term 5; $\rho c_p \bar{\theta}_i U_{SP}$; Section2.32.3.3), and vertical upwelling (Terms 6 and 7), estimated using a combination of geostrophic flow from hydrography and Deep Argo floats and velocity data from moorings. The geothermal heating (Term 8; Q_g; Section2.32.3.5) is estimated assuming a constant heat flux proportional to the area of the isotherms in contact with the bottom across the abyssal plain. The sum of the left hand side (LHS) terms is calculated as the inferred vertical diffusive heat flux (Section 2.32.3.6). Calculated as a residual, this term consists of diapycnal mixing processes as well as contributions

from errors propagated from measurement error and other unresolved components in the LHS. We can then compare this to vertical diffusive heat fluxes estimated using κ derived from the strain-based parameterization (Gregg, 1989; Whalen, Talley, & MacKinnon, 2012), a VKE-based parameterization (Thurnherr et al., 2015a), and temperature microstructure measurements from χ-pods (J. N. Moum & Nash, 2009) (Section 2.32.3.7). Further partition of the right hand side (RHS) term into a decomposition consisting of gradients of diffusivity, stratification and isotherm area as has been done in some recent studies (e.g., Drake et al., 2020; Spingys et al., 2021) is not considered here as it deviates from the scope of this study.

2.3.1 Unsteady terms (Equation 2.8 Terms 1-3)

The time derivatives in the unsteady terms ($\frac{d\bar{\theta}}{dt}$ and $\frac{dz}{dt}$) are calculated using the linear trend in potential temperature, θ, and isotherm height, z, using measurements from the 4 occupations of P06 following Purkey & Johnson (2012a). The θ-depth profiles from the four occupations are interpolated onto a regularly spaced vertical and horizontal grid. At each horizontal grid point along the section, the θ-depth profile is also interpolated onto a regular spaced θ-grid and the isotherm height is calculated as the distance above the bottom along the section. Then, a linear trend in θ and isotherm height versus occupation date are found at each horizontal and vertical grid point. The along-section average of $\frac{d\theta}{dt}$ along isobars and $\frac{dz}{dt}$ along isotherms is calculated and assumed to represent the basin mean (see Purkey & Johnson (2012a) for more details).

2.3.2 Horizontal Heat Transports across P06 (Equation 2.8 Term 4)

The horizontal heat flux into the basin across P06 is calculated from the deep geostrophic volume transport estimated with corrected reference velocity from the LADCP (Hernández-Guerra & Talley, 2016) and the observed hydrographic properties along the 4 occupations of the section. First, geostrophic velocity is estimated between station pairs along P06 using CTD data linearly interpolated on a 20 m depth grid assuming a level of no motion at γ_n = 28.1 kg m^{-3}. In the South Pacific, γ_n = 28.1 kg m^{-3} roughly forms the boundary between southward

gyre return flow of lighter intermediate and thermocline waters and northward transport of the denser AABW/LCDW (Ganachaud & Wunsch, 2003).

A velocity correction for the level of no motion assumption at γ_n=28.1 kg m^{-3} was applied based on LADCP data for stations between 179°W and 160°W in the Deep Western Boundary current where the velocity is unlikely to be zero at γ_n = 28.1 kg m^{-3} (Whitworth et al., 1999; Hernández-Guerra & Talley, 2016). The correction was only applied to the 2003, 2009 and 2017 occupations of P06 owing to LADCP data availability. For each occupation, meridional LADCP velocities were linearly interpolated to the mid-point of station pairs and the mean and variance of the difference between the initial geostrophic velocity and LADCP velocity between depths of 2000 m and 5500 m are calculated. The mean offset is applied to all station pairs where the variance is below 0.07 cm^{2}s^{-2}. This variance cut off corresponds to where the geostrophic and LADCP velocity profiles were determined to be vertically consistent across all depths through visual inspection of the profiles.

The net geostrophic transport below deep isotherms into the North SWP Basin across 32.5°S is calculated by integrating geostrophic velocities (Figure 2.3) from west to east. To do this, the corrected geostrophic velocities are first linearly interpolated on to a regular potential temperature grid from 0.6°C up to 1°C in 0.01^{o}C layers and linearly interpolated onto an evenly spaced 0.1° longitude grid. Then, transport within each layer is integrated across the basin. The choice of the 1°C isotherm as the upper-bound corresponds roughly to γ_n = 28.1 kg m^{-3}, forming the boundary for the deep northward transport that flows through the Samoan Passage (e.g., Roemmich et al., 1996). For comparison, a similar calculation can be done by integrating the net transport below γ_n = 28.1 kg m^{-3} from the Tonga-Kermadec Ridge to 130°W for each year (Figure 2.4) of the P06 occupation. We use averaged mass transport estimates between 1992 and 2017 to estimate Term 4 in Equation 2.8 in the unsteady-state heat budget calculation.

To capture the variability in the integrated meridional transport across P06, we use guidance from previous estimates of mass transport variability in the Tonga-Kermadec Trench region between 178°W and 168°W, as well as observed mass transport variability from two

pairs of Deep Argo floats in the abyssal plain of the SWP Basin east of 168°W. Whitworth et al. (1999) estimated a DWBC transport variance of 59% from the mean transport below 3200 m from a mooring time series in the Tonga-Kermadec Ridge region. Inverse model estimates from Hernández-Guerra & Talley (2016) show transport variance in the DWBC below γ_n=28.1 between 25% and 48%. Other studies also show a similarly wide range of basin integrated northward transport across the P06 section (Wijffels et al., 2001; Mazloff et al., 2010). Since transport variability on interannual and shorter timescales is largely unknown along the P06 section and has been shown to vary greatly in the DWBC from prior estimates, a factor of 50% of the net LADCP-referenced geostrophic transports is applied to account for temporal variability within each temperature bin for each year between 178°W and 168°W in the DWBC region.

For assessing temporal variability of transport east of 168°W, the vertical profiles of temperature and salinity from three Deep Argo floats are interpolated vertically onto an evenly spaced 20 dbar vertical grid, and geostrophic transport between pairs of Deep Argo floats are calculated for pairs that surfaced within a week of each other for the period between October 2017 and June 2018. The temporal variance in the geostrophic transport over the 8-month time series is assumed to be representative of the expected variance over the full abyssal plain even though the floats did not fully cover the region. The geostrophic transport from the Deep Argo floats shows a 29% variation from the mean transport in the eight month period. Therefore, we apply a 29% variance on the mean geostrophic flow in all temperature classes between 0.6°C and 1°C east of 168°W to account for the variation of geostrophic transport in the abyssal plain region.

The net meridionally integrated transports below γ_n = 28.1 kg m^{-3} are within 1Sv for the four P06 occupations as well as within error of previously published estimates for the region (Whitworth et al., 1999; Wijffels et al., 2001; Hernández-Guerra & Talley, 2016). However, the application of transport time variances in the DWBC and the abyssal plain as a measure of the spread aims to account for potential differences in integrated transport resulting from choice of reference density level in calculating the geostrophic transport as well as other measurement errors and the overall variability in the circulation on mesoscale and longer timescale. We then

consider this range of integrated mass transport to calculate horizontal heat transports in each isotherms between 0.6°C and 1°C in the heat budget calculation of the residual estimates of diffusivity (Section 2.42.3.6).

2.3.3 Horizontal Heat Transports across Samoan Passage (Equation 2.8 Term 5)

To estimate heat fluxes out of the basin, the mean volume transport through the Samoan Passage is estimated using mooring data from 1992-1994 (Rudnick, 1997) and 2012-2014 (Voet et al., 2016). No significant reduction in volume transport was observed between the two moored arrays but the volume of water within the coldest isotherms has changed (Voet et al., 2016). Therefore, here we use the 2012-2014 mooring array heat outflow for the 2003, 2009 and 2017 budgets and the 1992-1994 heat outflow for the 1992 budget. Outflow volume transports were interpolated onto the same regular potential temperature grid used for the inflow across P06. To account for northward flow around the Manihiki Plateau, an additional net transport of 2.7 Sv is distributed within temperature classes between 0.8°C and 1°C and added to the budget calculation for all years following estimates from Roemmich et al. (1996). Our final estimates of diffusive heat fluxes and diffusivity for these temperature classes are not sensitive to this choice.

2.3.4 Vertical Advection (Equation 2.8 Terms 6-7)

Upward advection, or upwelling, through the top bounding isotherm for each layer is calculated by solving for w through conservation of mass. To conserve mass within each layer beginning at the bottom-most isotherm (0.6°C), the horizontal mass inflow and vertical advection through the bottom bounding isotherm has to be balanced by an equal horizontal outflow or vertical outflow through the top bounding isotherm, or a change in the layer volume.

2.3.5 Geothermal Heating (Equation 2.8 Term 8)

The geothermal heating term is calculated as the product of the total surface area of the isotherm in contact with the bottom in the basin and a constant deep ocean heat flux of

0.05 W m^{-2} (Hofmann & Maqueda, 2009). We determine the total surface area of each layer in the temperature grid in contact with the ocean bottom using the 1° latitude x 1° longitude climatological maps of the ocean bottom temperature (Gouretski & Koltermann, 2004)(Figure 2.1). The time dependence of top and bottom surface areas S_{top} and S_{btm} on the geothermal heating term is not taken into account in the study since the this term is orders of magnitude less than the other terms in Equation 2.8 (see Section 2.4) is ultimately negligible in comparison.

2.3.6 Residual Diffusive Heat Fluxes from Basin Heat Budget (Equation 2.8 RHS)

A mean basin-averaged diffusivity (κ) can be estimated from the diffusion term (Figure 2.5a) by summing the LHS of Equation 2.8. We estimate the basin-averaged diffusive heat flux and κ on each isotherm by solving Equation 2.8 using the surface area of bounding isotherm (S) and vertical temperature gradient $\frac{\partial\theta}{\partial z}$ derived from WOCE-era hydrographic climatology (Gouretski & Koltermann, 2004) (Figure 2.6). Upper and lower bounds on the basin-wide diffusivity estimates are made by propagating the transport temporal variability error of 50% (in the Tonga-Kermadec Ridge region) and 29% (in the abyssal plain) on mass flux along P06 and through the Samoan Passage for each layer in the heat budget (see Section 2.32.3.2).

2.3.7 Diffusive Heat Fluxes from in-situ Measurements and Parameterizations (Equation 2.8 RHS)

Vertical diffusive heat flux, turbulent dissipation rate (ϵ), and eddy-diffusivity (κ) for the basin are also estimated using a strain parameterization, a VKE based parameterization, and temperature microstructure profiles from χ-pods along P06.

Strain Based Finescale Parameterization

Finescale parameterizations provide indirect means of estimating turbulent mixing in the ocean. Shear and strain based parameterizations use internal wave-wave interaction theories to predict the downscale cascade of energy transfer from larger to smaller scales, resulting

in turbulence production from breaking internal waves (McComas & Müller, 1981). Vertical profiles of strain variances are calculated along the P06 section using ship-based CTD data to estimate the rate of turbulent dissipation (Kunze et al., 2006a; Whalen, Talley, & MacKinnon, 2012; Polzin et al., 2014a) (Figure 2.7a).

Strain variance $\langle \xi_z^2 \rangle$ is calculated by integrating the buoyancy-normalized spectra, starting integration at λ = 100 m, which is constrained by the segment length (200 m) and avoids longer wavelength contamination by background stratification (Kunze et al., 2006a), to between wavelengths of 10 m and 40 m, while also satisfying strain variance $\langle \xi_z^2 \rangle < 0.2$ to avoid underestimating the variance through oversaturation of the spectrum (Gargett, 1990). We do not employ the use of shear measurements for the shear-strain parameterization (Kunze et al., 2006a) in this study due to unusually high noise levels in the deep ocean shear measurements along this section. Therefore, we apply a constant ratio between shear and strain $R_\omega = 3$ excluding the mixed layer (see Whalen et al. (2015a) for details). Profiles of ϵ and κ are calculated at each CTD station along the section from 200-m half-overlapping segments in depth. The parameterization gives average estimates of diffusivity and kinetic energy dissipation from breaking internal waves over multiple wave periods and does not account for mixing processes in the boundary layer, hydraulic jumps, double diffusion or internal wave driven turbulence in regimes with significant wave-mean flow interaction (Waterman, Polzin, Naveira Garabato, Sheen, Forryan, Garabato, et al., 2014).

Vertical Kinetic Energy (VKE) Parameterization

In contrast to the shear and strain based methods, the single-parameter VKE parameterization (Thurnherr et al., 2015a) is based on an empirical relationship between dissipation of turbulent kinetic energy and the energy in high-frequency internal waves, which dominate vertical velocity in the interior ocean (e.g., Eriksen, 1978). Requiring no input beyond vertical velocity, the VKE scaling between internal-wave energy and dissipation is not consistent with the latitudinal dependence of the shear/strain methods. Based on the relatively limited application to

date, the VKE method does not seem to be affected by dataset specific biases that exceed a factor of 2 that have been reported to affect some applications of the shear/strain method (Polzin et al., 2014a; Thurnherr et al., 2015a).

Using LADCP velocity data, the vertical fluid velocity (w) is calculated following Thurnherr (2011) and Fourier transformed to obtain VKE spectra. The scaling between the VKE spectra and ϵ has been further described in the study by Thurnherr et al. (2015a). Estimates of ϵ and κ, the latter based on the Osborn (1980a) relationship $\kappa = \Gamma\epsilon/N^2$ with constant mixing efficiency $\Gamma = 0.2$ (Gregg et al., 2018) and buoyancy frequency N from CTD data, are calculated at each CTD station along the section and binned in 320-m half-overlapping segments vertically. Mean profiles and confidence intervals along P06 are computed in the same way as for the strain parameterization (see Section 2.3.7 Basin Mean Diffusivity Profiles below, Figure 2.7b).

CTD-mounted χ-pod Measurements

High wavenumber temperature gradient fluctuations dT'/dz measured by the χ-pods were obtained on each upcast and processed following the methods of Moum and Nash (2009) and Nash et al. (submitted) to compute the dissipation rate of the temperature variance χ:

$$\chi = 6D_T \int_0^\infty \Psi_{T_z}(k)dk \tag{2.9}$$

where D_T is the thermal diffusivity and Ψ_{T_z} is the wavenumber spectrum of temperature gradient fluctuations. In practice, Ψ_{T_z} is not fully resolved by FP07 thermistor measurements, so assumptions must be made about the shape of the spectrum to compute χ at moderate TKE dissipation rates. While Goto et al. (2018a) use a curve-fitting technique to determine χ from CTD-mounted sensors, this method requires that the spectral roll-off be resolved and is biased for $\epsilon > 10^{-8}$ W/kg. Instead we follow a procedure based on Moum and Nash (2009) that corrects for unresolved variance in 1-s long spectra by simultaneously determining the ϵ and χ that are consistent with the resolved part of Ψ_{T_z}. Details of the methodology are provided in Nash et

al. (submitted), who also outline a means for rejecting data contaminated by the CTD-rosette wake for profiles collected in moderate sea states and compare these estimates with those from a free-falling microstructure profiler to demonstrate that the method is not biased. Here we follow that methodology and use Osborn & Cox (1972a) to calculate the eddy diffusivity of heat κ_T

$$\kappa_T = \frac{\chi}{2\left(\overline{dT/dz}\right)^2}, \tag{2.10}$$

where $\overline{dT/dz}$ is the mean background temperature gradient computed over 10-m scales. The dissipation rate of kinetic energy is then calculated as

$$\epsilon = \frac{N^2 \chi}{2\Gamma\left(\overline{dT/dz}\right)^2} \tag{2.11}$$

where N^2 is the squared buoyancy frequency and Γ is the mixing efficiency, chosen to be a constant 0.2. Following Nash et al. (submitted), χ is computed in 1-s bins, data that are potentially contaminated by platform-induced noise are rejected, as are data in regions of very weak stratification where $\overline{dT/dz}$ is less than 10^{-4} K m^{-1}. Retained data are binned into 200-m half overlapping segments (Figure 2.7c).

Basin Mean Diffusivity Profiles

We calculate the basin mean diffusivity and 95% bootstrapped confidence intervals for each parameterization and χ-pod measurements. First, parameterized estimates of diffusivity along the P06 section along isotherm surfaces are converted to diffusive heat fluxes by multiplying the diffusivity by the local vertical temperature gradient for a given isotherm $\frac{d\theta}{dz}$, density (ρ) and specific heat (c_p). We then take the mean along isotherms to determine the basin mean diffusive heat flux from each parameterization in order to compare it to the heat budget derived diffusive heat fluxes (Figure 2.6a). Further, we divide the above diffusive heat fluxes by the horizontal mean temperature gradient for each isotherm in the SWP Basin determined from a

hydrographic climatology to calculate the mean diffusivity for the basin (Gouretski & Koltermann, 2004)(Figure 2.6b).

2.4 Results

Each term in the heat budget in the North SWP Basin is examined using the measurements along P06 section and Samoan Passage and compared to diffusive heat flux and diffusivity estimates from finescale parameterizations and χ-pod measurements. The occupations of P06 are also used to estimate the variability in the estimates of the diffusive heat flux from the heat budget owing to the variance in the geostrophic flow across P06, as well as the heat tendency term due to warming in the abyssal ocean (Equation 2.8).

2.4.1 Unsteady-State Terms

The waters below 0.7°C have warmed significantly throughout the basin between the 1990s and 2010s and the coldest waters have disappeared, leading to more homogeneous bottom temperatures throughout the basin (Figure 2.8; Purkey & Johnson (2010); Sloyan et al. (2013); Purkey et al. (2019); G. C. Johnson et al. (2019). Observations along P06 between 1992 and 2017 show the rate at which the deepest isotherms have fallen in the coldest layers (~25m/yr at 0.6°C), which results in a substantial loss in volume of cold water (Figure 2.8b).

In Equation 2.8, this warming is included in the heat budget through three terms. First, the unsteady warming term $V\rho c_p \frac{d\bar{\theta}_i}{dt}$ which accounts for increase in heat content of the layer over time. This term depends on the grid spacing and accounts for the fact that discrete isotherm bins could experience non-uniform warming that results in changing the mean temperature ($\bar{\theta}_i$) of the water within that bin. Since our isotherm bins are very fine (0.01 °C), this term is smaller compared to the other unsteady terms in our framework (Figure 2.5b).

Second, the effect of deep warming is accounted for in Equation 2.8 through the rate of change in isotherm volume in the terms $\rho c_p \frac{dz}{dt}\big|_{top}(\theta_{top} - \bar{\theta}_i)S_{top}$ and $\rho c_p \frac{dz}{dt}\big|_{btm}(\bar{\theta}_i - \theta_{btm})S_{btm}$ and represents a basin wide contraction or expansion of the volume of a given isotherm and

the energy required to warm a given volume of water from a given isotherm by 0.01 °C to move it into the warmer layer. This effect is roughly similar for the top and bottom bounding isotherms throughout much of the deep ocean and accounts for the bulk of the warming tendency term (Figure 2.5b, purple). Consequently, the heat tendency term reduces to near-zero as the basin-wide isotherm contraction goes to zero, representing a steady-state in the warmer isotherm classes above 0.85°C.

We have assumed for our calculation that the rate of isotherm heave in the basin observed along P06 (Figure 2.8b) is representative of the meridional variation in the entire basin. This is supported by data from GO-SHIP lines P15 and P16, the two meridional sections along the east and west sides of our study region, showing similar rates since the 1990s (see Purkey et al. (2019)).

2.4.2 Lateral Transport from Geostrophic Velocities

The structure and magnitude of geostrophic velocity across P06 into the North SWP Basin is consistent between occupations, with small differences in magnitude and location of the DWBC (Figure 2.3). We find the highest velocities in the DWBC to occur within the core of the DWBC with mean velocities between 3 cm s^{-1} and 10 cm s^{-1} found below 4000 m between 179°W and 177°W. However, structure and location of the DWBC core vary between occupations. Despite this spatial variability within the DWBC, the integrated northward mass transport across the North SWP Basin in the four occupations is remarkably similar below γ_n= 28.1 kg m^{-3} with net transport ranging from 14.6×10^9 kg s^{-1} to 15.3×10^9 kg s^{-1} (Figure 2.4). In all four occupations, over half of the total transport is found east of 178°W within the DWBC. Some southward recirculation is observed to the west adjacent to the DWBC, but overall northward transport is observed between 170°W and 140°W, until the cumulative sum of the transport becomes constant around 130°W, where the γ_n = 28.1 kg m^{-3} isopycnal "bottoms out" along the east side of the Basin.

Despite the total northward volume transport staying relatively constant across the four

occupations of P06 (Figure 2.4), the temperature of the northward flowing waters changed substantially between occupations. The coldest waters found along 32.5°S within the North SWP Basin warmed from 0.6°C in 1992 to 0.62°C in 2017 (Figure 2.8).

2.4.3 Residual Diffusivity from Heat Budget

Summing the left hand side of Equation 2.8 gives the vertical diffusion term needed to close the budget (Figure 2.5a,black). We find that the inferred diffusive heat fluxes below 0.7°C increased by around a factor of 3 compared to the steady state diffusive fluxes with the inclusion of the unsteady terms in Equation 2.8 that are leading order in the coldest part of the water column (below 0.7°C).

A reduction in the cross-isotherm upwelling term (not shown) occurs mainly below the 0.75°C isotherm due to the reduction in volume and heat transport in the coldest layers, which is indicated by an isotherm heave signal (dh/dt) along the P06 section (Figure 2.8b). Consequently, this reduction in cross-isotherm upwelling is compensated through an increase in the diffusion term in those isotherm classes (Figure 2.5a, black). This difference in decreased upwelling transport and increased downward diffusion is most prominent below 0.65°C where the bulk of the warming is concentrated; the contribution of the unsteady terms (Figure 2.5a, purple) is non-negligible in the three-term balance between steady, unsteady and diffusion terms. The contribution of the unsteady terms to the increased diffusive heat flux reduces greatly by 0.75°C and is virtually the same as would be under a steady-state assumption above 0.8°C. This is primarily driven by a gradual minimization of the warming-driven isotherm heave signal of waters with temperatures greater than 0.75°C (Figure 2.8b), as shown by persistent isotherm positions along P06 between 1992 and 2017 (Figure 2.8a). The unsteady state diffusive heat flux and diffusivity estimates from the heat budget calculation and the associated uncertainties calculated using the full range of northward heat transport in the SWP basin (see Section 2.32.3.2,2.3.3) lie within the uncertainty estimates from the finescale VKE and strain parameterizations as well as χpod observations for most of the temperature classes considered in the budget.

Steady-State Modification of the Heat Budget

Finally, in addition to formulating the full unsteady-state budget (Equation 2.8), we consider the effect of neglecting the unsteady-state terms to incorporate the more widely used framework of a steady-state heat budget (WHITEHEAD & WORTHINGTON, 1982; Hogg et al., 1982; Polzin et al., 1997; Morris et al., 2001; Heywood et al., 2002). Here we assume zero heat accumulation within each layer and do not consider the unsteady terms in Equation 2.8. That is, the heat budget is a balance between only the horizontal advection calculated using mass and heat transport estimates from individual occupations of the P06 section, vertical upwelling, geothermal heating, and diapycnal diffusion (Figure 2.2). In order to conserve heat within a layer, heat entering within a layer must either exit the layer as outflow, upwell by advection or mix through vertical diffusion. Similar to the unsteady-state heat budget, the diffusive heat flux is in balance with the advective heat flux without the presence of the unsteady terms.

Despite the diffusive heat term being the same order of magnitude as the advective terms as well as being notably lesser in magnitude from the unsteady-state derived estimates of diffusive heat flux in the coldest isotherms below 0.65°C (Figure 2.6a), the inferred diffusivity remains well within the error of the unsteady-state estimate accounting for interannual variations in the advective transport (Figure 2.6, grey shading). The inferred diffusivity profile from both unsteady-state and steady state heat budgets (Figure 2.6b) show enhancement of turbulent mixing near the bottom, in line with recent results showing elevated levels of turbulent mixing occurring near bottom topography (up to $\sim 10^{-3}$ $m^2 s^{-1}$ here) in the abyssal basins driven in-part by internal wave interaction with ocean topography (e.g., Polzin et al., 1997; Ledwell et al., 2000; Waterhouse et al., 2014a; Mashayek et al., 2017; Drake et al., 2020). Our results also show that variations up to a factor of 8-10 between steady and unsteady budget estimates are possible when considering the full range of uncertainty bounds that account for variability in lateral heat transport in the basin.

2.4.4 Diffusivity (κ) and Dissipation Rate (ϵ) from Finescale Parameterizations and χ-pods

In much of the the SWP Basin's interior and in regions away from surface and near-bottom influences, dissipation rates are relatively weak, as measured by χ-pod observations and finescale parameterizations (Figure 2.7). However, regions of intensified mixing are observed along the interface between the 1°C and 1.25°C which roughly forms the boundary between northward flowing Circumpolar Deep Water and southward flowing Pacific Deep Water in both the χ-pod data and finescale estimates. Bottom-intensified mixing is observed along most of the section in the deep SWP Basin, especially evident in the χ-pod observations that characterize irreversible mixing and less-so from the internal-wave based parameterizations. Notable are regions around the East Pacific Rise between 140°W and 100°W show high dissipation rates and diffusivities values along the sloping bottom bathymetry, consistent with enhanced generation and scattering of internal waves over rough topography (Polzin et al., 1997; Mashayek et al., 2017; Callies et al., 2018; R. M. Holmes et al., 2018).

The strain and VKE parameterizations show high dissipation rates in patches at mid-depths, observed also in undulations of isotherms in the middle of the basin away from topography. Topographic enhancement in dissipation rate is observed in the finescale estimates along the abrupt topography of the East Pacific Rise region east of 155°W. These patterns also reveal some differences between the finescale and temperature microstructure estimates from χ-pods, which are metrics of slightly different attributes of the flow. First, the overall (median) dissipation rates from the χ-pods (Figure 2.7c) in the abyssal ocean below 1°C are slightly higher than the finescale estimates (Figure 2.7a,b), but have few regions where their means are significantly different based on bootstrap averages (Figure 2.6b). Second, the range of dissipation estimates from finescale parameterizations in regions of high dissipation associated with rough topography is larger than estimates from χ-pods, which likely reflects the fact that the χ-based estimates have significantly more degrees of freedom in their averages. While the current analysis can not

completely rule out all possible biases from χ-pod measurements (see Nash et al.,submitted), the possibility of low-biases in finescale parameterizations (Klymak et al., 2008; Polzin et al., 1995, 2014a; Waterman, Polzin, Naveira Garabato, Sheen, Forryan, Garabato, et al., 2014) in the abyssal ocean cannot be overlooked either. Although CTD χ-pod estimates are not significantly biased compared to direct measurements from shear microstructure (Nash et al., submitted), a broader evaluation of the differences and biases of the patterns of turbulent dissipation and amplitude of the energetics exhibited in the abyssal ocean will be the subject of future work and outside the scope of this study.

Mean diffusivities for the North SWP Basin are derived from estimates of average diffusive heat flux along the P06 section (Section 2.32.3.6, Figure 2.6a). The basin mean diffusivity for waters colder than 1°C calculated from the unsteady-state heat budget agrees within error estimates with the temperature microstructure estimates(χ-pod) for all isotherms colder than 1°C, and with the VKE and Strain parameterization for waters warmer than 0.7°C (Figure 2.6b). The heat budget, χ-pod and strain parameterized estimates that extend to the bottom show bottom intensified diffusivity values, decreasing exponentially towards the warmer temperature classes. The highest diffusivities from the heat budget are around $4.3\text{x}10^{-4}$ m^2s^{-1} from 2009-2010 and $3.6\text{x}10^{-4}$ m^2s^{-1} for 1992. The diffusivity estimates from the heat budget fall within 95% bootstrap confidence intervals of χ-pod as well as the strain and VKE parameterizations. In the lower water column below 0.7°C, the budget estimates agree with χ-pod, VKE and the strain parameterization within error for most of the temperature classes.

2.5 Discussion and Summary

We have demonstrated that the heat fluxes associated with the abyssal limb of the MOC in the North SWP Basin can be well constrained within uncertainty limits using data from repeated hydrography sections, mooring arrays and Deep Argo floats. This is shown by the broad agreement of inferred vertical diffusive heat flux estimates from an unsteady-state heat budget (i.e.

allowing for temporal changes in temperature, volume and heat storage) to direct measurements from the CTD-mounted χ-pods and indirect estimates from finescale parameterizations (Figure 2.6). We assess the relative contribution of each term in the heat budget, showing that the heat budget is primarily a balance between the inflow of cold waters from the south and the vertical diffusion of heat from above with a small contribution from the unsteady-state warming term. Of particular importance, direct measurements of terms in the unsteady heat budget (Equation 2.8) allow for evaluation of the assessment of measurement error in each term, a key step as we continue to develop our global deep ocean observing system.

The hydrographic section (P06) results presented here indicate a steady northward volume transport along the bottom limb of the MOC in the Southwest Pacific (Figure 2.4) with the gradual warming and eventual disappearance of the coldest abyssal waters being transported northward since the 1990s (Figure 2.8). From four repeat occupations of the P06 section between 1992-2017 we estimate that isotherms below 0.65°C in the SWP basin have been sinking at an average rate between 10m/yr and 30m/yr within uncertainty bounds, encompassing most of the abyssal ocean below 4500m in depth. For instance, between 1992 and 2017 the coldest portion of the SWP basin once consisting of waters colder than 0.6°C had warmed to ~0.62°C, resulting in an average isotherm heave of more than 1000m in the deepest portion of the basin over the period (Figure 2.8a). The resulting decrease in the volume of the coldest waters flowing into the basin is compensated by an increase in volume transport of warmer bottom waters. As the abyssal ocean is in flux, we show that the unsteady terms in the heat budget calculation are consequential in the heat balance for the isotherms shrinking in volume. We show that the Unsteady Terms (Section 2.32.3.1) below 0.64°C are within a factor of 3 of the Steady and Diffusion Terms (Figure 2.5a, Equation 2.8), which result in an increase by factor of 2-5 in the inferred diffusive heat flux and diffusivity estimates from steady-state in the bottom-most isotherms. While the unsteady-state balance regime (primarily below 0.64°C) occupies a small fraction of the range in temperature coordinates (as shown in Figure 2.5), it has consequences for large swaths of the abyssal ocean in the SWP below 4000m (Figure 2.8a). However, these deviations still remain within our overall

estimates of uncertainty as discussed below.

The largest source of known uncertainty in our budget stems from estimates of total meridional transport in and out of the basin. GO-SHIP measurements offer decadal snapshots of the global ocean. However, a large uncertainty of the total annual transport remains due to the unknown temporal variability in the northward meridional transport. We assessed this variability with Deep Argo (in the abyssal plain) and other published findings from moorings (in the DWBC region) in the SWP Basin and incorporated them into the range of uncertainty for the calculated vertical diffusive heat fluxes that would arise from variations in the northward heat transport (Figure 2.6). The future implementation of a global array of Deep Argo, complemented with the continued GO-SHIP cruises, will allow for broader assessment of the interannual to decadal variability of the deep meridional transport and will greatly reduce the uncertainty spread in the results as well as better constrain the variability in the MOC (Roemmich et al., 2019).

Further, there are several sources of uncertainty associated with the turbulent heat flux estimates presented here. Each method used in our comparison has its own intrinsic uncertainties and limitations. The finescale parameterized estimates are based upon a mathematical framework that assumes that the downscale cascade of energy from larger to smaller spatial scales is driven by nonlinear internal wave-wave interactions and results in turbulent dissipation in the ocean. While some previous studies have pointed to a strong agreement between microstructure and finescale estimates in the open ocean (Polzin et al., 2014a; Whalen et al., 2015a), others have provided insight into regions where these parameterizations may be biased, possibly due to mixing processes other than the cascade of internal wave energy captured by the current state of finescale parameterizations (Polzin et al., 1995; MacKinnon & Gregg, 2003; Klymak et al., 2008; Waterman, Polzin, Naveira Garabato, Sheen, Forryan, Garabato, et al., 2014; Ijichi & Hibiya, 2015). The χ-pod measurements are a more direct estimate of mixing because they are based on the small scales of turbulence at which irreversible mixing occurs, and hence include more turbulence-producing phenomenology. However they can be problematic at extremely low stratification (Nash et al., submitted) and are instantaneous measurements of turbulent events

and hence can be biased when turbulence is (as typical) lognormally distributed (e.g., Whalen, 2021). Biases in finescale as well as χ-pod estimates could also be introduced in certain regimes dominated by turbulent mixing driven by advective process such as downslope bottom Ekman flows near the DWBC are concerned (e.g., Naveira et al., 2019; Spingys et al., 2021). Furthermore, all methods shown here are subject to the limitation that they represent one snapshot across the basin, and may not reflect either meridional or temporal variability in turbulence, which is known to have significant variability in the deep and abyssal ocean (Polzin et al., 1997; Waterhouse et al., 2014a; MacKinnon et al., 2017a; Kunze, 2017b).

Despite these uncertainties, the agreement in averaged-profile magnitude and structure between all direct or indirect estimates of turbulence and inverse heat budget estimates is remarkable. A primary motivation for the global χ-pod program was to provide the first high resolution maps of turbulence microstructure measurements in the deep ocean. The 75 profiles shown in Figure 2.7c span a wide swath of varied bottom topography. The section traverses through a range of regimes that are considered dynamically active sites for turbulent mixing in the abyssal ocean (e.g., Polzin et al., 1997; Ledwell et al., 2000; Waterhouse et al., 2014a; Ferrari et al., 2016; Mashayek et al., 2017; Drake et al., 2020) including but not limited to a strong DWBC on the flanks of the Tonga-Kermadec Ridge, abyssal plains, ridges and seamounts as well the sloping rough topography of the East Pacific Rise. Additionally, the sheer number of profiles likely reduces some of the uncertainty associated with poor sampling of episodic turbulence events (e.g., Whalen, 2021), facilitating robust averaged profiles.

Some error could arise from imposing a basin-wide average temperature gradient calculated from the WOCE hydrographic climatology to estimate average diffusive heat fluxes for the basin. Meridional spatial inhomogeneity in the temperature gradient in the basin could result in significant spatial variations of estimated diffusive heat fluxes and diffusivities. The temperature gradient regime could be especially different from the mean temperature gradients in regions of abrupt or steep topography where multiple isotherms slump or intersect within a short depth range. Furthermore, the vertical temperature gradient is changing in time due to the

disappearance of some of the coldest isotherms in the basin (Figure 2.8), resulting in a more thermally uniform abyssal ocean and reduced stratification which in turn has implications for vertical heat fluxes near the bottom (Zhang et al., 2020).

In this study, we quantified the effect of decadal warming on the heat budget through three unsteady terms (Section 2.32.3.1) and calculated inverse estimates of diffusive heat flux and diffusivity in the North SWP Basin (Equation 2.8). Although the unsteady terms are important in the resulting heat balance for the coldest isotherms that are rapidly warming (Figure 2.5a), the resultant effect on the diffusive heat flux and diffusivity remains in the envelope of uncertainty ensuing from temporal variability in the northward abyssal transport (Section 2.32.3.2). However, we find that high resolution mixing estimates from CTD-χ-pods and indirect estimates from strain and VKE finescale parameterizations agree to within a factor of 3 for all isotherms below 1°C in the abyssal SWP basin adding confidence to our residual estimates of mixing in the basin. However,some previous studies (e.g., Katsumata et al., 2021; Huussen et al., 2012) have also found significant (between factor 8-10) disagreement between large-scale inverse and finescale parameterized estimates of mixing in the Indian Ocean. This was largely attributed to discrepancies in the inverse estimates of the strength of the Indian Ocean MOC, perhaps undersampling of intense mixing events on repeat hydrographic sections that sample a minuscule volume of the ocean or the inadequacy of finescale parameterizations to capture mixing processes other than non-linear internal wave-wave interactions. Looking to the future, the commitment of sustained global measurements of the deep MOC from Deep Argo, GO-SHIP Repeat Hydrography and moored arrays in DWBCs, coupled with high resolution global measurements of mixing from instrumentation like the CTD-χ-pod, will help close the uncertainty gap as well as advance our understanding of the mechanisms driving watermass transformation and pathways of overturning in the abyssal ocean.

Acknowledgments

We thank the WOCE, CLIVAR and GO-SHIP programs for collection of the hydrographic and LADCP data used in this study. CLIVAR and GO-SHIP data were collected and made publicly available by the International Global Ship-based Hydrographic Investigations Program (GO-SHIP; http://www.go-ship.org/) and the national programs that contribute to it. R.L, S.G.P J.A.M, and J.D.N were supported by NSF (OCE-2023289). R.L. was also supported in part by US GO-SHIP (NSF OCE-1437015) and the NASA FINESST program (Grant 80NSSC20K1609). L.D.T. was supported in part by US GO-SHIP (NSF OCE-1437015). C.B.W was supported by NSF award OCE-1923558. We thank Jim Moum, June Marion, Mike Neeley-Brown and Andy Pickering for support of Chipod instrumentation, data collection and processing, which was funded in part by OCE-1335283. The Deep Argo data were downloaded from https://www.usgodae.org/argo/argo.html. The Samoan Passage observations were funded by the National Science Foundation under grants OCE-1029268 and OCE-1029483. We thank Ilker Fer, Jacob Wenegrat and an anonymous reviewer whose comments greatly benefited the final form of this paper.

Chapter Two, in full, is a reprint of the material as it appears in the Journal of Physical Oceanography, 2021. R. Lele , S. G. Purkey, J. D. Nash, J. A. MacKinnon, A. M. Thurnherr, C. B. Whalen, S. Mecking, G. Voet and L. D. Talley(2022) Abyssal Heat Budget in the Southwest Pacific Basin *Journal of Physical Oceanography*, 51(11):3317–3333, 2021
The dissertation author was the primary investigator and author of this paper.

Data Statement

All data used for this article is publicly available. Hydrographic data is available at CCHDO (http://cchdo.ucsd.edu), LADCP data is available through the JAMSTEC (http://www.

jamstec.go.jp/iorgc/ocorp/data/beagle2003/) and

U. Hawaii (https://currents.soest.hawaii.edu/home/data/) websites. The χ-pod data collected on P06 2017 Leg 1 and 2 are available from CCHDO at https://microstructure.ucsd.edu/#/cruise/320620170703 and https://microstructure.ucsd.edu/#/cruise/320620170820 respectively. The Deep Argo data were downloaded from https://www.usgodae.org/argo/argo.html. The Samoan Passage data is available from the authors upon request.

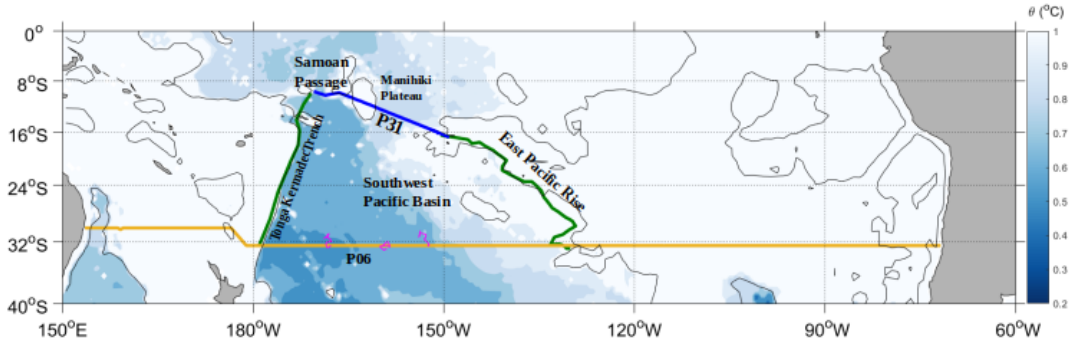

Figure 2.1. Climatological bottom potential temperature (Colorbar; Gouretski and Koltermann, 2004) within the study region of the North Southwest Pacific Basin, defined by the 4000 m isobath (black contour) to the east and west (green), Samoan Passage and P31 to the north (blue), and P06 to the south (orange). Location of three Deep Argo floats (pink) used to estimate geostrophic transport variability across P06 in 2017-2018 are indicated (Section 2.32.3.2).

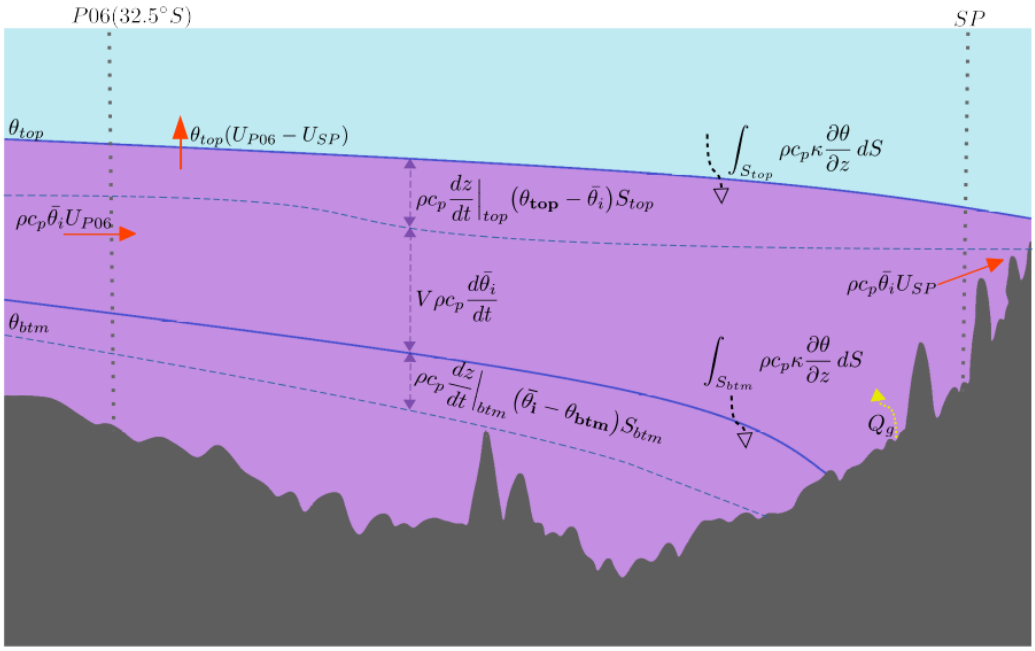

Figure 2.2. Schematic of all terms in the heat budget as described by Equation 2.8 showing heat fluxes in a zonal-mean isotherm framework (three unsteady terms, advective and diffusive flux terms) associated with meridional flow entering through the P06 section at 32.5°S and exiting through the Samoan Passage (SP).

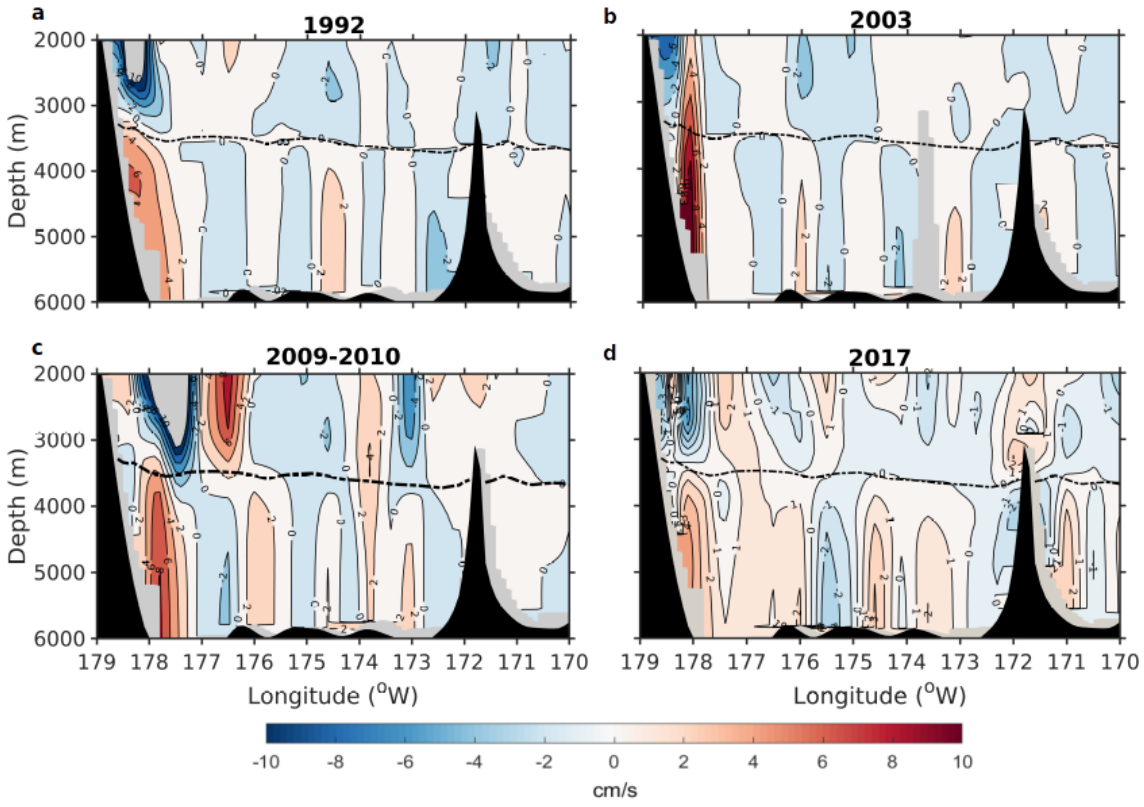

Figure 2.3. Meridional northward geostrophic velocities (cm/s) referenced to LADCP (b-d) across the Deep Western Boundary Current in the Tonga-Kermadec Ridge along P06 at 32.5°S in 1992 (a), 2003 (b), 2009(c) and 2017 (d) with bottom bathymetry (black) and the mean depth of γ_n=28.1 kg m^{-3} (dashed black contour).

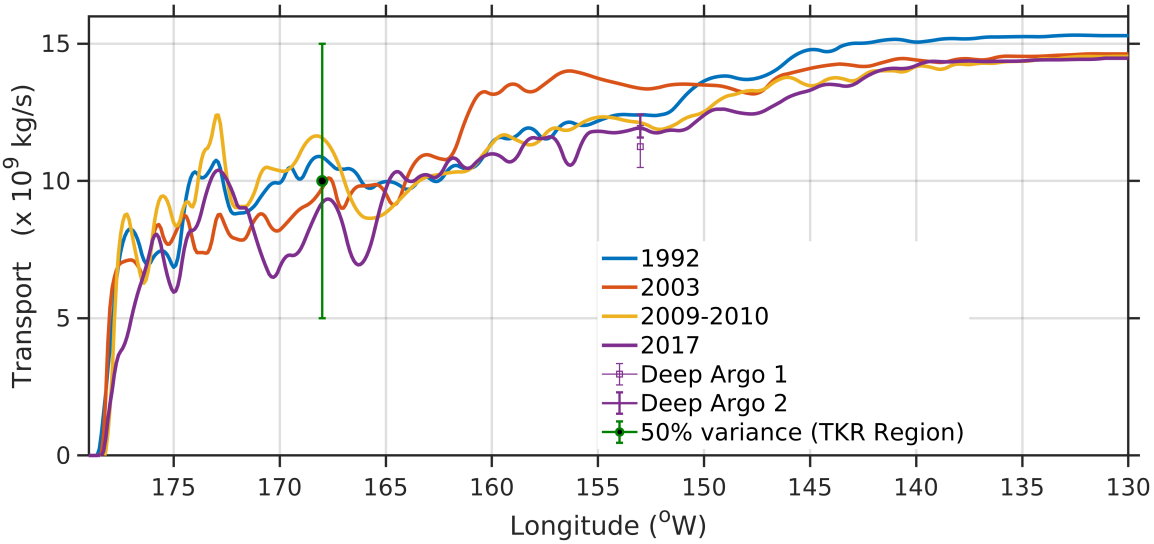

Figure 2.4. Eastward integrated net northward mass transport (kg/s) below γ_n=28.1 kg m^{-3} along the 4 occupations of P06 (colors) between the Tonga-Kermadec Ridge (179°W) and the East Pacific Rise (130°W). Accumulated transport from all the four occupations between 179°W and 168°W is shown with the green error bar representing 50% transport variance in the TKR region. Mean geostrophic transport with one standard deviation of the mean estimated between ~168°W and ~152°W (Deep Argo Float Pair 1) and ~160°W and ~152°W (Deep Argo Float Pair 2) from Deep Argo floats profiles collected between September 2017 and June 2018 are plotted at 152°W, offset by the eastward integrated geostrophic transport in 2017 at 168°W and 160°W, respectively, to show agreement with hydrography line.

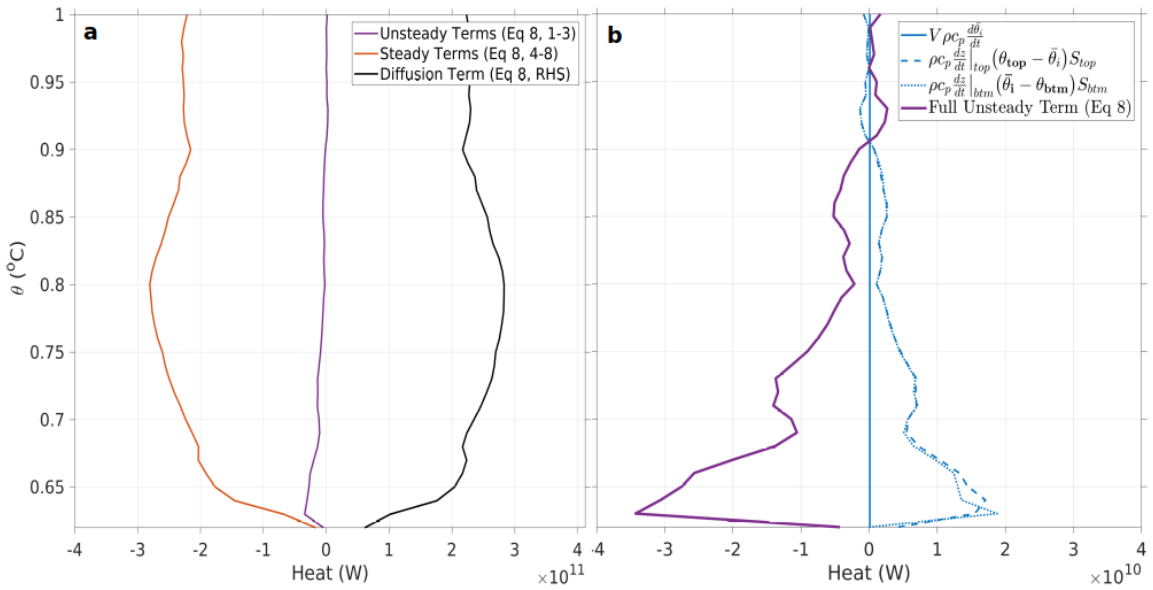

Figure 2.5. a) Heat balance for each layer between 0.6°C and 1°C (in Watts) for the components of the heat budget in the SWP basin which include Unsteady Terms (Equation 8, Terms 1-3), sum of the advective and geothermal heat terms, herein Steady Terms (Equation 8, Terms 4-8) and a Diffusion Term (Equation 8, RHS) calculated using hydrographic data from the P06 section and mooring data in the Samoan Passage (Equation 2.8), b) Three components of the unsteady term (blue) as derived in Equation 2.8 along with the total unsteady term (purple) calculated using isotherm heave (dh/dt) (Figure 5.9b) and warming within the layer.

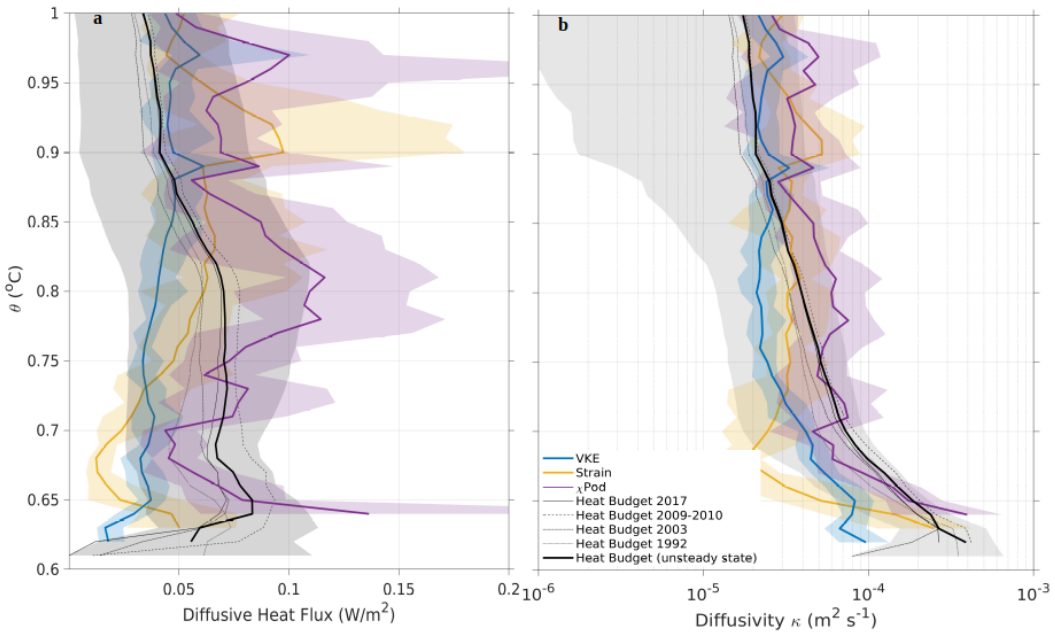

Figure 2.6. a) Profiles of basin mean diffusive heat flux [Wm^{-2}] calculated from the residual of a heat budget calculation of the North SWP Basin (black lines), also showing estimates resulting from one standard deviation of the meridional mass transport interannual variability along P06 (gray shading). Section-mean vertical profiles of diffusive heat flux calculated from two finescale parameterizations and a temperature microstructure along P06 are plotted (colors) with 95% bootstrapped confidence intervals (colored shading) b) Profiles of diffusivity (κ) [$\mathrm{m}^2\mathrm{s}^{-1}$] for the North SWP Basin calculated from the heat budget-derived mean profiles of diffusive heat flux as plotted in Figure 5.7a (black) with estimates resulting from one standard deviation of the meridional mass transport interannual variability along P06 (gray shading). Basin mean vertical profiles of κ calculated from two finescale parameterizations and a temperature microstructure are plotted (colors) with 95% bootstrapped confidence intervals (colored shading).

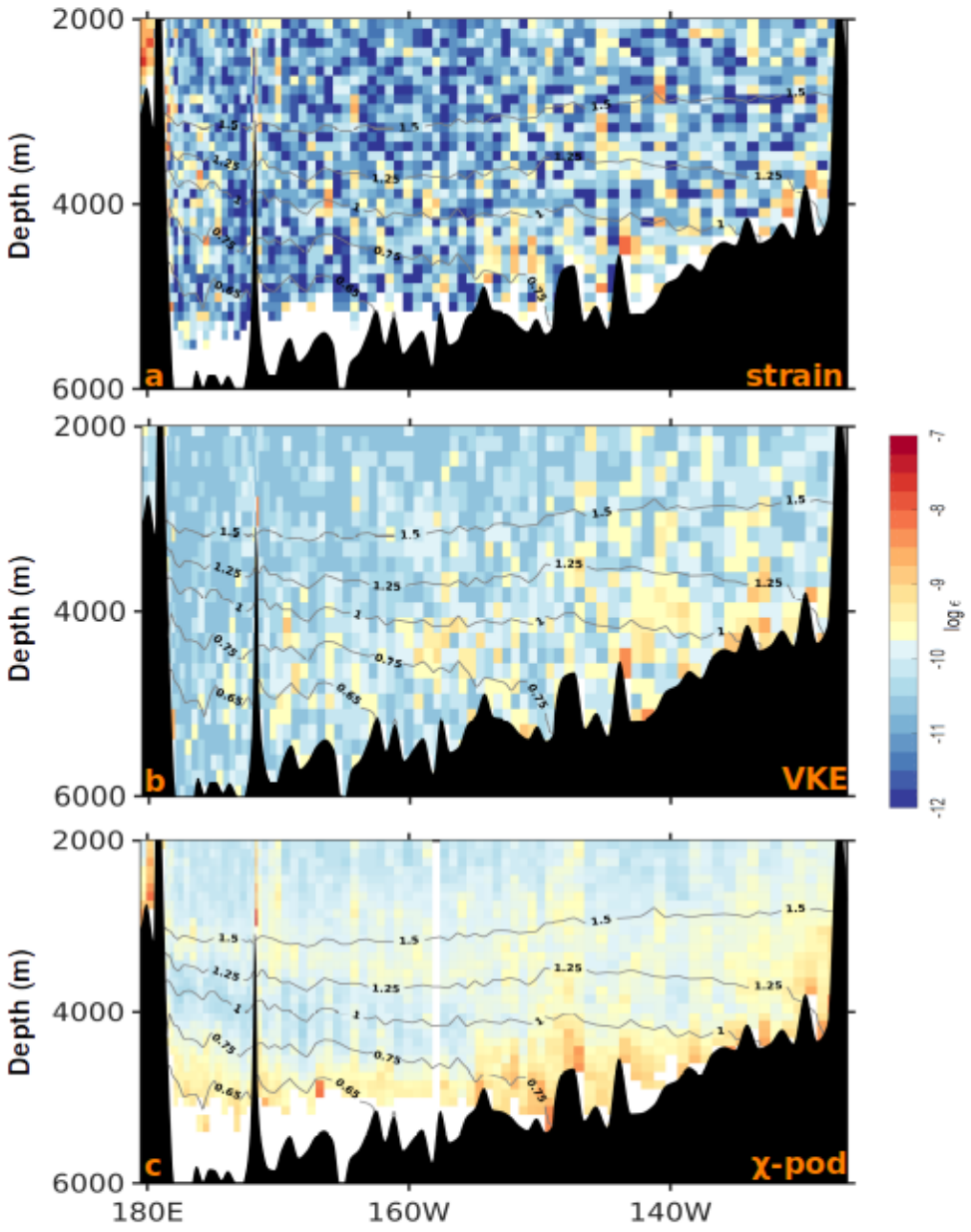

Figure 2.7. Dissipation rate (ϵ) [W kg^{-1}] in the SWP Basin along the 2017 occupation of the P06 section bounded in the east and west by the East Pacific Rise and Tonga Kermadec Ridge respectively, with bottom bathymetry (black) from a) a strain-only parameterization with a constant shear to strain ratio, b) a VKE based parameterization and c) temperature microstructure measurements of CTD-mounted χ-pods along with the 0.65, 0.75, 1, 1.25, 1.5°C isotherms contoured in grey lines.

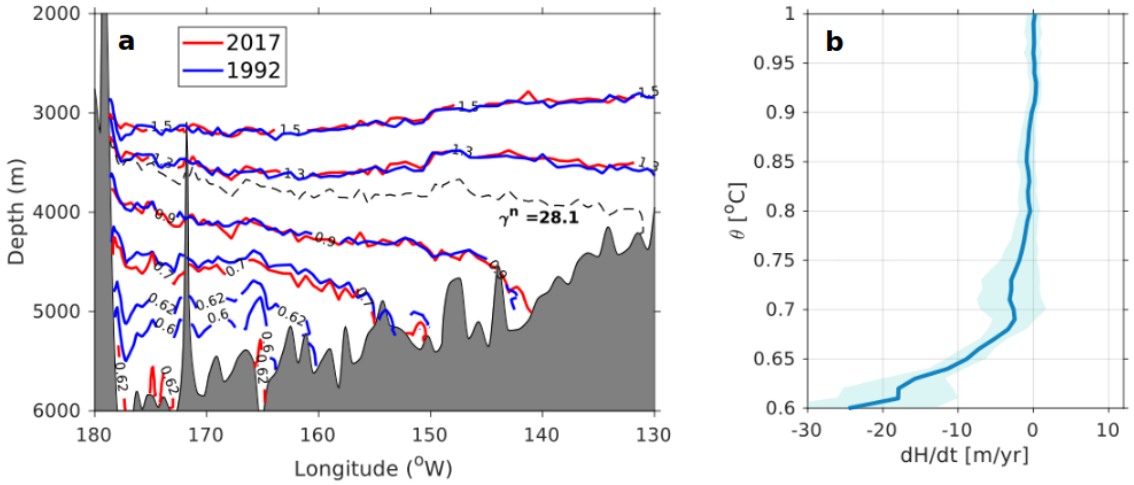

Figure 2.8. a) Isotherm contours in 1992 (blue) and 2017 (red) along P06 across the SW Pacific Basin with mean neutral density γ_n=28.1 kg m^{-3} between 1992-2017 (dashed black), b) rate of isotherm heave dH/dt(m yr^{-1}) calculated using 4 occupations of P06 between 1992 and 2017 along with 95% confidence intervals (blue shading).

Chapter 3

Ocean mixing measured by fast-response thermistors on traditional shipboard CTDs: sources of uncertainty and bias.

Abstract

Direct quantification of ocean mixing generally requires measurement of ocean properties at the O(1 cm) scales on which turbulent energy dissipates. Because the measurement of temperature gradient is relatively insensitive to vehicle vibration, deep-ocean turbulence data can be acquired during routine CTD profiling. Here we document the error and bias in estimating the rate of dissipation of temperature variance χ from fast-response FP07 thermistors mounted on a standard shipboard CTD, a system we call the CTD-χpod. The most significant source of error is associated with the fact that FP07 thermistors resolve only a fraction of the temperature gradient variance at the 1 m/s profiling speed of typical CTD casts. Assumptions must thus be made about the wavenumber extent of the temperature gradient spectrum, which scales with the rate of dissipation of turbulent kinetic energy, a quantity that is not directly measured. In addition, a means for identifying contaminated data associated with mechanically-generated turbulence from the package wake is required. Here we utilize observations from a free-falling microstructure profiler with shear probes to demonstrate the validity of our method of estimating χ from partially-resolved thermistor data, and to assess uncertainty and bias. We then apply this methodology to temperature gradient profiles obtained from the CTD-χpod and compare these to microstructure profiles obtained almost synoptically. CTD-χpod estimates of χ agree within 95% confidence intervals to the shear-probe microstructure measurements and demonstrate that the method is not significantly biased. This supports the utility of the measurement as part of the global repeat hydrography program (GO-SHIP) cruises, during which this type of data has been acquired over the past few years.

Significance Statement

Understanding the processes that control the temporal variability and geographic distribution of ocean mixing is an important community goal towards obtaining more accurate global climate predictions. Until recently direct observation of deep-ocean mixing has required special free-falling profiling instruments, and because of this, mixing observations are sparse. This paper describes a relatively new technique for obtaining ocean mixing by measuring very small-scale temperature fluctuations during traditional CTD profiling. We show that the method is not significantly biased, which provides support for making continued observations within the global repeat hydrography programs.

3.1 Introduction

Diapycnal mixing affects the distribution of heat, salt, and nutrients, maintains the abyssal overturning circulation (Munk & Wunsch, 1998b), and affects both local and global-scale dynamics. Because the turbulence that drives mixing occurs at scales that are not resolved in large-scale and climate models, it must be parameterized using some combination of (i) aspects of the resolved model physics, (ii) nested higher resolution models that capture the processes that feed energy to turbulence, or (iii) theoretical formulations that characterize the energy cascade, such as an internal-wave based parameterization (MacKinnon et al., 2017b). While it is known that numerical model dynamics are sensitive to the magnitude and distribution of mixing (Melet et al., 2013b), the actual distribution of mixing is poorly constrained as a result of the dearth of direct observations (Waterhouse et al., 2014b). Inferred estimates from internal-wave parameterizations (i.e. Whalen et al., 2015b) suggest mixing to be highly heterogeneous and time variable (Whalen et al., 2018a). However, questions still remain about the validity of these internal-wave parameterizations (Waterman, Polzin, Naveira Garabato, Sheen, & Forryan, 2014). A comprehensive set of turbulence measurements that spans relevant dynamical regimes is needed to constrain mixing and develop more accurate parameterizations for the modeling

community.

While the earliest observations of ocean mixing come from the measurement of microscale temperature gradients by Osborn and Cox in the 1970s (Osborn & Cox, 1972a), quantifying deep ocean mixing has more recently relied on airfoil shear probes to determine the dissipation rate of turbulent kinetic energy ϵ. ϵ has become one of the community's standard measures of ocean turbulence because of its dynamical importance as the irreversible sink of energy for the internal wave energy cascade (Gregg, 1987) on both local and global/climate scales (MacKinnon et al., 2017b). It is computed from the variance of velocity gradient, which has a relatively universal spectral shape with subranges described by power-law formulations (Figure 3.1). Conveniently, the amplitude and wavenumber extent of the shear spectrum depends on only one parameter (ϵ), so microstructure profilers equipped with shear probes can be used to obtain ϵ as $\epsilon = \frac{15}{2}\nu(du/dz)^2$ without needing to resolve the entire shear spectrum (Grant et al., 1962; Osborn, 1974); here ν is the molecular viscosity and only Taylor's frozen-flow hypothesis and isotropy have been assumed (J. Moum et al., 1995). However, the measurement of microscale shear is highly sensitive to mechanical vibration, so shear-probe estimates require hydrodynamically-quiet free-falling profilers and have been largely focused on targeted upper-ocean process experiments. As a result, existing measurements of diapycnal mixing, especially in the deep ocean, are sparse (Waterhouse et al., 2014b).

In order to obtain a larger quantity of mixing estimates, considerable work has gone into inferring mixing from measurements made during routine sampling from shipboard CTD and/or lowered ADCP. One common method is the use of Thorpe scales, where diapycnal mixing is inferred from adiabatically resorting statically-unstable temperature or density inversions, assuming that the energy associated with the static instability is that which ultimately supports the turbulence (Thorpe, 1977; Dillon, 1982). This method can work well when turbulence is energetic and eddies have large scales; however, in regions of high stratification or weak turbulence, sensor resolution and noise become more important and control the minimum resolvable ϵ (Galbraith & Kelley, 1996). While some studies indicate relatively good agreement with microstructure and

other observations, there remain questions about the assumptions and the validity of the method, which is based on the potential for mixing and not the mixing itself (Mater et al., 2015; Scotti, 2015).

Parameterizations based on large-scale vertical shear and/or strain have also been developed and applied to estimate diapycnal mixing (Gregg, 1989; Kunze et al., 2006b; Polzin et al., 2014b; Whalen, Talley, & MacKinnon, 2012; Whalen et al., 2015b). However, they rely on a series of assumptions about the internal wave energy cascade and its relationship to turbulence dissipation that may be violated. Numerous studies (i.e., Waterman, Polzin, Naveira Garabato, Sheen, & Forryan, 2014) have found appreciable uncertainty associated with these parameterizations, in that there can be substantial regions that are consistently biased, yet with a sense of bias (i.e., over-predict vs. under-predict) that is not known a priori.

Another means of estimating ocean turbulence has been proposed by Thurnherr et al. (2015b), who suggested that ϵ can be related to the vertical kinetic energy spectrum through a single parameter. This provides an attractive complement to the shear/strain parameterizations because it relies on a different set of assumptions, and hence can be used as an additional mostly-independent estimator of ocean mixing. Indirect metrics, such as measuring the spread of a passive tracer such as dye, are also an effective constraint on the integrated effect of mixing (Ledwell et al., 1998b), but these also require substantial observational efforts. However, of the above methods, only shear probes measure the dissipation rate directly.

Quantifying turbulence directly from moorings or traditional profiling platforms that are mechanically coupled to the ship is challenging because of vibration and package-motion that corrupts shear-probe measurements. A number of alternatives have been suggested, ranging from the use of pitot-static tubes to compute the turbulent velocity spectrum (J. N. Moum, 2015), optical sensors that capture fluctuations in index of refraction from which density fluctuations are inferred (M. H. Alford et al., 2006) and acoustical techniques to measure highly-resolved velocity fields (Shcherbina et al., 2018). Each of these suffers some limitations, ranging from noise, low-signal level, calibration challenges, failure at high pressures, lack of acoustical scatterers, etc.

Even shear probes have challenges, because they only provide ϵ and not the diapycnal diffusivity of scalars, K_ρ, which must be inferred from ϵ as $K_\rho = \Gamma\epsilon/N^2$ (Osborn, 1980b), where N^2 is the buoyancy frequency and Γ is a mixing efficiency, assumed to be constant.

3.2 Using χ and K_T to quantify ocean mixing

An alternative direct measure of turbulent mixing is obtained from the dissipation rate of temperature variance, defined as $\chi = D_T \left\langle |\nabla T'|^2 \right\rangle$, where $\nabla T'$ is the microscale temperature gradient and D_T the molecular diffusivity for heat or thermal conductivity (Osborn & Cox, 1972b). By assuming a steady production-dissipation balance in the evolution equation for turbulent temperature variance, Osborn & Cox (1972b) formulated the eddy diffusivity for heat as $K_T = \frac{1}{2}\chi/(dT/dz)^2$ where dT/dz is the background vertical gradient of temperature. This "Osborn-Cox" formulation for mixing has the advantage that (i) it relies only on temperature and temperature gradient, the measurement of which is both relatively straightforward and largely insensitive to platform motion, and (ii) it does not explicitly require assumptions about Γ. The challenge, however, is that (i) the shape of the temperature gradient spectrum exhibits considerable variability (Gargett, 1985), (ii) temperature gradient variance extends to very small scales, so that its spectrum is seldom fully resolved, and (iii) its wavenumber extent does not scale with χ but instead depends on ϵ (see Figure 3.1) via the Batchelor wavenumber k_b (Batchelor, 1959; Dillon & Caldwell, 1980):

$$k_b = [\epsilon/(\nu D_T^2)]^{1/4}. \tag{3.1}$$

Thus, unless measurements capture the full viscous-diffusive subrange of turbulence (i.e., down to scales $\Delta x \sim 1/k_b \sim 1$mm) in all three dimensions, assumptions must be made to compute χ. For example, Gargett (1985) demonstrated that spectral shape in the viscous convective and dissipation subranges of T often does not follow a universal form and attributed the deviations to the anisotropy of geophysical turbulence. This spectral variability has ramifications for the choice of canonical spectrum used(i.e., Batchelor vs. Kraichnan, see for example Bogucki et al.,

1997), and for determining the proper choice for "constants" like Batchelor's q that controls the spectrum's high-wavenumber extent (Smyth, 1999) and the Obukhov-Corrsin constant C_T that controls the amplitude in the inertial subrange (Sreenivasan, 1996). Notwithstanding questions about the validity of these assumptions, the fundamental parameter controlling the wavenumber extent of the scalar spectrum is the Batchelor wavenumber k_b. To estimate k_b when ϵ is not independently measured, we follow Oakey (1982a) and M. Alford & Pinkel (2000) and make the assumption that $K_T = K_\rho$. While this assumes a statistical equilibrium and relationship between the turbulence and mixing of a stratified fluid that is seldom achieved, J. Moum & Nash (2009) and Perlin & Moum (2012) find that the relatively weak dependence on ϵ leads to robust estimates of χ from moored timeseries. Here we perform a similar set of validations to test these assumptions with data obtained from lowered CTD rosettes.

Over the past decade, χpods – self-recording devices that measure temperature variance using an FP07 thermistor and sensor acceleration (J. Moum & Nash, 2009) – have been mounted on shipboard CTD rosettes to acquire temperature microstructure data while CTD/LADCP profiling. In our first deployments from R/V Revelle in Luzon Strait, 2010, the rosette was vaned and sensors extended from the leading edge of the rosette in order to sample fluid undisturbed by the rosette itself. While the quality of the data was high, it was cumbersome to vane the ship's rosette. To support a broader effort to increase our global database of mixing, the operation was simplified and χpods were installed above and at the bottom of the rosette (Fig. 3.2), permitting χ to be acquired during the standard cross-basin hydrographic lines of the Global Ocean Ship-based Hydrographic Investigations Program (GO-SHIP) without modifying the rosette. These data serve 2 purposes. First is to characterize the spatial and temporal distribution of turbulence at many locations globally, in order to understand the relationship of mixing to the observed large-scale forcing that could be resolved by models. The second is to determine generalized relationships between mixing and the local internal wave climate, in order to test the validity of indirect measures of mixing, such as that used by Kunze et al. (2006a) and Whalen et al. (2015a)

In addition to the data collected by Oregon State University and processed following the

methods outlined here (i.e. R. Holmes et al., 2016), other groups have also obtained temperature microstructure from FP07 thermistors during shipboard CTD profiling (Muench et al., 2009; Wang et al., 2016), but process the data in notably different ways. For example, Goto et al. (2018b) collected temperature microstructure on 72 traditional casts in the North West Pacific Ocean and find excellent agreement between these estimates and those made from a traditional free-fall turbulence profiler for low TKE dissipation rates ($\epsilon < 10^{-8}$ W/kg). However, their methodology uses the Maximum Likelihood Estimator (MLE) method of Ruddick et al. (2000), which requires that the rolloff of the temperature gradient spectrum be captured, a criterion often not met in the most interesting parts of the ocean where ϵ often exceeds 10^{-7} W/kg.

The goal of this paper is to describe the methods used to compute χ and K_T with χpods mounted on CTDs (Figure 3.2), such as ones used during GO-SHIP sections. We first describe the methodology and show an example profile of the data. We then validate the methodology using profiles of temperature gradient measured by thermistors on Chameleon, OSU's microstructure profiler, taken at 0.75° N, 110° W. Because Chameleon is a loosely tethered profiler equipped with shear probes (J. Moum et al., 1995), it directly measures ϵ (in addition to χ) and allows us to directly test our assumptions. Specifically, it allows us to determine biases associated with computing χ from partially-resolved temperature gradient spectra alone, as compared to computation that includes ϵ, which constrains the wavenumber extent of the scalar spectra as well as its amplitude. We show that this methodology is a marked improvement over that used by Ruddick et al. (2000) and Goto et al. (2018b), which is significantly biased for large ϵ. Finally, we apply the methodology to CTD-χpod profiles obtained contemporaneously with microstructure profiles to verify the method can be applied to temperature gradient obtained during profiling using a traditional CTD rosette, and describe an example application to one of the GO-SHIP repeat hydrography lines (P06).

3.3 Data

3.3.1 EQ14

In Fall 2014, data were collected on the R/V Oceanus during the EQ14 experiment (at 110° W, 0.75° N) to study equatorial mixing. In this experiment, 35 CTD-χpod profiles were obtained for calibration purposes within a timeseries of more than 2700 Chameleon profiles. Chameleon profiles were made to a maximum depth of about 250m, with CTD casts going to 500m or deeper. The EQ14 experiment and results are discussed in more detail in R. Holmes et al. (2016) and Warner et al. (2018).

3.3.2 P06

Data from the Pacific Ocean zonal repeat hydrographic section P06 across 32.5°S were collected on R/V Nathaniel B. Palmer as part of the GO-SHIP program between Sydney (Australia) and Valparaiso (Chile) in austral Winter 2017 (July-September). A total of 250 CTD χpod profiles from two upward-looking and one downward-looking χpod each, were collected from the surface to a maximum depth of 6000m (Figure 3.3). The stations were nominally spaced at 55km (~0.5°), with closer spacing in regions of interest such as western and deep western boundary currents, ridges, trenches and other topography. The results from this hydrographic section pertaining to abyssal circulation and mixing in the Southwest Pacific (SWP) Basin are discussed in more detail in Lele et al. (2021). Traditional microstructure data were not acquired during this section, except for finescale parameterized data.

3.4 Methods

Temperature gradients are rarely resolved at the smallest scales of turbulent mixing; the fraction of the temperature gradient spectrum resolved depends on the shape and wavenumber extent of the true spectrum (a function of ϵ, the "age" of the turbulence, etc.), the flowspeed past the sensor (u), and the response of the thermistor. The GE/Thermometrics FP07 thermistors we

use typically resolve frequencies up to about $f_{max} = 10 - 25$ Hz (Nash et al., 1999). The maximum resolved wavenumber is then equal to $k_{max} = f_{max}/u$, while the wavenumber extent of the true spectrum varies with k_b (and $\epsilon^{1/4}$), and other factors we only partially understand (J. D. Nash & Moum, 2002; Bogucki et al., 2012). For even relatively weak turbulence characterized by $\epsilon = 10^{-9}$ W/kg, only 50% of the temperature gradient variance is captured by integrating spectra to 20 Hz (assuming ~1m/s CTD rosette profiling speed, see Gregg, 1999, figure 12, for example). While methods have been developed to fit the observed temperature gradient spectrum to theoretical forms (Ruddick et al., 2000), these were developed for slowly-falling profilers in lakes and are only effective when (1) a large fraction of the temperature gradient spectrum is resolved, and (2) the time constant of individual thermistors is well-characterized. Goto et al. (2018b) show, for example, that the MLE method is unbiased only for $\epsilon < 10^{-8}$ W/kg), and if the thermistors have been previously calibrated by empirically adjusting the thermistor double-pole time constant τ to minimize the error in ϵ obtained from a free-falling profiler (Goto et al., 2016). Unfortunately the thickness of glass covering the FP07 microbead thermistor varies significantly from sensor to sensor, such that τ can vary by 50% between individual thermistors (see Gregg & Meagher, 1980; J. Nash & Moum, 1999, figure 3.12 and the Appendix for more details). Since ϵ scales to the fourth power of the spectrum's wavenumber extent, individual thermistor response calibrations are necessary for such methods to be applied, even for low ϵ. At higher dissipation rates sampled at profiling speeds typical of CTD casts, the MLE method is strongly biased (see Goto et al., 2018b, and appendix B for details). Because the bias cannot be determined a priori, the MLE method should be used with caution, and we suggest the following methodology is preferred because it does not require the spectral peak to be resolved nor does it have a strong ϵ-dependent bias.

We first outline our method for estimating χ, which parallels J. Moum & Nash (2009) and relies on (i) converting temporal gradients to spatial gradients using the instantaneous flowspeed past the sensor, (ii) defining the relevant values of N^2 and $(dT/dz)^2$ used to relate χ and ϵ, (iii) applying an iterative method to compute χ, and finally (iv) identifying (and rejecting)

periods where data may be contaminated by the wake of the CTD rosette. We then discuss some limitations and practical considerations that arise.

3.4.1 Iterative Method for Estimating χ

For each 1-s window, χ is estimated via the following procedure as outlined in J. Moum & Nash (2009). For isotropic turbulence,

$$\chi = 6D_T \int_0^\infty \Phi_{T_x}(k)dk \tag{3.2}$$

where D_T is the thermal diffusivity and $\Phi_{T_x}(k)$ is the wavenumber spectrum of dT/dx, computed from the Fourier transform of windowed and detrended dT/dt converted using Taylor's frozen flow hypothesis:

$$\frac{dT}{dx} = \frac{1}{u}\frac{dT}{dt} \tag{3.3}$$

where u represents the flow speed past the sensor and x is a spatial coordinate of the fluid trajectory relative to the sensor.

We assume $K_\rho = K_T$ and $K_\rho = \Gamma\epsilon/N^2$, and the mixing efficiency $\Gamma = 0.2$ (J. Moum & Nash, 2009) to determine ϵ_χ (the dissipation rate inferred from χ) as:

$$\epsilon_\chi = \frac{N^2\chi}{2\Gamma < dT/dz >^2} \tag{3.4}$$

Typical thermistors do not resolve the spectrum out to $k \approx k_b$, so the measured spectrum is fit to the Kraichnan form (with $q = 7$) of the theoretical scalar spectrum over the range of resolved wavenumbers ($k_{min} < k < k_{max}$). The variance between the measured $[\Phi_{T_x}(k)]_{obs}$ and theoretical $[\Phi_{T_x}(k)]_{theory}$ spectra at these wavenumbers is assumed to be equal:

$$\int_{k_{min}}^{k_{max}} [\Phi_{T_x}(k)]_{obs}dk = \int_{k_{min}}^{k_{max}} [\Phi_{T_x}(k)]_{theory}dk \tag{3.5}$$

An iterative procedure is then used to fit and calculate χ and ϵ_χ:

1. First we estimate χ based on an initial guess of $\epsilon_\chi = 10^{-7}$ W/kg and compute k_b via eq. 3.1. We set $k_{max} = k_b/2$ or to a wavenumber equivalent to $f_{max} = 7$ Hz [i.e., $k_{max} = 2\pi(f_{max})/u$], whichever is smaller. In general f_{max} is the highest frequency that is not attenuated by the sensor roll-off; we use $f_{max} = 7$ Hz based on historical data for these sensors (see Appendix A for more details).

2. We then use Eq. (3.4) to refine our estimate of ϵ_χ and k_b and recompute χ using Eqs. (3.2) and (3.5).

3. This sequence is repeated and converges after two or three iterations.

We note that this procedure is equivalent to the explicit formulation of (M. Alford & Pinkel, 2000), except we use the Kraichnan theoretical form instead of the Batchelor spectrum for $[\Phi_{T_x}(k)]_{theory}$. At wavenumbers below the spectral peak, there is little distinction between the Kraichnan and Batchelor spectra, so this does not introduce a bias. In this paper we use both χ and χ_χ interchangeably to denote estimates using the above procedure, the latter used for clarity in section 5 to differentiate it from χ_ϵ, that computed using an independent measure of ϵ to constrain k_b.

3.4.2 CTD-χpod Data Processing

We next review the basic outline for processing each CTD-χpod profile. In contrast to the moored χpod (which is self contained with a pressure sensor and pitot-static tube for speed; J. Moum & Nash, 2009), the CTD-χpod requires pressure measured by the CTD and has no independent speed measurement other than dp/dt from the CTD. The procedure for merging data sources and computing N^2 and dT/dz are as follows:

1. The time offset for the χpod clock is determined by aligning dp/dt from the 24Hz CTD data (high-pass filtered with a 3 dB point of 25 s) to the time-integrated vertical acceleration measured by the χpod. Records are aligned within < 0.5 s so that (i) the correct value

of u is used, and (ii) wake contamination can properly be identified. In the case of the CTD-χpod we assume u is solely due to the vertical motion of the CTD cage so that $u = W = dp/dt$.

2. Low-order polynomial calibration coefficients are determined to convert thermistor voltages from χpod to ITS90 temperature (as measured by the CTD). Figure 3.3 shows an example of the aligned and calibrated CTD-χpod time series for one cast. Note the significant differences in amount of variance associated with the two sensors during down and up casts. For the upward-mounted sensor (T1), the downcast signal is largely associated with the CTD wake, as is the upcast for the downward-mounted sensor (T2). Only the 'clean' portions of the cast (e.g., the T1 upcast and the T2 downcast) are used in the χpod calculations.

3. Buoyancy frequency N^2 and temperature gradient dT/dz are computed from 1-m binned CTD data, and averaged over a scale of 10m.

4. Half-overlapping 1-s windows of data are used to estimate χ following the methods described in J. Moum & Nash (2009), as outlined in the previous section.

3.4.3 Identifying wake-contaminated data

Unlike free-falling turbulence profilers, the CTD rosette's motion is strongly coupled to the ship and experiences large changes in profiling speed. When sampling in rough seas, ship roll can be so severe that the rosette changes direction and the thermistors sample eddies from the rosette's wake instead of the geophysical turbulence. Even if the rosette doesn't fully reverse direction, rapid deceleration can cause fluid from within the cage to be shed ahead of it and be sampled by the χ-pods. Examples of both types of motions are evident from the pressure and temperature record shown in Figure 3.4 from P06. Because temperature variance in the wake (following a slowdown) can be many orders of magnitude greater than our real signals, such time periods must be identified to avoid bias in estimates of χ.

Goto et al. (2018b) provide some initial guidance towards defining an objective criterion for rejecting wake-contaminated χ data based on CTD fallspeed and comparing to simultaneous estimates of χ from their CTD-rosette and a free-falling profiler. In their study, FP07 thermistors were located at the bottom of the rosette and contaminated χ was linked to elevated variance in vertical velocity within the 1-s bins over which χ was computed. Goto et al. (2018b) propose rejecting data when the standard deviation of vertical velocity in a 1-s window (W_{sd}) exceeds a threshold. For their configuration, data in which $W_{sd} > 0.2W - 0.06$ m/s are rejected, where W is the rosette speed. Based on this, all data for $W < 0.3$ m/s are rejected, as are data with $W_{sd} > 0.14$ m/s for $W = 1$ m/s, typical of our casts. While this appeared successful for their sampling setup, the criterion they employ does not consider the deterministic motion of the CTD rosette. When we apply the criterion of Goto et al. (2018b) to the χ-pod CTD we've acquired, we find that their criterion does not always reject data that is clearly within the wake of the CTD during a reversal of profiling direction. Instead, we use criteria that are related to the longer-timescale variations in vertical profiling speed (associated with ship roll/heave), and not the sub 1-sec variability of the rosette.

Figure 3.4 provides an example of how regions of high variance in dT/dt (and consequently χ) are related to the rapid deceleration and/or reversal of the CTD rosette, and that this often lasts for several seconds after such reversals. To identify regions of potential contamination of χ, we adopt the following procedure.

First, on most CTD-χpod repeat hydrography cruises two upward oriented FP07 sensors were deployed on either side of the CTD cage to provide simultaneous independent measurement of dT/dt. This redundancy provides a straightforward way of detecting events that are clearly non-geophysical. Similar to our routines for rejecting plankton spikes on shear-probes (J. Moum et al., 1995), we reject data from a sensor if its χ estimate exceeds that of the other sensor by more than a factor of 3; otherwise data from both sensors are averaged. FP07 sensors were also deployed at the bottom of the CTD Rosette; under moderate ship-heave, data from these sensors are often contaminated by wake from the CTD rosette and are not used for this analysis.

Next, depth loops are identified and flagged in the 24Hz CTD data. If the CTD speed (which is nominally 1 m/s) slows below 0.3 m/s, data are discarded within 2m of the minimum/maximum extent of the speed drop. For data collected during rough sea-states (eg. majority of GO-SHIP data), we find that additional thresholding is necessary, and we further reject data 2 seconds before to 7 seconds after any event when the vertical velocity drops below 0.1m/s, (i.e., this criterion is applied when the CTD fully reverses direction and for cases bordering on the "loop" criterion). We note that the above threshold of 0.3 m/s as a low-speed cutoff is consistent with Goto et al. (2018b)'s W criterion (and their Fig. 9) but is more stringent because it rejects data outside of the slowdown interval. An 80-s segment of data from P06 during a moderate sea-state demonstrates the data retention after the above criteria are applied (Figure 3.4).

Even for profiles significantly affected by ship heave, good segments of data are retained between most CTD rosette slowdowns and reversals, allowing estimates of χ to be computed in nearly every 10-m bin. A typical full profile of χ obtained during the P06 section is shown in Figure 3.5 to demonstrate the degree to which surface wave induced ship heave (characterized by the rosette speed variability) contaminates the temperature gradient data. Note that this includes the data segment shown in Figure 3.4. Shown is both the retained (blue) and rejected (grey) 1-m χ estimates to illustrate how the fraction of data rejected increases with the amplitude of the swell-induced motion. In general we find that rosette motion to be greatest near the ocean surface and becomes increasingly uncoupled from the ship at deep depths. As a result, our relatively stringent criteria for rejecting a minimum of 9 seconds of data around each slowdown rejects a significant fraction of the data, especially above 1500 m water depths in this particular case. Regardless, more than 75% of the data is retained in a majority of 200m bins below 2000m (Figure 3.5c). Shallower than 1500 m we retain on average $\sim$ 50% of the data. During the period affected by the largest rosette heave (around 200-m depth in this profile), approximately 25% of the data are retained within the 200m bin.

The retained (1-m) χ estimates span more than 6 orders of magnitude (from less than 10^{-12} to 10^{-6} K^2/s) with the majority of the data sampling the relatively quiescent abyss characterized

by $\chi \sim 10^{-12} - 10^{-10}$ K^2/s (Figure 3.5). As is characteristic of geophysical turbulence in the deep ocean, a small number of energetic events dominate the mean in each 200-m bin and its bootstrap confidence interval (black line and pink shading in Fig. 3.5b). As a result, at the 95% confidence level, the peaks at 1200, 2200 and 3600 m are not statistically different from the slowly varying background χ. Multiple casts must be averaged together to tease out the dynamics associated with these peaks.

3.5 Microstructure profiler comparisons

Here we use FP07 thermistor data collected from the free-falling Chameleon during EQ14 to assess the methodological bias and uncertainty of our computation of χ.

3.5.1 Example Spectra and Fits

Examples of the observed temperature gradient spectra and associated theoretical fits are shown in Figure 3.6 for regions of high and low ϵ. Here, the χ and associated theoretical spectra are computed in two ways: (1) the magenta curve is the theoretical Kraichnan spectra for the values of χ and ϵ as measured by Chameleon's shear probes, and (2) the dashed black line represents the curve determined by applying the χpod method to just the thermistor data for the same window (i.e., using k_b computed from ϵ_χ as estimated from equation 3.4). Note that at lower ϵ, k_{max} is closer to k_b so the peak of the spectrum is almost resolved and a larger fraction of spectral variance captured. For higher ϵ, less of the spectrum is resolved and the spectral peak is well above k_{max}. Even so, the iterative χpod method gives an accurate estimate of χ. Note that the lower-wavenumber portions of the fit are within the inertial and viscous-convective subranges and so the observed spectra and fits match at low k. They deviate at the high-wavenumber extent of the spectrum, set by k_b, which is not used in our computation.

3.5.2 Direct Test of χpod Method

We utilize highly-resolved free-falling profiler data from Chameleon (for which both ϵ and χ are measured) to test the assumptions in our method of estimating χ. We first apply the χpod method to Chameleon's FP07 thermistor data and compute χ_χ^{cham} without assuming any a priori knowledge of ϵ (i.e., we use equation 3.4 to compute k_b, yielding the dashed black lines in Figure 3.6). These estimates are then compared to χ_ϵ^{cham}, computed by integrating the theoretical temperature gradient spectrum where k_b is computed directly from shear-probe derived ϵ (i.e., the magenta curve in Figure 3.6). Qualitatively, χ_χ^{cham} and χ_ϵ^{cham} are of similar magnitude and show similar patterns in both depth and time, as shown by the comparison in Figure 3.7). A more quantitative comparison (Figure 3.8), shows the two are well-correlated over five orders of magnitude. The distribution of log_{10} of the χ ratios is approximately normal, with a mean of $\mu = -0.1$ and standard deviation of $\sigma = 0.51$, equivalent to a 20% bias low of χ_χ^{cham} relative to χ_ϵ^{cham}, and a random spread in variability of a factor of 3. The magnitude of the bias increases slightly at higher values of ϵ_{cham} (Table 3.1), reaching 40% for $-6 < log_{10}[\epsilon_{cham}] < -5$. The cause of this bias is unknown, but may be related to the spectrum shifting to higher wavenumbers at larger ϵ.

3.5.3 CTDχpod - Chameleon Comparison

Having demonstrated that the method works using Chameleon data, we now compare χ_χ^{ctd} from CTD-mounted χpods to χ_ϵ^{cham} during EQ14. In contrast to the Chameleon data, the CTD is more strongly coupled to the ship, and therefore subject to vibration, heaving, and artificial turbulence created by the rosette. A total of 35 CTD-χpod casts were performed, bracketed with Chameleon profiles immediately before and after. We first compare CTD-χpod profiles to the mean of the two Chameleon profiles bracketing each cast, both averaged in 5m depth bins (Figure 3.9). The two are correlated, albeit with considerable scatter. A histogram of the log of ratios is approximately normal and has a mean of -0.31, indicating a small negative bias. The

$\log_{10}$ standard deviation of $\sigma = 0.96$ indicates 70% of the profile-to-profile data agree to within a factor 10, which we do not associate with the χpod method but rather to natural variability of ocean turbulence. To illustrate this, histograms of the ratio of χ from adjacent casts are computed (Figure 3.10) which show that the variability between CTD χpod and Chameleon casts is similar to the natural variability between Chameleon profiles themselves. Our best inter-platform comparisons between profilers (intended to sample the same physical process) also find agreement to not better than a factor of 2 (i.e. J. Moum et al., 1995; Perlin & Moum, 2012), but only after considerable averaging. This finding is consistent with the profile-to-profile variability observed by Goto et al. (2018b), who also found $\sigma \approx 1.0$ for $\log_{10}(\epsilon_n/\epsilon_{n+1})$ for neighboring profiles n and $n+1$ (their figure A1).

Profiles from all CTD-Chameleon pairs averaged in time and 40m depth bins (Figure 3.11) overlap within 95% confidence limits at all depths (in the top 200 m) where there exists good data for both. Averages of subsets of these profiles that were clustered in position/time (not shown) also agree well. We conclude that the variability between CTD-χpod and Chameleon profiles is indistinguishable from natural variability in turbulence levels.

3.6 Discussion

We have presented a methodology for computing χ from χpods attached to CTD rosettes, and have shown that these estimates agree with those obtained using a traditional microstructure profiler. This methodology can also be applied to other profiling configurations, such as the use of χ-pods on profiling wirewalkers (J. N. Moum & Nash, 2009) or χ obtained by measuring microscale temperature gradient alongside any profiling/lowered CTD. The methodology we employ differs from that proposed by Goto et al. (2018b) in that we explicitly consider the CTD-rosette trajectories in identifying wake-contaminated data, and we use the iterative procedure of J. Moum & Nash (2009) in order to compute unbiased estimates of χ regardless of the value of ϵ (the Goto et al. (2018b) method is limited to $\epsilon < 10^{-9}\mathrm{m}^2/\mathrm{s}$). Our procedure also provides

estimates of K_T and ϵ; the accuracy of which is left for a future paper as it involves additional assumptions about the value of the mixing efficiency Γ. While $\Gamma = 0.2$ is commonly assumed (and is likely representative for the ocean average), its numerical value relevant to the instantaneous application of equation 3.4 likely has wide variability. Fortunately, the calculations presented in this paper are not highly sensitive to Γ, since χ scales to a low power of ϵ in our iterative method; J. Moum & Nash (2009) found a bias in χ of up to 1.6 for Γ values ranging from 0.1 to 0.35.

The goal of CTD-χpods is to expand the number and spatial coverage of ocean mixing observations. The census of Waterhouse et al. (2014b) found less than 20 locations where full-depth microstructure profiles were taken (see their figure 1c), all of which had less than 100 profiles. We have already deployed CTD χpods during several process experiments and on several GO-SHIP repeat-hydrography cruises, obtaining more than 1700 full-depth profiles of χ over a wide range of locations. We plan to continue regular deployment on GO-SHIP and similar cruises, adding χ to the suite of variables regularly measured. The expanding database of mixing measurements from CTD-χpods will also enable testing of other commonly-used or new mixing parameterizations. This has the potential to be transformative for the field, allowing the community to develop and test global turbulence parameterizations, use estimates of turbulence along with the CLIVAR repeat hydrography data for inverse models and water mass modification calculations, identify hotspots of turbulence to target with future process experiments, and compare with in-situ chemical and biological measurements made routinely on repeat hydrography cruises.

3.7 Conclusions

- The χpod method for estimating χ was directly applied to temperature gradients measured by the Chameleon microstructure profiler on > 2700 profiles during the EQ14 cruise. The estimated χ_χ agrees well with χ_ϵ calculated using ϵ from Chameleon's shear probes over a wide range of magnitudes (Figure 3.8) with little or no bias, demonstrating that the method

works. This allows us to estimate χ without concurrent measurements of ϵ.

- CTD-χpod profiles were also compared to nearby Chameleon profiles during the cruise. Variability between CTD-χpod and Chameleon estimates of χ is indistinguishable from natural variability between Chameleon profiles. Time-averaged profiles of χ from both platforms agree within 95% confidence limits, and no significant bias was detected between the estimates of χ.

- CTD χpods were tested on the P06 repeat hydrographic section to collect 250 profiles along the section from 6000m to the surface. We demonstrate that by incorporating certain post-processing norms in order to filter erroneous measurements primarily due to the motion of the CTD rosette and fluctuations in its fallspeed, it is possible to obtain reliable estimates of turbulent mixing under routine sampling conditions on repeat hydrographic transects that span a range of ocean sea-states.

- We conclude that estimates of χ made from the CTD-χpod platform are robust and reliable.

Acknowledgments

GO-SHIP CTD data used for χpod processing were collected and made publicly available by the International Global Ship-based Hydrographic Investigations Program (GO-SHIP; http://www.go-ship.org/) and the national programs that contribute to it. CTD χpod instrumentation, data collection and processing was funded in part by NSF OCE-1335283 and the EQ14 experiment was funded by OCE-1256620. J.N, R.L, J.A.M and S.G.P were supported in part by NSF (OCE-2023289). R.L was also supported in part by the NASA FINESST program (Grant 80NSSC20K1609). We thank the Captain and crew of R/V Oceanus and RVIB Nathaniel B. Palmer, and the numerous students and PIs who have helped support the CTD-χpod data collection. Pavan Vutukur, Craig Van Appledorn, Mike Neeley-Brown made the sensors; June Marion provided technical support for the instrumentation, and Andy Pickering created the

CTD-χpod processing framework and a number of the figures used in this paper. Aurelie Moulin, Ryan Holmes, Sally Warner and Anna Savage helped collect the EQ14 data.

Chapter Three, in part, is currently being prepared for submission for publication of the material. J.N. Nash, R. Lele, S.G. Purkey and J. A. MacKinnon, Ocean Mixing Measured by Fast-Response Thermistors on Traditional Shipboard CTDs: Sources of Uncertainty and Bias (In Preparation). The dissertation author was a co-investigator and co-author of this material and contributed to Sections 3, 4 5 and 6.

Appendix A: Thermistor Frequency Response

Prior to 2009, the transfer function for each FP07 thermistor was measured by profiling adjacent to a thermocouple in Yaquina Bay, OR. However, measuring the transfer function for each individual thermistor proved too expensive and time-consuming, and since that time a generic transfer function has been used. Figure 3.12 shows the measured transfer functions for 2008. The majority of the transfer functions are similar for frequencies up to about 10 Hz, and begin to significantly differ above that. To estimate the potential error in not using a transfer function, we calculated the % of spectral variance captured for each of the measured functions. For frequencies up to 7Hz, more than 95% is captured for 88% of the measured functions. If frequencies up to 15hz are used, more than 95 % variance is captured only 67% of the time. Using only frequencies up to 7Hz (where the transfer function is equal to or very close to unity) avoids the issue of the unknown transfer functions.

Appendix B: Test of MLE fitting method

Following Goto et al. (2018b) and others, we have applied the spectral fitting methods of Ruddick et al. (2000) to our data and compared those to the χpod method above. Consistent with the findings of Goto et al. (2018b), the MLE method works well and gives similar results to our method at true ϵ values less than about 10^{-9}, but severely underestimates χ at larger values of epsilon, where only a small fraction of the spectrum is resolved (Figure 3.13). At lower profiling

Table 3.1. Biases and standard deviations of ratios of $log_{10}[\chi_\chi/\chi_\epsilon]$ for different ranges of ϵ_{cham}.

ϵ_{cham} range	bias	std.
$-9 < \epsilon < -8$	-0.04	0.47
$-8 < \epsilon < -7$	-0.15	0.51
$-7 < \epsilon < -6$	-0.18	0.54
$-6 < \epsilon < -5$	-0.2	0.55

speeds we would expect the MLE method to work better, as more of the spectrum will be resolved for a given value of ϵ. For ocean dissipation rates and speeds typical of GO-SHIP CTD profiling, we conclude that the MLE method is not effective.

Appendix C: Sensitivity Analysis / Flowspeed Past Sensor

To quantify the potential error in the CTD-χpod calculations from ignoring horizontal velocities and assuming the flow speed is equal to the vertical speed of the CTD rosette, we repeated the calculations with constant offsets added to the flowspeed. Note that since the total magnitude of velocity is used, dp/dt is a minimum estimate of the true speed. Adding 0.1(1)m/s results in a mean percent error of -14(-58) percent (Figure 3.14), small compared the large natural variability in turbulence and uncertainty in our measurements. Note that increasing the velocity tends to result in smaller values of χ, since it shifts the spectrum to lower wavenumbers.

We also looked for any systematic biases associated with flowpseed. We found that χ was biased high for very small speeds (u < 25cm/s). This could be associated with contamination by CTD wake or entrained water when the CTD slows. These values were discarded for our analysis.

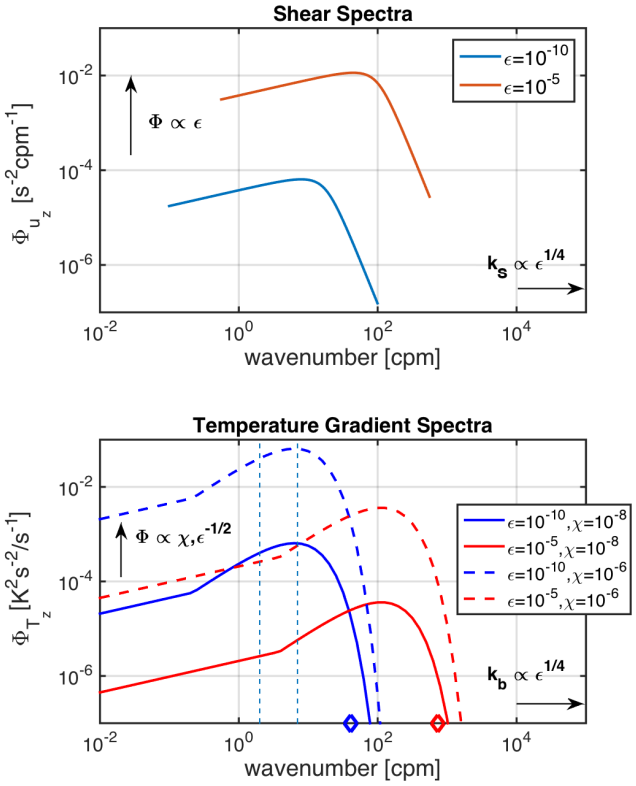

Figure 3.1. Top: Theoretical (Nasmyth) wavenumber spectra for velocity shear, for two different values of ϵ. Lower: Theoretical (Kraichnan) wavenumber spectra for temperature gradient, for two different values of ϵ and χ. Note the amplitudes of temperature gradient spectra depend on both ϵ and χ, while the shear spectra depend only on ϵ. Diamonds indicate the Batchelor wavenumber for each, which depends only on ϵ. Vertical dashed lines indicate range of wavenumbers used for χpod fit assuming u = 1m/s.

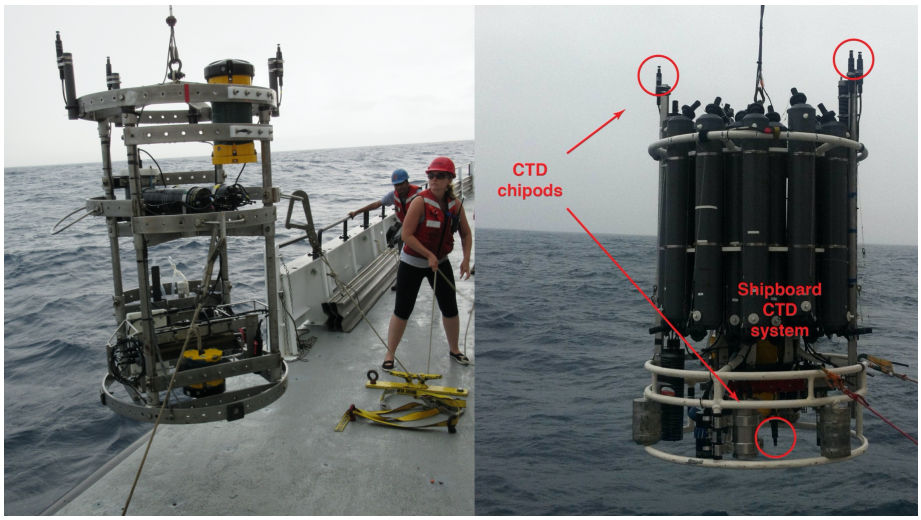

Figure 3.2. Photos of CTD rosette with χpods attached. Left shows the open configuration used during EQ14; right shows the more traditional configuration with a full set of Niskin bottles on the A16 repeat hydrography line.

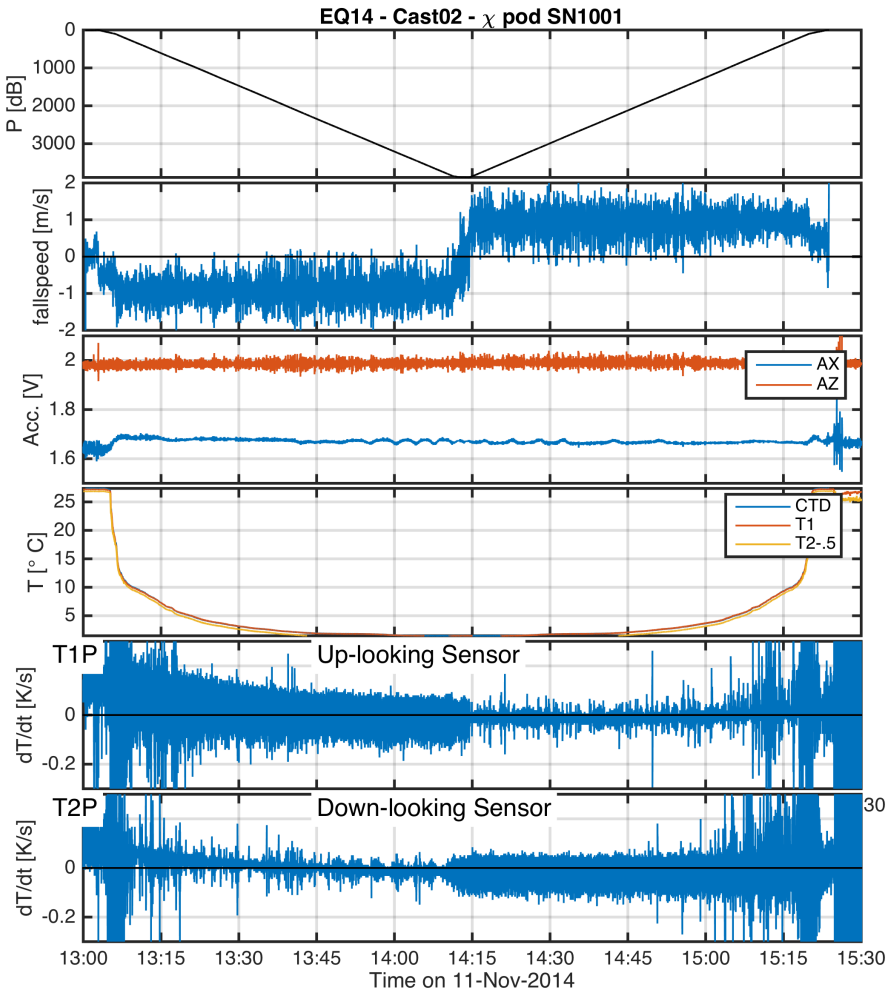

Figure 3.3. Example timeseries from one CTD cast during EQ14. a) CTD pressure. b) Vertical speed of CTD (dp/dt). c) Vertical and horizontal accelerations measured by χpod. d) Temperature from CTD and two χpod sensors (T1 and T1). T2 is offset slightly for visualization. e) Temperature derivative dT/dt measured by the upward-looking χpod sensor T1. f) Temperature derivative dT/dt measured by the downward-looking χpod sensor T2.

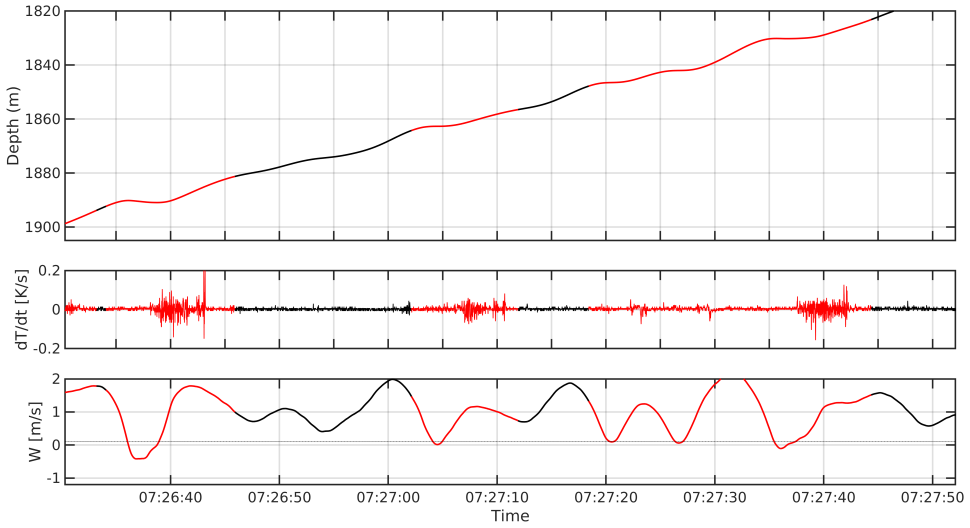

Figure 3.4. An 80-s portion of the P06 station 125 up-cast showing depth vs time (top), the χpod time series of dT/dt (middle), and the CTD rosette's profiling speed (bottom); data discarded because of the potential for contamination from the rosette's wake is indicated in red. High variance of temperature gradient occurs for 5-10 s following reversals in the rosette direction ($W < 0$) and during periods of rapid deceleration. The algorithm we apply is fairly conservative, in that it identifies the period between 7:27:18 and 7:27:37 as potentially contaminated (due to dips to $W = 0.1$ m/s), even though the data during that time period may represent real turbulence signals.

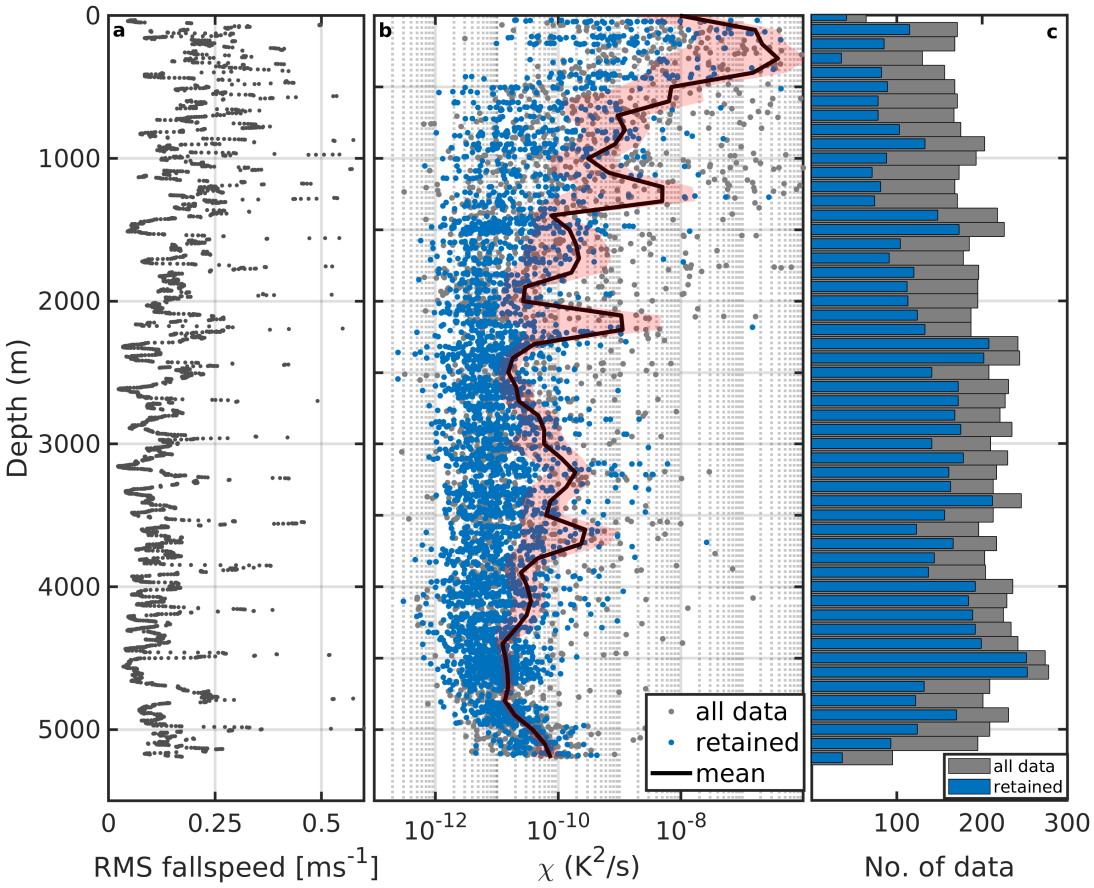

Figure 3.5. The full profile from P06 station 125 to illustrate the data retention: a) RMS profiling speed (with mean removed) of the CTD rosette computed in 50-sec intervals, b) χ estimates from the upcast collected from two upward-looking sensors showing the distribution of all of the data (grey), the retained data (blue), bootstrapped mean profile (black line) and 95% bootstrapped confidence interval (red shading) computed from the retained data in 200m half-overlapping segments, c) histogram showing the number of data points retained in each 200m half-overlapping segment after flagging for potentially contaminated estimates.

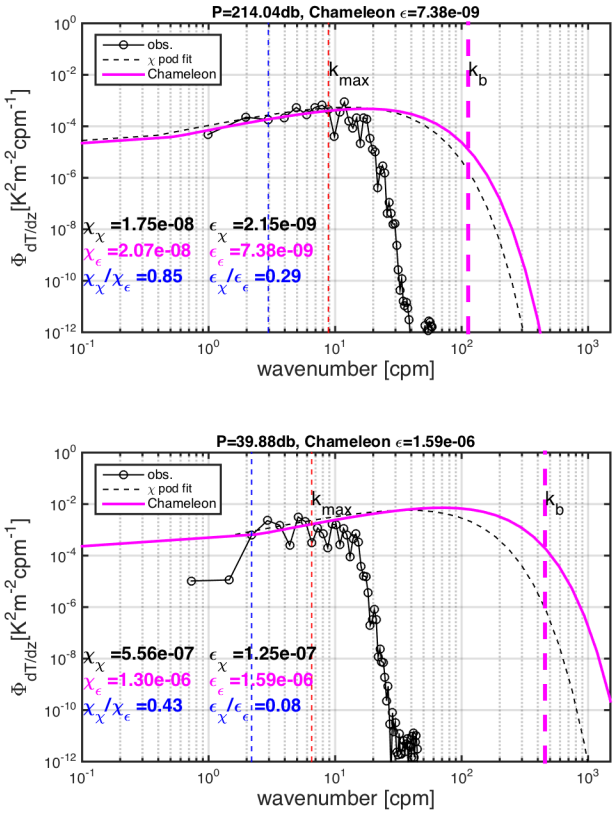

Figure 3.6. Two example temperature gradient spectra from an EQ14 Chameleon profile, for high (top) and low (bottom) values of ϵ. Solid black lines with circles show the observed temperature-gradient spectra from the thermistor on Chameleon. Dashed black line shows the fitted theoretical Kraichnan spectra estimated by applying the χpod method to the thermistor data only. Magenta line is Kraichnan spectra for Chameleon χ and ϵ measured at the same depth, using the shear probe data as well. Vertical dashed blue (red) lines indicate the minimum (maximum) wavenumber used in the χpod calculation. The Batchelor wavenumber k_b is also indicated by the vertical magenta line.

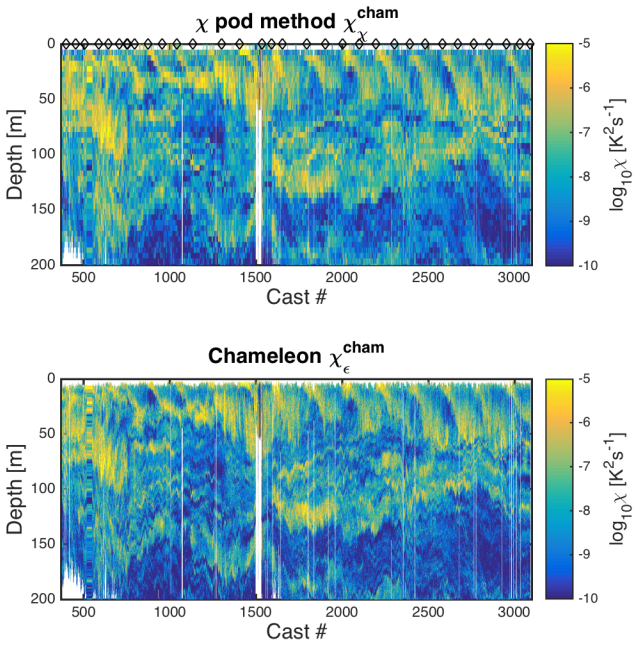

Figure 3.7. Depth-time plots of $log_{10}\chi$ from both methods for EQ14 data. Top: χpod method using only FP07 data from Chameleon. Black diamonds indicate casts used for comparison with CTD-χpod profiles. Bottom: Chameleon measurements using FP07 and shear probe data.

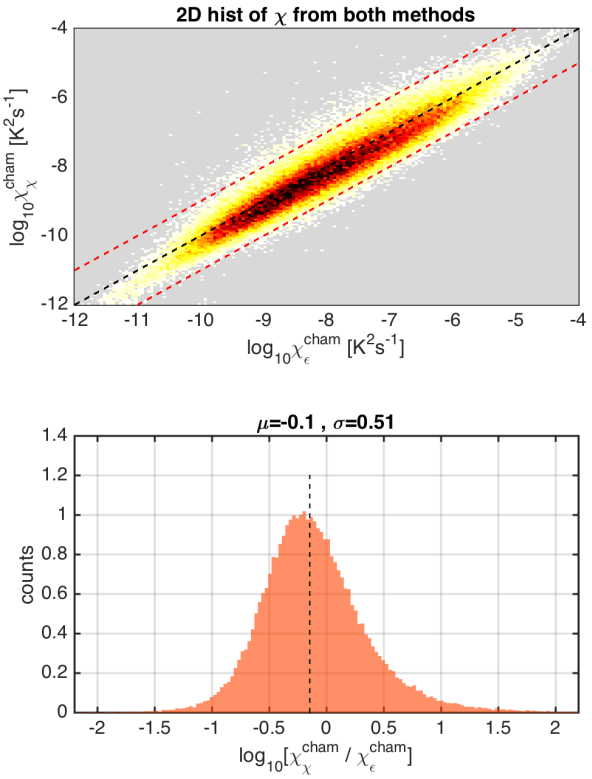

Figure 3.8. Top: 2D histogram of $log_{10}(\chi)$ from Chameleon (x-axis) and χpod method (y-axes). Values from each profile were averaged in the same 5m depth bins. Bottom: Normalized histogram of $\log_{10}[\chi_\chi^{cham}/\chi_\epsilon^{cham}]$. Vertical dashed line indicates the mean of the distribution.

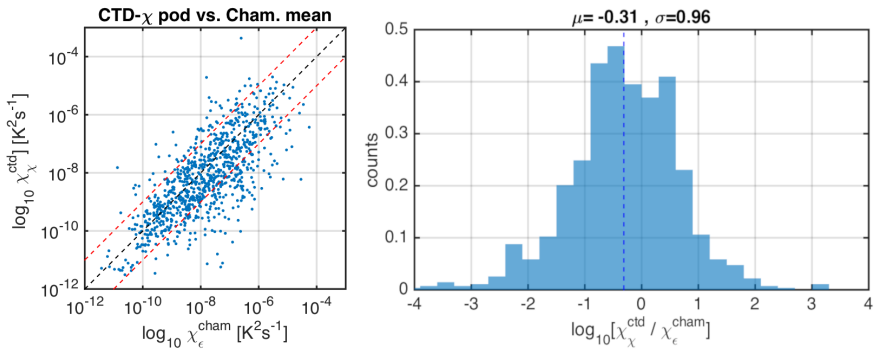

Figure 3.9. Left: Scatter plot of χ from CTD-χpod profiles versus the mean of bracketing Chameleon profiles. Black dashed line shows 1:1, dashed red lines represent the bounds for factor-of-ten agreement. Right: Normalized histogram of the log of ratios.

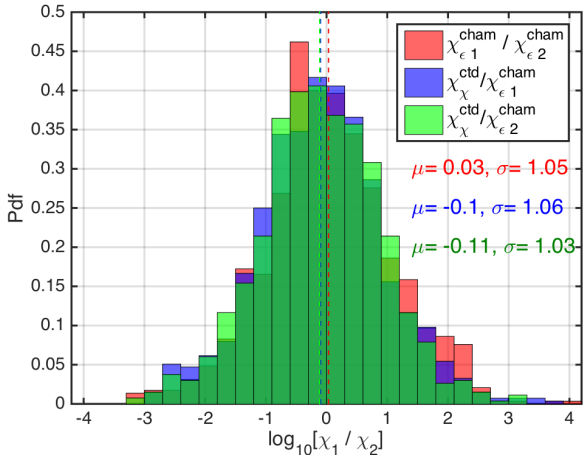

Figure 3.10. Histogram of log_{10} of the ratio of χ for nearby casts. The first set is for the before ($\chi_{\epsilon 1}^{cham}$) and after ($\chi_{\epsilon 2}^{cham}$) Chameleon profiles. The 2nd is CTD-χpod profiles (χ_{χ}^{ctd}) versus the before($\chi_{\epsilon 1}^{cham}$) profiles. The last is CTD-χpod profiles (χ_{χ}^{ctd}) versus the after($\chi_{\epsilon 2}^{cham}$) profiles. Dashed lines show the medians of each set. Note that bias is small/zero, and the variability (spread) between CTD/Chameleon is similar to the natural variability between Chameleon profiles.

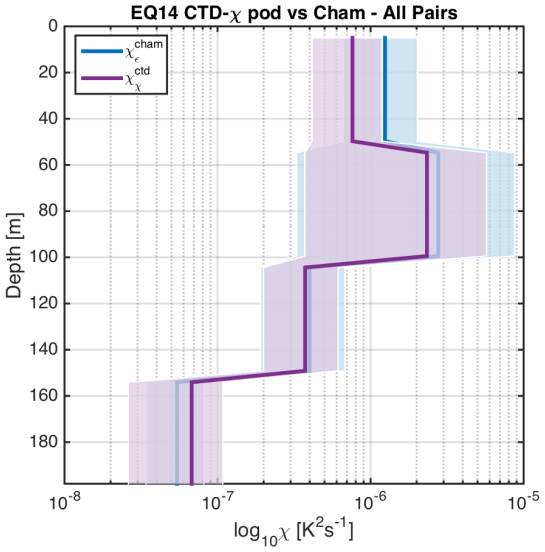

Figure 3.11. Time mean of χ for all CTD-χpod - Chameleon cast pairs, with 95% bootstrap confidence intervals.

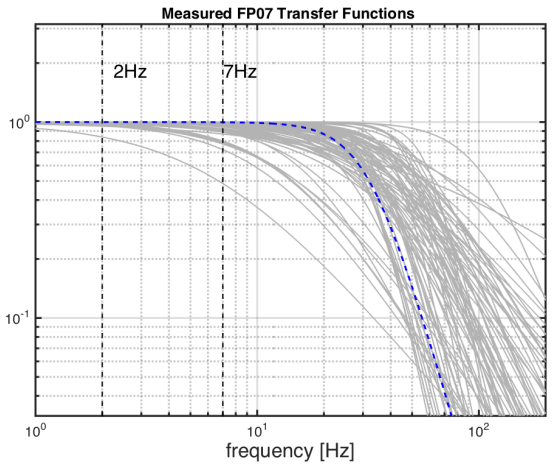

Figure 3.12. Measured FP07 thermistor transfer functions from historical database. Vertical dashed lines show the frequency range used in χpod method. Dashed blue line is a generic transfer function found to best represent the bulk of measured transfer functions.

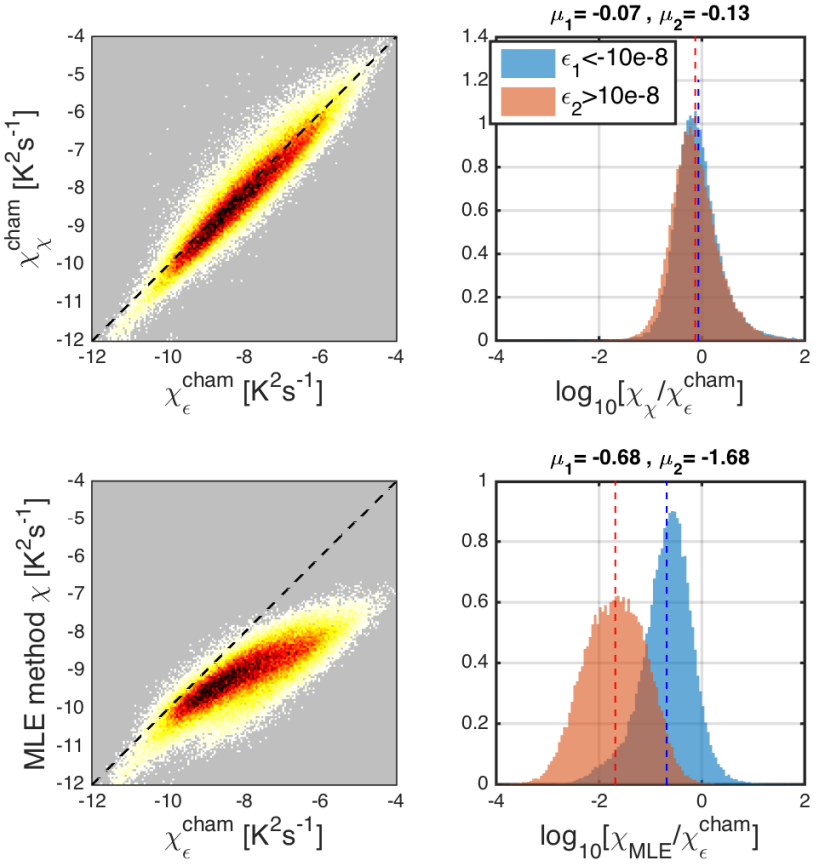

Figure 3.13. Left: 2D histograms of χ computed using the iterative χpod method (top) and the MLE fit (bottom) versus χ computed from Chameleon. Note that the MLE method underestimates χ at larger magnitudes. Right: Histograms of the log of ratios for different ranges of ϵ (values in W/kg). The mean of each distribution is given above.

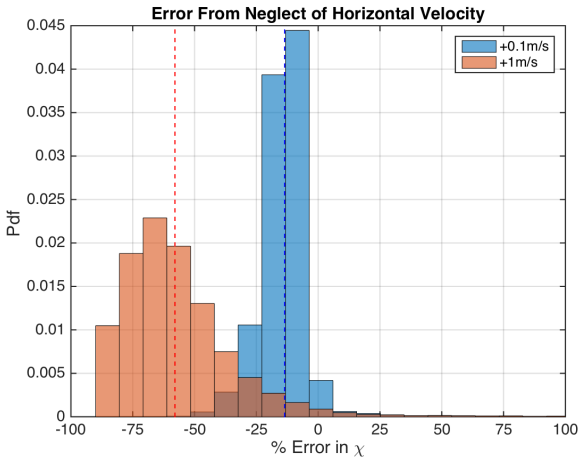

Figure 3.14. Histogram of % error for χ computed with Constant added to fallspeed, in order to examine sensitivity to fallspeed. Vertical lines indicate the mean of each distribution.

Chapter 4

Global Patterns of Bias in Ocean Mixing Parameterization Identified Through Unsupervised Machine Learning

Abstract

Turbulent mixing in the ocean is often parameterized in terms of the downscale energy transfer by internal waves. Expressed in terms of the vertical wavenumber spectrum of oceanic velocity shear (V_z^2) and isopycnal strain (ζ_z^2), the "finescale parameterization" relies on several parameters, including key assumptions relating to the spectral properties. Here we use an unsupervised learning model to identify spatial correlations between embedded parameters of the finescale parameterization based upon data from 1875 full-depth hydrographic profiles from 15 sections traversing the global ocean. The clustered patterns along the sections have marked horizontal and vertical spatial dependence associated with distinct modes of spectral variation. Two clustered regions are identified where the underlying spectra deviate significantly from the canonical Garrett-Munk (GM) spectrum, suggesting potential departures from implicit assumptions about the downscale energy cascade. Spectral composites in these two regions show intensification of variance in the low and high wavenumber regimes respectively, as well as distinction in overall spectral levels and geographic prevalence. Furthermore, these clusters are found to be associated with regions where parameterized estimates of the turbulent dissipation rate ϵ differ significantly (exceeding a factor of 5) from co-located in-situ observations measured using χ-pod temperature microstructure. Extending the methodology to other hydrographic datasets has the potential to reveal reasons for this parameterization bias and to identify the dynamical underpinnings leading to more robust parameterizations of oceanic turbulent mixing.

4.1 Introduction

Turbulent mixing plays a critical role in the overturning circulation of the global ocean, driving the vertical and horizontal transport of heat and tracers (Ganachaud & Wunsch, 2000; Wunsch & Ferrari, 2004). While mixing at the molecular level can be explicitly characterized by thermodynamic diffusion equations, the observed interior ocean stratification requires vigorous turbulent mixing that is 10-100 times stronger than that from molecular diffusion alone (e.g., Munk, 1966; Bryan, 1987; Talley, 2003; Cimoli et al., 2023), driven primarily through breaking internal waves (Polzin et al., 1997; Kunze et al., 2006a; Whalen, Talley, & MacKinnon, 2012; Waterhouse et al., 2014a; MacKinnon et al., 2017a). The strength of this turbulent mixing is governed by distinct physical and dynamical processes which result in rich geographical patterns of mixing throughout the global ocean. (Polzin et al., 1997; Naveira Garabato et al., 2004; Whalen, Talley, & MacKinnon, 2012; Waterhouse et al., 2014a; Whalen et al., 2018b).

Resolving the spatiotemporal patterns of turbulent mixing in the ocean from observations is significantly challenging owing to the intermittent nature of mixing. At present, the most accurate estimates of turbulent mixing come from specialized microstructure instrumentation deployed from ships (Polzin et al., 1997; St. Laurent et al., 2012; Naveira et al., 2019; Lele et al., 2021), on moorings (J. N. Moum & Nash, 2009), and autonomous platforms (Rudnick et al., 2013; Johnston & Rudnick, 2015; Shroyer et al., 2016). These microstructure instruments allow for estimates of kinetic energy dissipation rate (ϵ) and temperature gradient variance (χ) by measuring high frequency velocity and/or temperature gradients. The resolved turbulent gradient spectra in the inertial subrange of turbulence are then used to compute ϵ and χ (e.g., Oakey, 1982b; Gregg, 1999; Itsweire et al., 1993). However, global microstructure observations have sparse global spatio-temporal coverage (Waterhouse et al., 2014a).

In response to the low abundance of microstructure observations, the community has embraced a set of mixing parameterizations based upon internal wave-wave interaction theories called finescale parameterizations that allow for the estimate of ϵ from lower resolution temperature

and salinity data (Henyey et al., 1986; Gregg, 1989; Polzin et al., 1995). These parameterizations estimate turbulent dissipation of energy by estimating the rate of downscale energy transfer through wave-wave interactions by combining the measured internal wave spectral level and theoretical and empirical models of wave interactions. The applicability of finescale parameterizations on the more widely available oceanographic ship-based and Argo-based Conductivity Temperature Depth (CTD) and Lowered Acoustic Doppler Current Profiler (LADCP) data has drastically increased the spatial coverage of mixing estimates as well as our understanding of the spatial geography of mixing in the ocean (e.g., Whalen et al., 2015a; Kunze, 2017b) with overall broad agreement with measurements obtained from microstructure instrumentation (e.g., Polzin et al., 1995, 2014a; Whalen et al., 2015a; Whalen, 2021) Crucially for our work, the spectral energy level is estimated by comparing the *average* spectral level within a limited wavenumber band to the idealized Garrett-Munk (GM) model (Garrett & Munk, 1972; Munk, 1981). Since the finescale parameterizations are referenced to the GM model in their formulation of spectral energy transport through the internal wave vertical wave number space, large departures from the GM model are susceptible to engendering biased estimates (Polzin et al., 2014a).

Dissipation rates ϵ and related eddy diffusivities κ obtained from finescale parameterizations show overall broad agreement with measurements obtained from microstructure instrumentation (e.g., Polzin et al., 1995, 2014a; Whalen et al., 2015a; Whalen, 2021), however, some discrepancies and biases have also been previously documented (e.g., MacKinnon & Gregg, 2003; Waterman, Polzin, Naveira Garabato, Sheen, Forryan, Garabato, et al., 2014). The underlying assumptions of the parameterizations are violated in many regions of the ocean, such as in the surface mixed layer, or where turbulent mixing is controlled by double diffusion, hydraulic jumps and strong wave-mean flow interactions over rough topography (Waterman, Polzin, Naveira Garabato, Sheen, Forryan, Garabato, et al., 2014; Polzin et al., 2014a). There are also regions where the parameterized mixing rate does not match observations of turbulent mixing from microstructure measurements for unclear reasons. A hypothesis considered here is that deviations of the spectral shape or other properties of the internal wave spectrum from the

assumed GM form may be relevant (Müller & Liu, 2000; Polzin & Lvov, 2011), or variability in other individual parameters of the parameterization themselves, based on the local geography, topographic conditions and the presence of external forcing on the local internal wave field (Waterman, Polzin, Naveira Garabato, Sheen, Forryan, Garabato, et al., 2014; Chinn et al., 2016; Pollmann, 2020). Recently, both supervised and unsupervised learning approaches have been used across a variety of fluid mechanical applications to provide new insight into fundamental relationships and patterns of variability in our oceans (Giglio et al., 2018; Brunton et al., 2020; Callaham et al., 2021; Kaiser et al., 2022; Mashayek et al., 2022). In particular, clustering techniques have proven useful in generating insights and exploring existing oceanographic data, such as categorizing datasets of temperature-salinity profiles (e.g., Rosso et al., 2020; Jones et al., 2019; Boehme & Rosso, 2021), classifying global ecological marine provinces (Sonnewald et al., 2020) and identifying dominant dynamical balances in global ocean circulation models (Sonnewald et al., 2019).

In this study, we employ unsupervised learning to characterize a parameter-space associated with large mismatches between finescale and microstructure observations of oceanic turbulent mixing. Drawing inspiration from unsupervised learning approaches in the spectral domain applied to earthquakes and astronomical observations (C. W. Johnson et al., 2020; Ivezic et al., 2014), we use latent features extracted from oceanic shear and strain spectra as well as other variables (features) used in the formulation of finescale parameterizations to identify regions of distinct co-variations connected to properties of turbulent mixing in the ocean and underlying dynamics of internal wave-wave interactions. The curated hydrographic dataset used in the study is described in Section 4.2, with the underlying principles of finescale parameterizations, feature development, dimensionality reduction and clustering model laid out in Section 4.3. Finally, we describe the geography and spatial characteristics of the clustering results and the interpretation of the results in the context of the underpinning finescale parameterization for estimating turbulent mixing in the ocean in Sections 5.3 and 5.4.

4.2 Data

4.2.1 Ship-based Hydrographic Data

The principal data used in this study are 1875 profiles of high quality full-depth CTD and LADCP data collected along 15 hydrographic sections from around the globe as part of either the Climate and Ocean Variability, Predictability and Change (CLIVAR) or the Global Ocean Ship-based Hydrographic Investigations Program (GO-SHIP) programs between the years 2000 and 2021 (Figure **??**, Table 4.1). The horizontal station spacing between CTD casts is nominally 55 kilometers, with stations spaced closer in regions of interest (e.g. trenches, rough topography, boundary current regions). Vertically, the CTD-cast data used here include the profile from 500m down to a maximum depth, usually 6000m or within 10-20m from the seafloor. The top 500m of the profiles are not considered in order to remove the surface mixed layer. Conservative temperature (θ), squared buoyancy frequency (N^2), and potential density ρ_θ are calculated from the CTD instrumentation using the Gibbs-Seawater Oceanographic Toolbox (McDougall, 2011; Jackett & McDougall, 1997). The publicly available LADCP data product has an 8-meter vertical resolution pre-processed using procedures laid out for the GO-SHIP program (Visbeck, 2002; Thurnherr et al., 2010). The LADCP data product for all 15 sections contains data binned at a nominal 1-meter resolution and with horizontal (U,V) and vertical component (W) of ocean velocity from the ocean surface down to the maximum CTD depth. All LADCP data obtained are co-located with CTD data for each CTD cast along the sections.

4.2.2 Microstructure mixing estimates from CTD-mounted χ-pods

Estimates of ϵ from rosette-mounted microstructure χ-pods taken along the P06 section were obtained from cchdo.edu (see data availability statement). ϵ was estimated using the high wavenumber temperature gradient fluctuations dT'/dz measured by the 100Hz FP07 thermistor probe following the methods of J. N. Moum & Nash (2009) and Lele et al. (2021). The data have all been processed and cleaned including (1) removing any points with platform-induced

noise, (2) calculating dissipation rates of the temperature variance, χ in 1-s bins, (3) any data in regions of very weak stratification where $\overline{dT/dz}$ is less than 10^{-4} K m^{-1} were removed, (4) ϵ was calculated from χ following Osborn & Cox (1972a) and (5) data were binned into 200-m half overlapping segments, ensuring binned averages comparable binned finescale parameterization data (see Section 4.3.1).

4.3 Methods

4.3.1 Estimating Mixing from Finescale Parameterizations

Profiles of ϵ and κ are estimated from 1875 CTD stations containing a total of *64816* spectral estimates of internal wave shear $\langle V_z^2 \rangle$ and strain $\langle \zeta_z^2 \rangle$ variances using the finescale parameterization method following Gregg (1989); Henyey et al. (1986); Polzin et al. (1995); Kunze et al. (2006a). Shear and strain variances are computed from CTD temperature and salinity and LADCP horizontal velocities profiles along the sections. Variance levels relative to the canonical Garrett-Munk (GM) spectra (Munk, 1981) are used to relate vertical turbulent eddy diffusivity (κ) to the turbulent kinetic energy dissipation rate ϵ via the Osborn (1980a) relationship $\kappa = \Gamma \frac{\epsilon}{N^2}$, wherein mixing efficiency Γ considered to be nominally 0.2 (Polzin et al., 2014a) and N is the buoyancy frequency. This relationship is further broken down as:

$$\kappa = \kappa_0 E_{v_z} h(R_\omega) J(f/N), \tag{4.1}$$

with

$$E_{v_z} = \frac{\langle V_z^2 \rangle^2}{\langle V_z^2 \rangle_{GM}^2} \tag{4.2}$$

$$h(R_\omega) = \frac{3(R_\omega + 1)}{2\sqrt{2} R_\omega \sqrt{R_\omega - 1}} \tag{4.3}$$

$$J(f/N) = \frac{f \cosh^{-1}(N/f)}{f_{30} \cosh^{-1}(N_0/f_{30})} \tag{4.4}$$

where $\cosh^{-1}$ is the inverse hyperbolic cosine function, and constant values $\kappa_o = 5 \times$

$10^{-6}\mathrm{m}^2\mathrm{s}^{-1}$, $f_{30} = 7.292 \times 10^{-5}$ rad s^{-1} and $N_0 = 5.2 \times 10^{-3}$ rad s^{-1}, where f_{30}, N_o and κ_o denote the Coriolis frequency at 30^oN latitude, the canonical GM buoyancy frequency and background diffusivity respectively.

The angle brackets in Equation 4.1 indicate integration of LADCP-derived shear spectra over a wavenumber band capturing finescale internal wave shear variance (Gregg, 1989; Polzin et al., 2014a). The factor $J(f/N)$ in Equation 4.2 is a latitudinal correction applied to account for weaker turbulent dissipation rates found near equatorial regions (Henyey et al., 1986; Gregg et al., 2003), while the factor $\mathrm{h}(R_\omega)$ in Equation 4.3 accounts for deviations from the GM spectrum based on the frequency content of the internal wave field given by R_ω, reducing to unity when R_ω is set to the canonical GM value of 3 (Polzin et al., 1995). The dependence on strain (ζ_z) is introduced in the parameterization through the shear to strain variance ratio $R_\omega = \frac{\langle V_z^2 \rangle}{\bar{N}\langle \zeta_z^2 \rangle}$, a measure of the internal wave fields aspect ratio or frequency content. This, under a monochromatic wave assumption can be summarized as:

$$\frac{\omega}{f} = \sqrt{\frac{R_\omega + 1}{R_\omega - 1}} \tag{4.5}$$

representing the contribution of near-inertial ($\omega / f \approx 0$) to non-near-inertial internal waves in the domain.

Profiles of ϵ and κ are calculated at each CTD station along the section from 200 m half-overlapping segments in depth using the parameterization given by Equation 4.1. It is important to note however, that these parameterized estimates of diffusivity κ and dissipation rate ϵ do not sufficiently resolve mixing processes in the boundary layer, hydraulic jumps, double diffusion or internal wave driven turbulence in regimes with significant wave-mean flow interaction (Waterman, Polzin, Naveira Garabato, Sheen, Forryan, Garabato, et al., 2014), and they produce spatially averaged estimates of mixing over multiple wave periods.

4.3.2 Feature Development

Here, we define and extract features from various attributes of the parameterization, to examine and understand the patterns of their cross-covariances as they relate to internal-wave driven mixing in the global ocean using unsupervised machine learning.

Building upon the parameterization in Equation 4.1 as the basis for feature development, we focus on measured shear and strain spectra which are primary components of the parameterization. Buoyancy frequency normalized shear [ϕ_{V_z}] and strain [ϕ_{ζ_z}] wavenumber spectra are calculated from the Fourier transforms of the vertical LADCP and CTD data for shear and strain respectively. To calculate shear variance $\langle V_z^2 \rangle$, segments are constructed starting from the bottom in 320m half-overlapping windows, each tapered with a 10% sine^2 window function to obtain its vertical wavenumber spectra (Kunze et al., 2006a), which are then integrated between wavelengths of 320m and 150m to avoid high wavenumber instrument noise contamination(Kunze et al., 2006a).

Strain is calculated from the buoyancy frequency as $\zeta_z = (N^2 - \bar{N}^2)/\bar{N}^2$, where the mean stratification $\bar{N^2}$ is determined from quadratic fits to the profile segments (Kunze et al., 2006a). Further, the strain variance is calculated by integrating the strain power spectrum between wavelengths of 150m and up to 10m while also satisfying strain variance $\langle \xi_z^2 \rangle < 0.2$ to avoid underestimating the variance through oversaturation of the spectrum (Gargett, 1990). $\langle V_z^2 \rangle$ and $\langle \xi_z^2 \rangle$ values are then normalized by the integrated GM model spectrum over the same respective bandwidths to represent the energy density in the internal wave field in the units of the GM energy density (Gregg & Kunze, 1991; Munk, 1981).

Each GM-normalized shear and strain spectrum is further normalized with its respective shear and strain variances across the finescale integration band to de-emphasize the known relationship between internal wave spectral level and stratification (Gregg, 1989; Kunze, 2017a). Further, we consolidate the dominant types of spectral variability by reducing the dimensionality of the data using Non-Negative Matrix Factorization (NMF) decomposition (Figure **??**; described further in Section 4.3.2).

NMF Decomposition of Shear and Strain Spectra

While unsupervised learning could in theory identify clusters in any N-dimensional space, the quality of the resultant clustering formulation is directly proportional to the number of data points in the N-dimensional space. It is therefore prudent to introduce a low-rank approximation of the input N-dimensional space to reduce redundant co-variances in the data. Factor analysis and principal component analysis (PCA) are two of the many classical methods used to accomplish the goal of dimensionality reduction and detecting structures among the variables. Often the data to be analyzed are non-negative, and the low-rank data are further required to be comprised of non-negative values in order to avoid contradicting physical realities. Therefore, we reduce the dimensionality of the input spectral data using non-negative matrix factorization (NMF) (Lee & Seung, 1999; Berry et al., 2007) to decompose high-dimensional spectra of shear and strain into lower-dimensional latent spectral representations (Figure **??**b). These low-dimensional embeddings (Figure **??**c (green box),4.2a-d) are further aggregated into a feature matrix along with other auxiliary features (Figure 4.2e-g) and are then used as feature inputs to the GMM model (Section 4.3.2,Figure **??**c).

The decomposition aims to approximate the input data matrix $\mathbf{X}$ consisting of non-negative elements, comprised of n individual spectral data points each with m wavenumbers, into a low-rank non-negative approximation consisting of a latent feature matrix W and corresponding hidden coefficients H. This can be expressed as: $\mathbf{X}_{[n\times m]} \approx \mathbf{W}_{[n\times p]}\mathbf{H}_{[p\times m]}$ (Figure **??**b). The matrix $\mathbf{W}$ can be regarded as spectral end-members whose linear combinations with the coefficient matrix $\mathbf{H}$ reconstruct the original data matrix $\mathbf{X}$. The quality of the approximation of $\mathbf{X}$ is measured using the Frobenius norm $||X - WH||_F^2 = \sum_{ij}(X - WH)_{ij}^2$ and the optimization algorithm is carried out using the NMF implementation in the Python library *scikit-learn* (Pedregosa et al., 2011). In this study the input data matrix $\mathbf{X}$ for both shear and strain spectra consists of n = 67816 total spectra respectively obtained along the 15 GO-SHIP hydrographic section descibed earlier in Section 4.2.1.

It is conceivable that the reconstruction of the original spectra gets progressively better with the increase in the number of NMF components (p) i.e. the addition of more latent dimensions. In theory, the number of latent dimensions is inversely proportional to the reconstruction error. Hence $p = m$ would result in a perfect reconstruction as the additional latent dimensions could in theory encode more of the information present in the original input matrix **X**. However, here we choose $p = 2$, i.e. *two* latent dimensions to represent high dimensional ($m = 10$) shear and strain spectra as it results in the greatest decrease in the reconstruction error with respect to the number of latent dimensions while still preserving relevant spectral characteristics (not shown). Although increasing the number of latent dimensions beyond two results in a better reconstruction of the original spectral matrix **X**, it can be counter-productive from an unsupervised learning standpoint as it can lead to inconsistencies in the final solutions produced by the clustering model often referred to as the "curse of dimensionality" (Bishop, 2006).

Final Feature Matrix (F)

Two NMF components each of the shear and strain spectra are aggregated into a "feature matrix" F (Figure **??**c) and used as input to an unsupervised learning model (Section 4.3.3). The sensitivity of the final results (Section 5.3) to the introduction of additional relevant features in the feature matrix- including the shear variance $\langle V_z^2 \rangle$, buoyancy frequency [N] and internal wave aspect ratio R_ω, all derived from the parameterization in Equation (4.1) is explored in Section 4.4.3. *Note*: The primary results discussed hereafter other than those specifically noted, describe the results of using only the 4 NMF components, two derived from the shear spectra and two derived from the strain spectra (Figure **??**c green box, 4.2a-d).

4.3.3 Unsupervised Learning of Turbulent Mixing Data

An unsupervised machine learning clustering technique is used to identify groups with similar shear and strain spectra characteristics by applying a Gaussian Mixture Model (GMM)

framework (e.g., Maze et al., 2017). The algorithm assumes the dataset with D features can be explained as derived from a mixture of K Gaussian distributions in D dimensions, where each feature represents a new dimension describing the data. The GMM model computes the parameters mean μ_k, covariance Σ_k and weights λ_k using the Expectation-Maximization algorithm in order to maximize the likelihood of the data X belonging to cluster k, denoted by the conditional probability distribution $p(k|x)$. The probability that data X belongs to the k^{th} component of the mixture of Gaussian distributions is given by:

$$p\left(k|x\right) = \frac{\lambda_k \mathcal{N}(x;\mu_k,\Sigma_k)}{\Sigma_{k=1}^{K} \lambda_k \mathcal{N}(x;\mu_k,\Sigma_k)} \tag{4.6}$$

with the multivariate normal Gaussian distribution given by:

$$p(x;\mu_k,\Sigma_k) = \frac{1}{\sqrt{2\pi^D|\Sigma|}} \exp\left[-\frac{1}{2}(x-\mu_k)^T\Sigma^{-1}(x-\mu_k)\right] \tag{4.7}$$

The conditional probability $p(k|x)$ in Equation 4.6 over all clusters k equals 1. The GMM algorithm assigns the cluster label k to the component for which this conditional probability is maximum i.e. $k = \text{argmax}_x\, p\left(k|x\right)$. We further mask out data with a maximum conditional probability less than 70% i.e. $k = \text{argmax}_x[p\left(k|x\right) > 0.7]$ (Figure 4.4a, gray) to avoid the possibility of having cluster labels with similar probability densities potentially near strong eddy or frontal forcings (Jones et al., 2019).

The choice of the number of clusters is a subjective one, and depends on the desired application of the clustering problem. The number of optimal clusters can vary widely based on the criteria used for convergence, tuning and choice of hyperparameters used (such as the type of covariances), as well as the amount of data and choice of feature inputs given to the clustering algorithm. Dimensionality reduction for shear and strain spectra using NMF decomposition

and clustering with the GMM model in this study were implemented using open-source python machine learning library scikit-learn (Pedregosa et al., 2011). We validate the optimal number of clusters outputted from the GMM model initialized with a "full" covariance matrix based on Akaike and Bayesian information criterion (AIC and BIC) scores (Schwarz G, 1978; Konishi et al., 2004). The AIC and BIC scores were computed for the entire feature matrix F created with the entirety of the data collected from 15 sections (not shown) as well random subsets of it for K=2 to K=14. The scores computed from 50 bootstraps of the random feature matrix subsets show a minimum between K=7 and K=9 clusters (Figure 4.7, purple shading). This conclusion is consistent when using a different metric for optimal clustering, the silhouette coefficient (Rousseeuw, 1987) (not shown). Although we use K=7 as the optimal number of clusters, the final results described in Section 4 are quantitatively the same, regardless of the choice of the number of clusters between K=7 and K=9 (Section 4.4.3).

4.4 Results

Seven distinct clusters of data are identified using the GMM model, which we explore to gain insight into the physical and geographical patterns relevant to turbulent mixing. We also consider the spatial structure of clusters and their correspondence with patterns of mismatch between finescale and microstructure-derived estimates to further contextualize the results. The feature matrix F input to the GMM model is comprised of only the two NMF-components of the normalized shear spectra and two NMF-components of the normalized strain spectra (Figure **??**c, green box) for approximately 70,000 data points, each representing a 100 m vertical segment of data collected from 1875 profiles along 15 GO-SHIP sections (Figure 4.2a-d, 4.3a). The GMM is constrained to 7 clusters, hereafter discussed and referred to by the arbitrarily assigned cluster number. In terms of relative proportions of the assigned cluster labels- Cluster 5 was the most prevalent, followed by Clusters 4, 3, 7, 2, 1, and finally 6 (Figure 4.3d).

It is insightful to disentangle and isolate the original raw input data associated with each

cluster to identify patterns that could potentially be linked to underlying physical mechanisms. We use the final clustering assignments to construct a composite average of the original "raw" shear and strain spectra belonging to each of the 7 clusters prior to any normalization and NMF decomposition (Section 4.3.2). The spectral data are "raw" in the sense that these spectra are the basis of the shear and strain variance ($\langle V_z^2 \rangle$, $\langle \zeta_z^2 \rangle$) calculations in the finescale parameterization described in Equations 4.1 and 4.2. At the individual level, the spectral energy density of the raw spectra across all 15 sections span orders of magnitude and appear to have incoherent geographical distributions and spatial dependence. However, considering the individual spectra combined with their corresponding clustering labels, we find that the average composite spectra (Figure 4.4 d, e) have distinct spectral shapes and unique slope and roll-off characteristics in vertical wavenumber space. These perceptible spectral characteristics combined with the cluster spatial distributions and dependence hint at the potentially differing underlying physical mechanisms responsible for the non-linear downscale energy transport and turbulent mixing in these regions.

4.4.1 Identification of Non-GM Spectral Conditions & Parameterized Mixing Bias

The finescale parameterization laid out in Equations 4.1-4.4 aims to represent nonlinear spectral energy transport in the vertical wavenumber domain based on arguments set forth by (Garrett & Munk, 1972, 1975, 1979), requiring careful treatment of deviations from this framework. The intent of parameterization is to encapsulate the non-linear internal wave-wave interaction within a finite amplitude and vertical length scales not only well-resolved by CTD and LADCP instrumentation (used for shear and strain calculation) and relatively free from contamination from instrumental noise or background stratification, but also from the effects of competing physical and dynamical processes such as near-boundaries mixing, wave-mean interaction, shear-driven mixing, double diffusion, which could potentially short-circuit the downscale energy transfer and the basis of the parameterization. In observations (e.g., Gregg & Kunze, 1991; Polzin et al., 1995; Brink, 1995; Eriksen, 1998), the wavenumber shear spectra at

smaller wavenumbers (<0.1 cpm) are relatively white (flat) with roughly equal distribution of shear variance in this regime. The transition to turbulence occurs at length scales greater than 1 cpm governed by non-linear dynamics and shear instability driven non-local energy transport (Gargett et al., 1981). The finescale parameterization is employed to predict the turbulent dissipation from energy transport calculated at the intermediate scales (<0.1cpm, Figure 4.4c, d gray vertical lines). Here, large deviations from GM-model prescriptions can induce biases in the estimates and are potentially emblematic of additional physical processes at play beyond wave-wave interactions (Polzin et al., 2014a).

Composite averages of shear and strain spectra computed within each cluster across all 15 sections (Figure 4.4c,d, Supporting Information Figure S3,S4) reveal *two* clusters (Cluster 1 and 7) with spectral characteristics differing significantly from the other clusters and from GM model spectra. Average shear spectra in Cluster 1 shows spectral levels comparable to other clusters but are characterized by a steep ("red") slope compared to GM, with spectral roll-off at much lower wavenumbers and larger vertical scales than the other composites. At approximately the same vertical scales, shear spectra belonging to Cluster 7 show an enhancement in shear spectral power where the spectra appear "blue" and roll-off quite steeply after shear-enhanced hump. The shear-to-strain ratios (R_ω) implied by the Cluster 1 composite suggest a decrease in R_ω at higher vertical wavenumbers which could be interpreted as an increased contribution of high-frequency waves (Equation 4.4). Studies have suggested that this is also possible due to the presence of quasi-permanent finestructure from rotating stratified turbulence (Polzin et al., 2003; Polzin & Ferrari, 2004).

The deviation from the assumptions about downscale spectral energy transport across wavenumbers in the parameterization is explored by comparing the ratio of the finescale parameterized estimates of turbulent dissipation rate ϵ to the concurrent co-located in-situ microstructure measurements of ϵ from CTD-mounted χ-pods (Lele et al., 2021) along the 2017 occupation of the P06 line within each cluster. The ratio of the two different estimates $\log_{10}\left(\frac{\epsilon_{\text{fine}}}{\epsilon_{\chi\text{pod}}}\right)$ or the "mixing bias" along the P06 section where positive (negative) values indicate finescale

over-prediction (under-prediction) compared to measurements from $\chi-$pods (Figure 4.4a). The clustering from the GMM model together with the mixing bias along the P06 are combined to produce estimates of average bias for each cluster (Figure 4.4c). The averaged mixing bias and 95% confidence intervals for clusters 2-6 fall well within a factor 5 (Figure 4.3c, dashed black line). Clusters 1 and 7 however show a high and a low bias respectively with average disagreement between finescale and χ-pod estimates as large as an order of magnitude along P06. Further, the averaged spectral properties of the clusters also reveal marked deviations from their respective canonical GM shear and strain counterparts (Figure 4.4d, e). The inconsistencies between the rate of downscale energy transfer as prescribed by the GM model (e.g. Cluster 1), and possible shear-enhancing high-wavenumber energy sources (e.g. Cluster 7), serve as useful indicators of potential physical-dynamical processes unresolved in the finescale parameterizations.

The formulation of the finescale parameterization in Equation 4.1 states that diffusivity κ and dissipation rate ϵ (through the Osborn relation, Section 4.3.1) are proportional to the total integrated shear variance from shear spectra $\langle V_z^2 \rangle$. Considering this relationship between $\langle V_z^2 \rangle$ and ϵ, the mixing biases between finescale parameterized observed along P06 between ϵ_{fine} and $\epsilon_{\chi\text{-pod}}$ likely occurs as a result of the overestimation (underestimation) of $\langle V_z^2 \rangle$ in locations where Cluster 1 (Cluster 7) occur (Figure 4.4f). In the case of Cluster 1, a "redder" than GM-like spectra (Figure 4.4e, f, pink line) results in an overestimation of shear variance due to the assumed spectral shape being GM-like, or flat (Figure 4.4f, pink shading). The overestimated shear variance through the relationship described in Equation 4.1 engenders a highly inflated estimate of ϵ_{fine} by almost an order of magnitude (Figure 4.4c). A reverse mechanism occurs in the case of Cluster 7 in which an increasingly positive slope ("bluer") compared to the GM-like spectra, leads to an underestimation of $\langle V_z^2 \rangle$ and consequently a depressed estimate of ϵ_{fine}.

Using limited modes of spectral variation through the NMF decomposition along 15 sections as inputs to the GMM model, we isolated *two* regions where underlying shear and strain spectra have characteristics to induce biases in parameterized mixing estimates. Spectral properties obtained in other process-based studies and certain localized environments have

shown similarities to spectral features we identify here using a global dataset. Several different physical mechanics have been proposed in which non-white gradient spectra are associated with physics unresolved or problematic for finescale estimation (Kunze et al., 2002; Klymak et al., 2008; Polzin & Lvov, 2011; Brink, 1995; Eriksen, 1998). For example, well-resolved spectra from a study around the Kergulean Plateau region (Waterman et al., 2013; Waterman, Polzin, Naveira Garabato, Sheen, Forryan, Garabato, et al., 2014) associated with finescale overestimation, exhibit steeper and rapid roll-offs at lower wavenumber attributed to strong wave-mean interactions in the region, similar to spectra found in Cluster 1. Similarly, generation or reflection at boundaries can inject shear at higher wavenumbers with loss of low-wavenumber energy and gain in high-wavenumber energy (Eriksen, 1985), as seen in composites from Cluster 7. Although diagnosing and interpreting the plethora of possibilities in the physics driving such peculiarities in the spectral energy transports in wavenumber space is beyond the scope of the paper- we further aim to prognosticate the spatial structure distribution of regions of potential finescale mixing bias along these sections.

4.4.2 Geographical Distribution

The spatial distribution of the clusters shows a rich and varied geographical distribution along the 15 sections considered here (Figure 4.3a). From a high-level perspective, the clustering reveals a rough dependence on stratification as seen by the alignment in most sections with the contours of buoyancy frequency along those sections (Figure 4.3a, black lines). Even though the inputs to the GMM consist of buoyancy-normalized spectral data that have been standardized by their respective integrated variances in order to diminish the a priori stratification dependence, the clustering patterns nevertheless reveal an ostensible relationship with buoyancy frequency.

In addition to the geographical cluster assignments by individual sections, more insight into the distinguishing characteristics of the clustering patterns can be gained by looking at the spatial variations in probability densities of each cluster vertically (depth and height-above-bottom) and horizontally (along-section) for each section individually, as well as by computing

composites encompassing all 15 sections (Figure 4.3 [b-c,e-f] 4.5, 4.6, Supporting Information Figure S1-S2).

The upper ocean was dominated by clusters 2, 3 and 4, each showing similar vertical distributions, with some differences in their zonal and meridional distributions. Cluster 2 forms the majority of clusters within the Southern Ocean, as seen by the increase in prevalence southward of 55^oS along S4P, I06 and P16S , and the peak of the latitudinal distribution from the zonal composite found around 62.5^oS (Figure 4.3e). No distinct patterns emerge in the zonal and meridional distribution of cluster 3 and 4, suggesting minimal geographical precedence (Figure 4.3e, f). In depth, all three clusters become more prevalent closer to the seafloor (Figure 4.3c), resulting in peaks around 3000m, also reflecting the variations in bathymetry of the sections (Figure 4.3b). The presence of Cluster 2 in the Southern Ocean and along other sections near the bottom bathymetry for example, along the P06, P02 and A20 (Supporting Information Figure S2) is consistent with regions of low stratification and is seen clearly in the contours of buoyancy frequency along those sections (Figure 4.3a, black lines)

Above the ocean bottom, the analysis found an increase in the relative abundance of clusters 5 and 6. These two clusters are prominently found in the upper ocean along most sections between 500m and 2000m. Cluster 6 is the least prominent of the assigned labels and forms only 7.8% of the total assigned clusters, and is mostly found in the upper ocean, typically between 1500m and 2000m in the Atlantic Ocean (e.g., a13, a16n 16s and a10 lines). Cluster 5 is the second most common upper ocean cluster other than Cluster 1, with no notable zonal preference.

Cluster 1, associated with a more “red” shear spectra, is predominately found in the upper ocean along most sections, existing primarily between 500-1500m depth (Figure 4.3 b), with the notable exception in the Ross Sea (S4P) and Gulf of Mexico (A20) which show a second mid-depth around roughly 4000m (Figure 4.3a, Supporting Information Figure S1). In addition, the zonal section composite also reveals an increased proportion of Cluster 1 along the Equator, with a clear peak observed within 5 degrees of the equator. In addition, the cluster is found most often in the subtropics with it rarely observed at high latitudes (Figure 4.3e). Meridional

variability in Cluster 1 is observed with a vast preponderance in the Southern Hemisphere's subtropical Atlantic and Eastern Pacific (Figure 4.3f).

Cluster 7, associated with a more "blue" shear spectra with enhanced energy at wavenumbers between 150-100 m,is distributed in the mid to deep oceans, forms roughly 10.4% of the total cluster labels along the 15 sections (Figure 4.3d) and is most prevalent above the bottom bathymetry with a peak around 500m from the bottom bathymetry (Figure 4.3c). Zonally, an increased proportion of cluster 7 is found in the Southern Ocean, scattered vertically throughout the sections, with cluster 7s found from the surface all the way down to the bottom topography (e.g. S4P).

4.4.3 Sensitivity of GMM to Number of Clusters [K] and additional feature inputs[d]

To test the robustness of the findings discussed above, we explore the sensitivity of this study to two key analysis choices. First, the effect of constraining the number to cluster to 7 is tested, and second, the effect of adding additional features to the GMM model is explored.

The analysis was run with a range of fixed number of clusters (K) ranging from 2 to 14. The optimal number of class labels requires model hyperparameter tuning, and the results are shown by the BIC scores (Figure 4.7). The BIC score had a minimum at K=7, but with some ambiguity for K=7-9. Here, we discuss sensitivity of our final results and conclusions to the clustering produced by the GMM model with the same four spectral inputs inputs, but with K=8 (Labels 0-7) as the optimal number of clusters here. The clustering distribution using K=8 and four inputs is overall very similar to the distribution with K=7. The additional 8^{th} class label is assigned to regions in the upper ocean and seems to split regions assigned to Cluster 1 in Figure 4.3a into two regions with labels 4 and 6 (Supporting Information Figure S5a).

This is further supported by the mean strain and shear spectra calculated from composite averages of individual cluster labels across the whole dataset (Supporting Information Figure S5b,c). Clusters 4 and 6 are associated with shear spectra with negative slopes whereas Cluster 5

(similar to Cluster 7 in Figure 4.3a) has a positive slope. Further, we see a similar association of finescale biased ϵ with regions in Clusters 4 and 6 over-predicting ϵ, while regions within Cluster 5 under-predict ϵ compared to measurements from χ-pods along the P06 section. Similarly, we tested K=9 (not shown) and it did not change the key findings of this study. Thus, while minor qualitative differences are to be expected with clustering assignments for each of the clusters with the results discussed in Figure 4.3 and 4.4, we do not find any quantitative differences in the iteration of results discussed above with the final conclusions of the study.

Second, the sensitivity of the final results to the incorporation of additional features as inputs to the GMM model is explored. The decision boundaries delineating one cluster from the next in the GMM model is a function of the means and covariances that describe the multi-dimensional Gaussian distributions. In general, addition or subtraction of feature inputs to the clustering model, aside from varying the dimensionality of the clustering space, can greatly affect these means and covariances and as a consequence the delineation and distribution of individual clusters in space. In an effort to critique the final results as not merely serendipitous artifacts attributable to the choice of feature inputs, various permutations of feature inputs to the GMM are explored, all derived from parameters in the finescale parameterizations (Section 3.1, Equations 1-5). We compare our main results to a GMM run using seven feature inputs consisting of four shear and strain spectra NMF decompositions, shear variance $\langle V_z^2 \rangle$, buoyancy frequency (N) and the internal wave aspect-ratio R_ω (Figure 4.2a-g) with seven output clusters (Labels 0-6).

Compared to the four feature run presented in the main text, the seven feature run produces clusters that are highly correlated to buoyancy frequency as seen in the alignment with buoyancy frequency contours along most of the 15 sections (Supporting Information Figure S6a, black solid lines). The results also show an overall higher posterior probability of clustering assignment as seen in the reduction in probability mask applied for posterior probabilities less than 70% (Supporting Information Figure S6a, gray mask). However, computing averaged strain and shear spectra composites for each cluster as before shows two clusters associated with large deviations from the GM-model shape (Supporting Information Figure S6b,c, Clusters 2 and

Cluster 4). Biases in finescale ϵ estimates also exist for the same two clusters with regions along Cluster 4 overpredicting and regions along Cluster 2 underpredicting ϵ compared to observations from χ-pods along the P06 section (Supporting Information Figure S6d). With no significant quantitative differences in the results relating to the finescale bias, we re-centered the focus of the main text on describing and discussing the results from the four-feature GMM output (Figure 4.2a-d).

4.5 Conclusions

In this study, we use a novel unsupervised learning approach with a Gaussian Mixture Model (Jeff A. Bilmes, 1998; Bishop, 2006) to cluster and identify patterns of turbulent mixing-related features derived from fundamental constituents of finescale parameterizations of internal wave-driven turbulent mixing in the ocean using a global dataset of ship-based hydrographic CTD and LADCP data collected on 15 GO-SHIP lines. Using an NMF decomposition of oceanic shear and strain spectra, we extracted spectral features consisting of encoded information about spectral level, shapes and slopes (Section 4.3.2,Figure **??**,4.2). These features once aggregated into a feature matrix are clustered using the GMM model into seven different domains characterizing and delineating their collective variation in the N-dimensional space represented by the extracted features. The class labels roughly align with stratification in the ocean on average vary with depth and height-above-bottom across the global ocean. Latitudinal and longitudinal variations among the clusters are more convoluted.

Further, we explore the implications and potential effects of spectral deviations in wavenumber space from the canonical Garrett and Munk (GM) internal wave spectrum (Garrett & Munk, 1972, 1975, 1979), for application of the finescale parameterizations to global data collected along 15 GO-SHIP sections. We identify the average composite shear and strain spectra associated with each of the seven clusters revealing two clusters (Cluster 1 and Cluster 7) associated with distinct spectra differing significantly from both the other composites and

GM model in their wavenumber distribution of shear and strain spectral energy. Since the wavenumber distribution dictates the rate of energy transport and downscale energy transfer from large to smaller scales and ultimately to wave-breaking scales, the spectral characteristics within each cluster are ultimately tied to underlying physical mechanisms at play for turbulent mixing to occur in those regions. While uncovering the underlying mechanisms at play driving each cluster's spectral distribution is beyond the scope of this paper, we explore the robustness of mixing estimates obtained from finescale parameterizations in these regions further.

Studies have previously found large biases in finescale parameterized estimates where physical and dynamical environments short-circuit the underlying assumptions of the parameterizations, for e.g. regions in the surface mixed layer, near boundaries or where turbulent mixing is controlled by double diffusion, hydraulic jumps and strong wave-mean flow interactions over rough topography (Waterman, Polzin, Naveira Garabato, Sheen, Forryan, Garabato, et al., 2014; Polzin et al., 2014a; MacKinnon & Gregg, 2003). Our analysis is consistent with prior studies regarding the broad agreement between finescale parameterized and microstructure estimates of mixing in the open ocean thermocline where the underlying assumptions made in the parameterizations apply (Polzin et al., 1995, 2014a; Whalen et al., 2015a; Waterman, Polzin, Naveira Garabato, Sheen, Forryan, Garabato, et al., 2014). However, based on the wavenumber distribution of global oceanic shear and strain spectra, we provide a rationale behind large biases in finescale parameterized estimates as well as identify their potential global spatial distribution based on data along 15 GO-SHIP lines.

Two clusters associated with high and low biased finescale ϵ estimates when compared to co-located temperature microstructure observations from χ-pods along the P06 section were identified. The clusters are distinct in their spatial distribution along the P06 section. Cluster 1 associated with regions of finescale overestimation is primarily found in the upper ocean between 500 m and 2000 m in depth, while Cluster 7 is linked to regions of finescale underestimation and is found mostly in the deeper ocean below 3000 m with an increased abundance roughly 500 m-1000 m above the bottom bathymetry (Figure 4.3b,c). Both along the P06 section and

averaged globally, the two cluster regions consist of roughly 20% of the total clustered data.

More work is needed to further our understanding of the underlying dynamical processes and the geographical distribution of various flavors of internal wave-wave interactions found in the ocean. Regardless of the cause, this study has shown caution that must be used when applying finescale parameterizations ubiquitously throughout the ocean. We show that there are regions of the ocean where the prevalence of more "red" or more "blue" spectra energy could lead to biases in estimates of mixing derived from finescale parameterization which assumes a GM-like universal form for the underlying spectra. This study could serve as a template to apply unsupervised machine learning approaches to localized process-based hydrographic studies or in engineering innovative features derived from hydrographic observations in an effort to understand the geographical and spatial distribution of the underlying dynamics.

Acknowledgements

We thank the WOCE, CLIVAR, and GO-SHIP programs for collection of the hydrographic and LADCP data used in this study. CLIVAR and GO-SHIP data were collected and made publicly available by the International Global Ship-based Hydrographic Investigations Program and the national programs that contribute to it. Lele was supported by the NASA FINESST program (Grant 80NSSC20K1609). Lele, Purkey, MacKinnon and Nash were supported by NSF (OCE-2023289). Purkey was also supported by NSF (OCE-2023545).

Chapter Four, in full, is a reprint of the material, currently being prepared for submission for the Journal of Geophysical Research: Oceans. R. Lele, S.G. Purkey, J.A. MacKinnon and J.D. Nash. Global Patterns of Bias in Ocean Mixing Parameterization Identified Through Unsupervised Machine Learning *Journal of Geophysical Research: Oceans*. The dissertation author was the primary investigator and author of this material.

Open Research

All data used for this article are publicly available. Hydrographic and LADCP data for hydrographic lines used in this study (Table 1) can be searched by the line "number" through the CCHDO (http://cchdo.ucsd.edu) and University of Hawaii (https://currents.soest.hawaii.edu/go-ship/ladcp/) website. The χ-pod data collected on P06 2017 Leg 1 and 2 are available from CCHDO (https://microstructure.ucsd.edu/#/cruise/320620170703) and (https://microstructure.ucsd.edu/#/cruise/320620170820) respectively.

Figures and Tables

Figure 4.1. Method schematic shows the locations of the Raw CTD and LADCP data along the 15 GO-SHIP lines in the study which are used to create primary features consisting of spectral and non-spectral data (see Section 4.3.2). (b) An example showing dimensionality reduction through NMF decomposition for shear spectra, converting high m dimensional spectra in the input data matrix $\mathbf{X}$ into lower p dimensional spectral features in the form of a latent feature matrix W and a corresponding hidden coefficient matrix H respectively (see Section 4.3.2). (c) Two latent spectral features each (p=2) of shear and strain are aggregated into a feature matrix F (green box, see Section 4.3.2), with additional features (see Section 4.4.3) are used as inputs to the GMM model to generate cluster mappings for all GO-SHIP sections (Table 4.1).

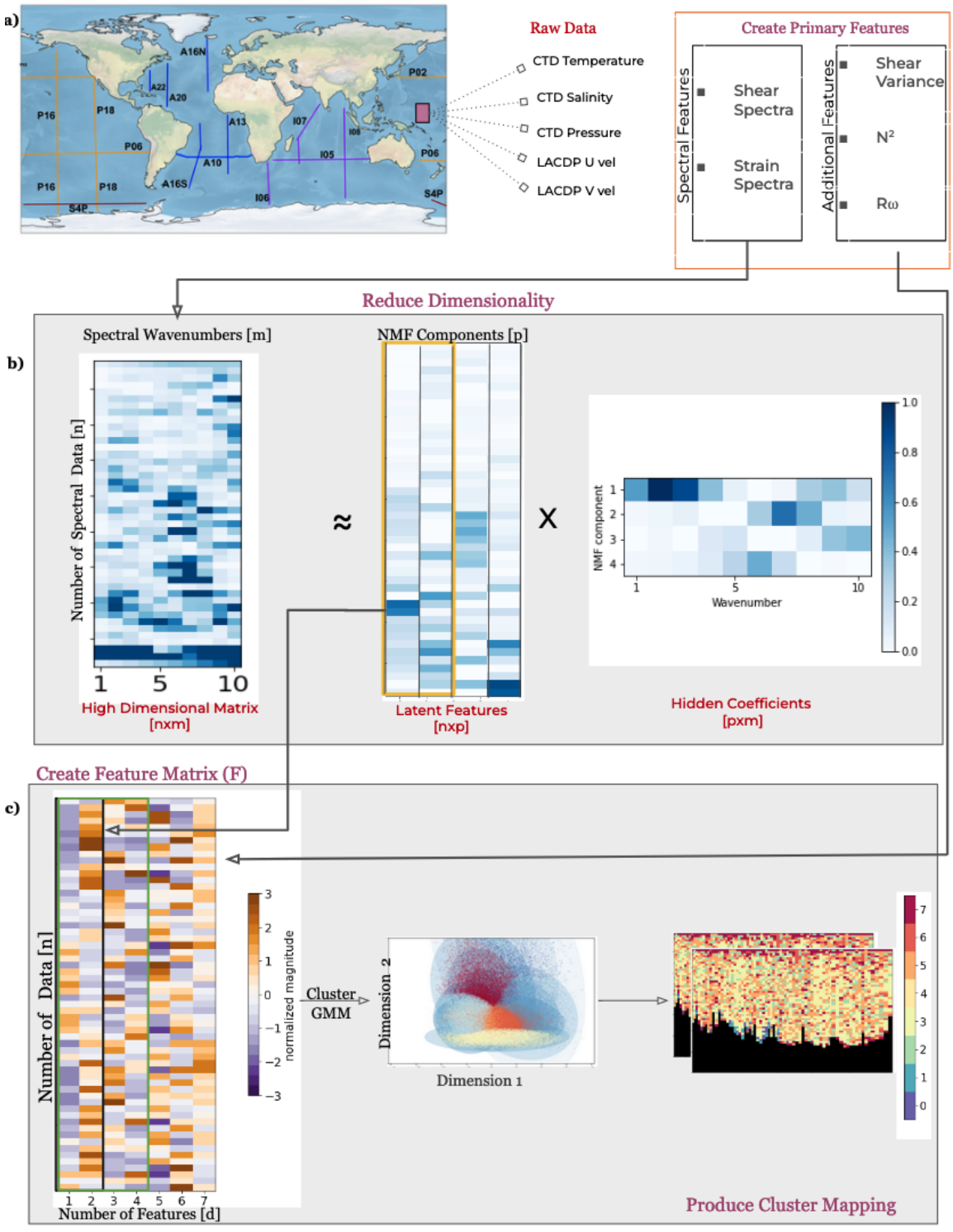
a)
A16N
P02
A22
A20
P16
P18
A13
I07
I08
P06
A10
I05
P06
P16
P18
A16S
I06
S4P
S4P
Raw Data
CTD Temperature
CTD Salinity
CTD Pressure
LACDP U vel
LACDP V vel
Create Primary Features
Spectral Features
Shear Spectra
Strain Spectra
Additional Features
Shear Variance
N²
Rω
Reduce Dimensionality
b)
Spectral Wavenumbers [m]
NMF Components [p]
Number of Spectral Data [n]
1
5
10
High Dimensional Matrix [nxm]
≈
X
NMF component
Wavenumber
Latent Features [nxp]
Hidden Coefficients [pxm]
Create Feature Matrix (F)
c)
Number of Data [n]
normalized magnitude
Cluster GMM
Dimension 2
Dimension 1
Number of Features [d]
Produce Cluster Mapping

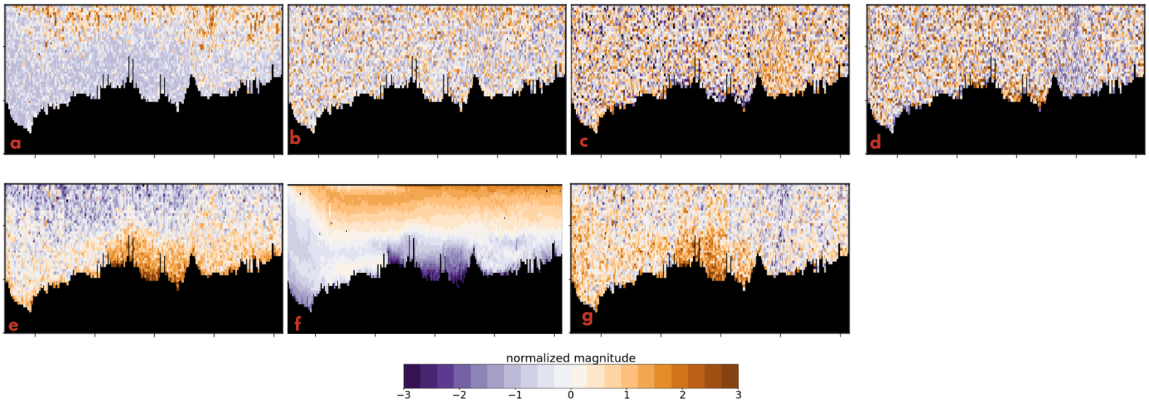

Figure 4.2. Example of geographical feature distribution along the P18 section for 7 different features with normalized magnitudes used for clustering using the GMM model including NMF-1 shear spectra (a), NMF-2 shear spectra (b), NMF-1 strain spectra (c), NMF-2 strain spectra (d), shear variance $\langle V_z^2 \rangle$ (e), buoyancy frequency [N] (f) and R_ω (g).

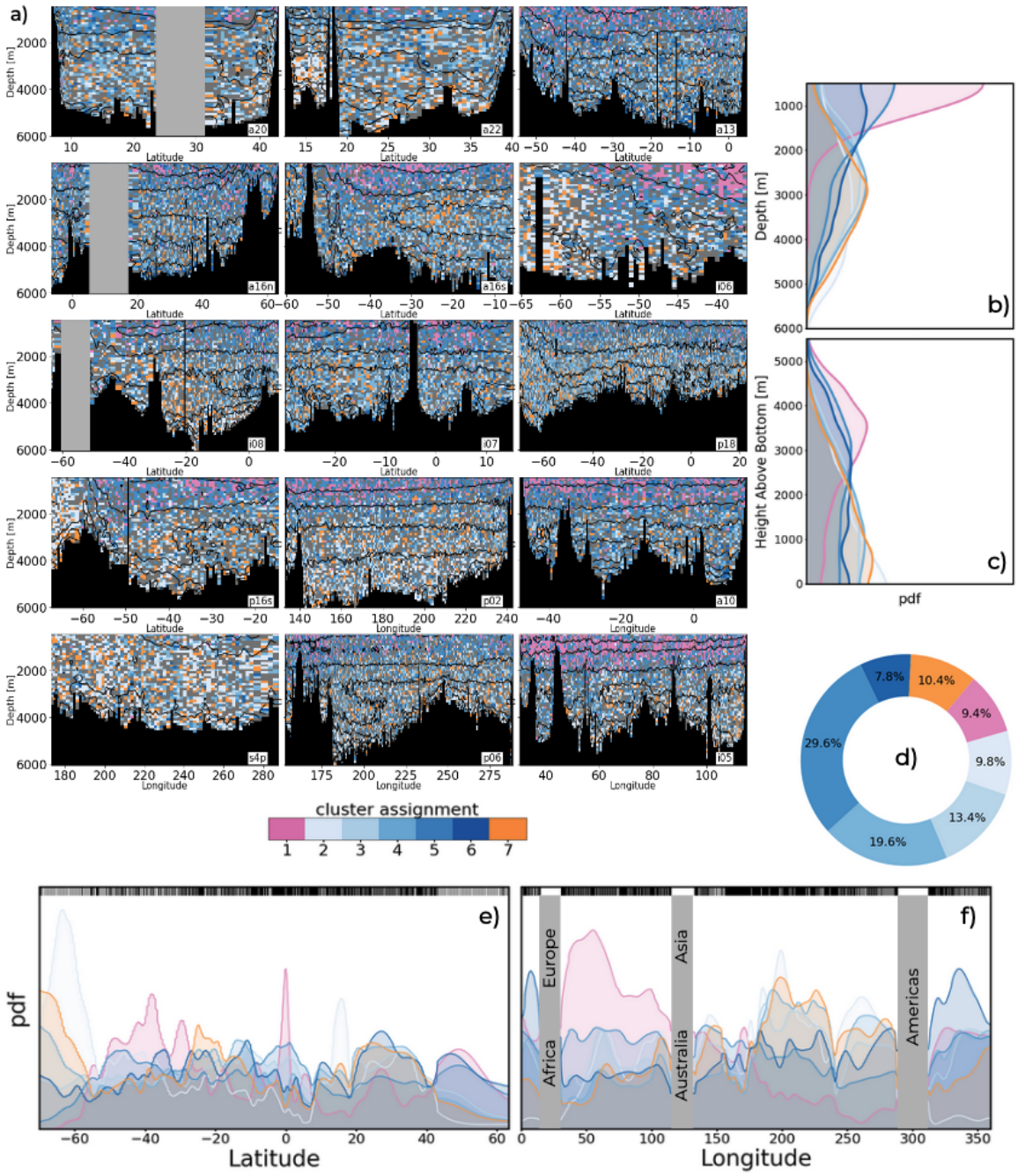

Figure 4.3. a) Resulting clustering along the 15 GO-SHIP lines produced by the GMM model with feature matrix based on the NMF features (Figure 4.2a-d). PDF showing the abundance and variation of individual clusters as a function of depth (b) and height above bottom bathymetry across all 15 GO-SHIP lines (c). Relative percentage distribution of the seven clusters from the GMM model with a posterior probability greater than 70% which are considered for the analysis (d). The zonal (e) and meridional (f) PDF computed from composites of 10 zonal and 5 meridional sections respectively, with the location of CTD stations for the zonal and meridional sections are shown (black vertical lines in e and f).

Figure 4.4. a) Ratio of estimates of turbulent dissipation rate from the finescale parameterization to measurements from CTD-mounted χ-pods taken concurrently along the P06 section expressed as $\log_{10}\left(\frac{\epsilon_{\text{fine}}}{\epsilon_{\chi\text{pod}}}\right)$, b) Cluster assignments from the GMM model along the P06 section (same as Figure 4.3a), c) Mean, 95% confidence intervals and violin plot computed for the ratio $\log_{10}\left(\frac{\epsilon_{\text{fine}}}{\epsilon_{\chi\text{pod}}}\right)$ from Figure 4.4a for seven clustered regions shown in Figure 4.4b, d-e). Mean strain and shear spectra computed as a composite average for the clusters computed using all 15 sections with 99% confidence intervals using computed using a χ^2 distribution (Chatfield et al., 1987) considering only $1/10^{th}$ degrees of freedom for better visibility (color shading). The average GM spectral levels are shown in the dashed black line, with the integration limits to calculate strain and shear variance shown by solid gray vertical lines. Slopes for shear spectra roll-offs between k^{-1} and k^{-4} are shown with high wavenumber asymptote k^{-2} representing inertial sub-range in the GM model, f) Schematic outlining how biases in estimates of turbulent mixing could arise from spectra deviating from the assumed GM-like shape in the finescale parameterization (Equation 4.1) by either overestimating (Cluster 1) or underestimating (Cluster 7) shear $\langle V_z^2 \rangle$ and strain variance $\langle \zeta_z^2 \rangle$ calculated by integrating the respective spectra in the finescale wavenumber band.

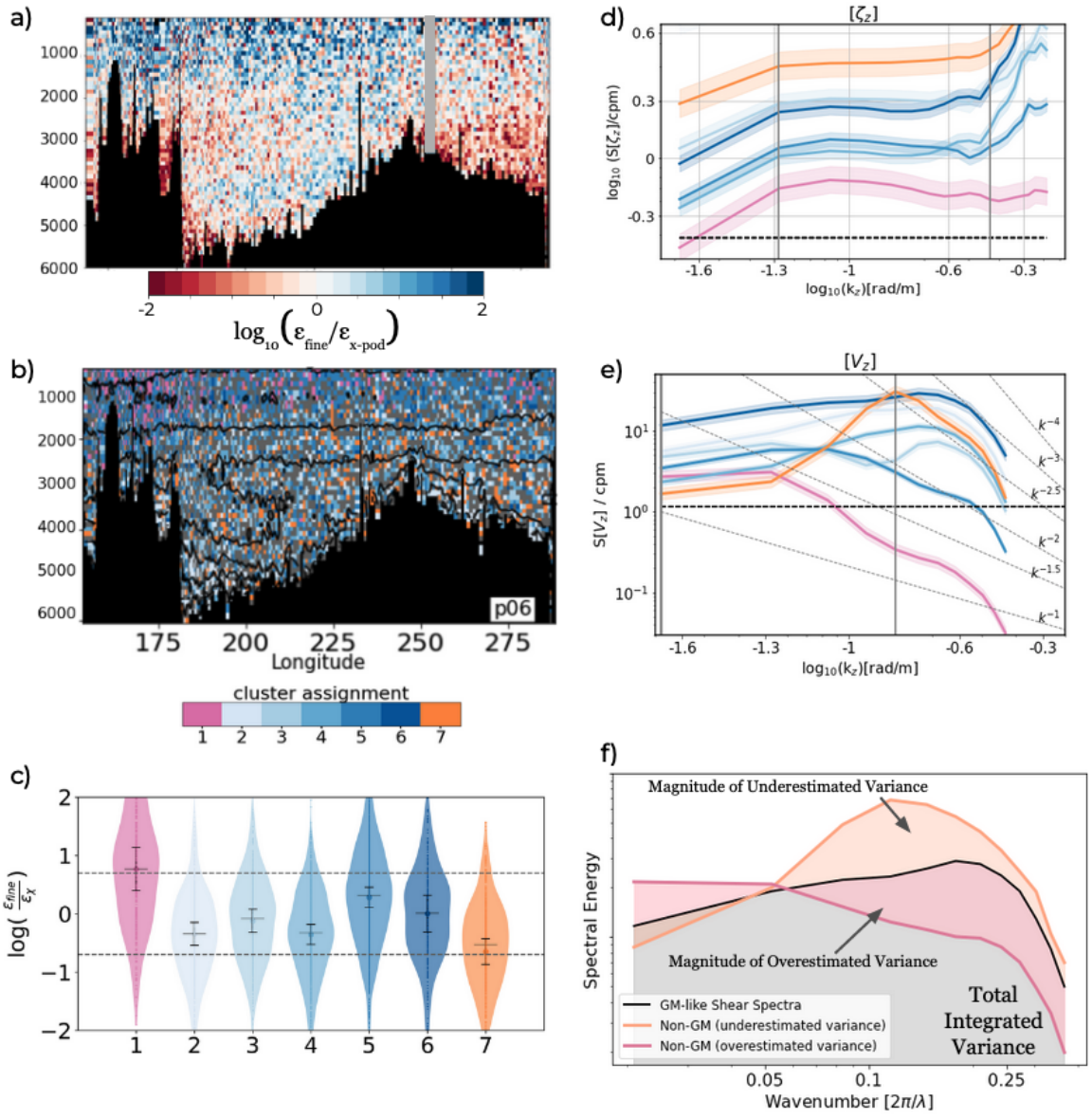
a)
1000
2000
3000
4000
5000
6000
-2
0
2
log10(εfine/εx-pod)
b)
1000
2000
3000
4000
5000
6000
p06
175
200
225
250
275
Longitude
cluster assignment
1 2 3 4 5 6 7
c)
log(Efine/εχ)
2
1
0
−1
−2
1
2
3
4
5
6
7
d)
[ζz]
0.6
0.3
0
-0.3
log10 (S[ζz])/cpm)
-1.6
-1.3
-1
-0.6
-0.3
log10(kz)[rad/m]
e)
[Vz]
10^1
10^0
10^−1
S[Vz] / cpm
k^−4
k^−3
k^−2.5
k^−2
k^−1.5
k^−1
-1.6
-1.3
-1
-0.6
-0.3
log10(kz)[rad/m]
f)
Magnitude of Underestimated Variance
Magnitude of Overestimated Variance
Spectral Energy
GM-like Shear Spectra
Non-GM (underestimated variance)
Non-GM (overestimated variance)
Total Integrated Variance
0.05
0.1
0.25
Wavenumber [2π/λ]

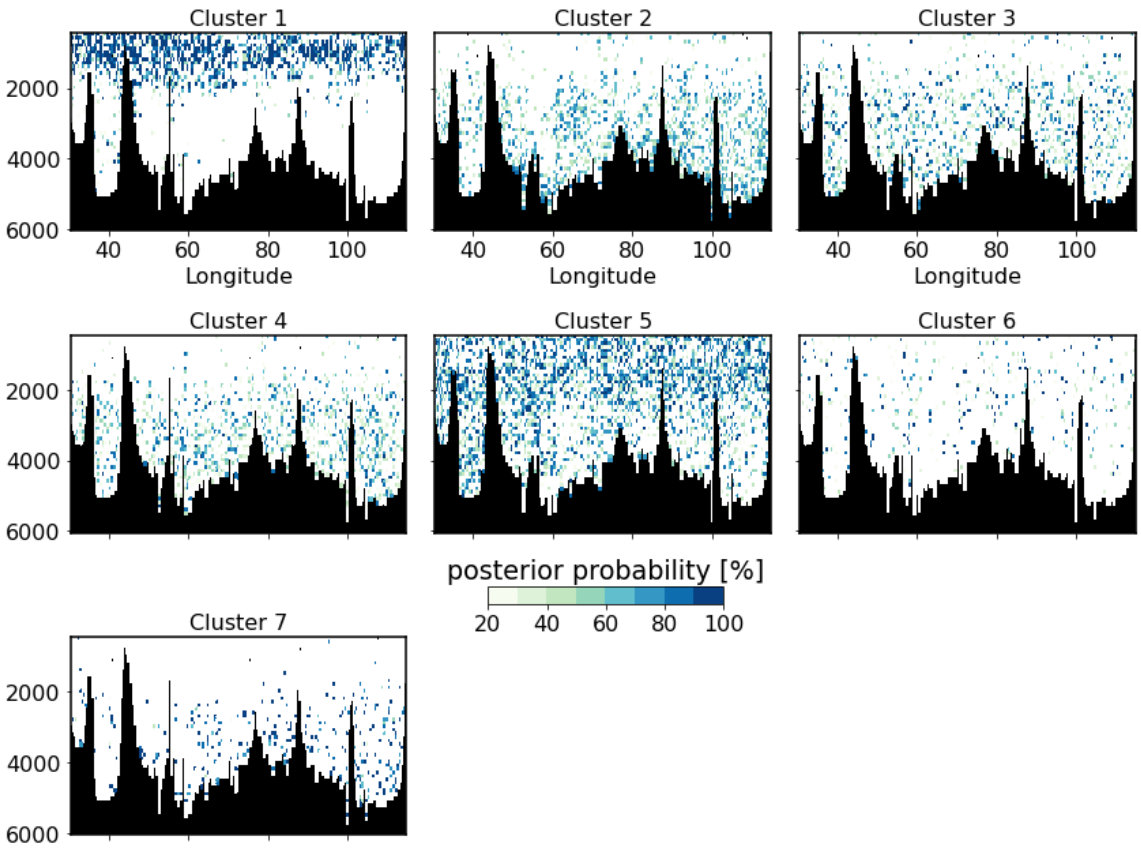

Figure 4.5. Posterior probabilities (%) $p(k|x)$ of data belonging to each of the clusters (1-7) as calculated with Equation 4.6 from the GMM model along the I05 section. Final cluster assignment of a data point belonging to a cluster k as shown in Figure 4.4 is made by computing $k = \text{argmax}_x\, p(k|x)$ as described in Section 4.3.3 .

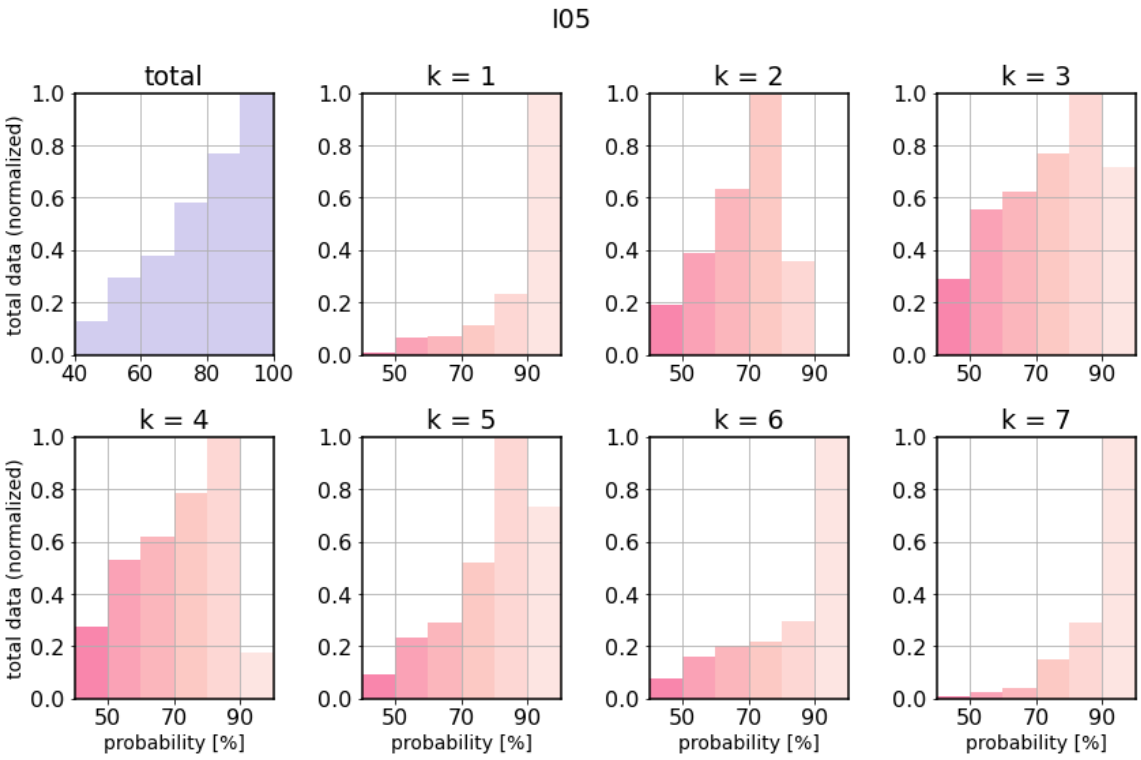

Figure 4.6. Histogram of the total percent posterior probabilities along the I05 section summed across all the clusters $\sum_{k=1}^{K} p(k|x)$ in 10% bins between 40% to 100% (top left). Additionally, histogram of the percent posterior probabilities in each individual cluster k=1-7 corresponding to Figure 4.5 are displayed as well. Data displayed in each bin are normalized by number of datapoints in the 10% bin with the most data.

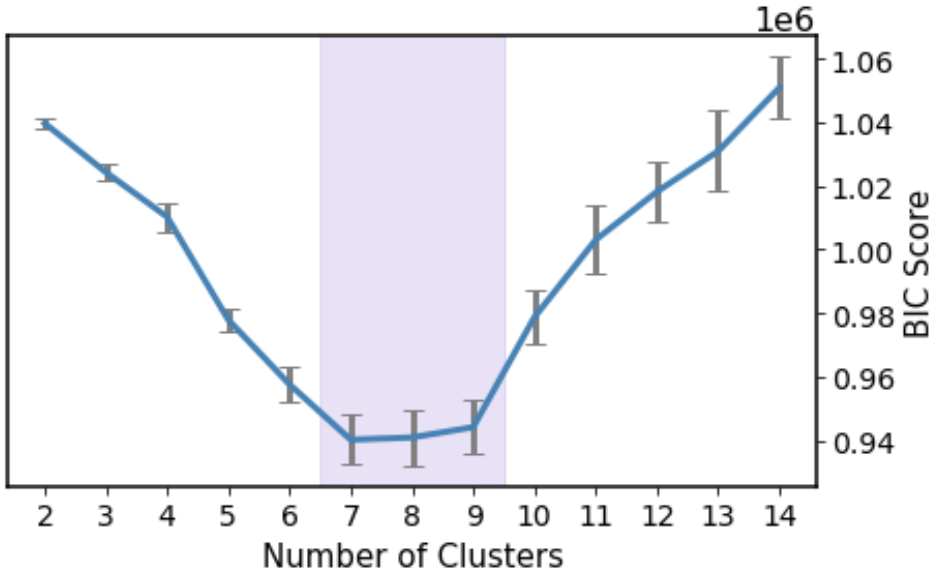

Figure 4.7. The BIC scores versus the specified number of clusters, with the means (solid blue line) and standard deviations (error bars) calculated from 50 random subsets of the data is also shown with the range of the smallest BIC values (between k=7 and k=9) is indicated (purple shading)

Table 4.1. Total number of full-depth profiles for each of the 15 GO-SHIP lines in the study along with the percentage distribution of each cluster from the GMM model output along a given line corresponding to results described in the main text and Figure 4.3.

Line	Profiles	Cluster 1	Cluster 2	Cluster 3	Cluster 4	Cluster 5	Cluster 6	Cluster 7
a20	74	2.9	9.4	17.3	28.8	22.8	6.2	12.6
a22	90	1.9	15.2	15.7	28.5	17.1	6.9	14.8
a13	128	10.2	1.5	13.1	19.3	36.5	12.9	6.4
a16n	119	8.5	1.6	12.9	18.5	35.5	15.3	7.8
a16s	111	9.5	2.2	15.0	24.7	27.4	10.6	10.6
i06	56	13.2	22.7	11.4	7.6	33.0	2.5	9.5
i08	114	5.7	12.8	13.7	16.0	34.6	5.2	12.0
i07	110	8.6	2.4	15.4	23.5	31.4	9.0	9.7
p18	209	2.6	2.9	17.5	34.9	19.2	10.5	12.4
p16s	86	8.6	20.5	11.6	14.0	29.8	2.8	12.6
p02	159	9.8	17.6	11.7	14.0	31.1	4.9	10.9
a10	116	16.5	1.6	11.6	17.0	35.7	10.9	6.7
s4p	72	0.5	36.1	11.9	19.6	9.1	3.6	19.2
p06	244	7.9	10.8	12.9	18.5	31.8	7.1	11.0
i05	187	25.3	10.8	9.7	8.2	35.7	3.0	6.3
TOTAL	1875	9.4	9.8	13.4	19.6	29.6	7.8	10.4

Supporting Figures

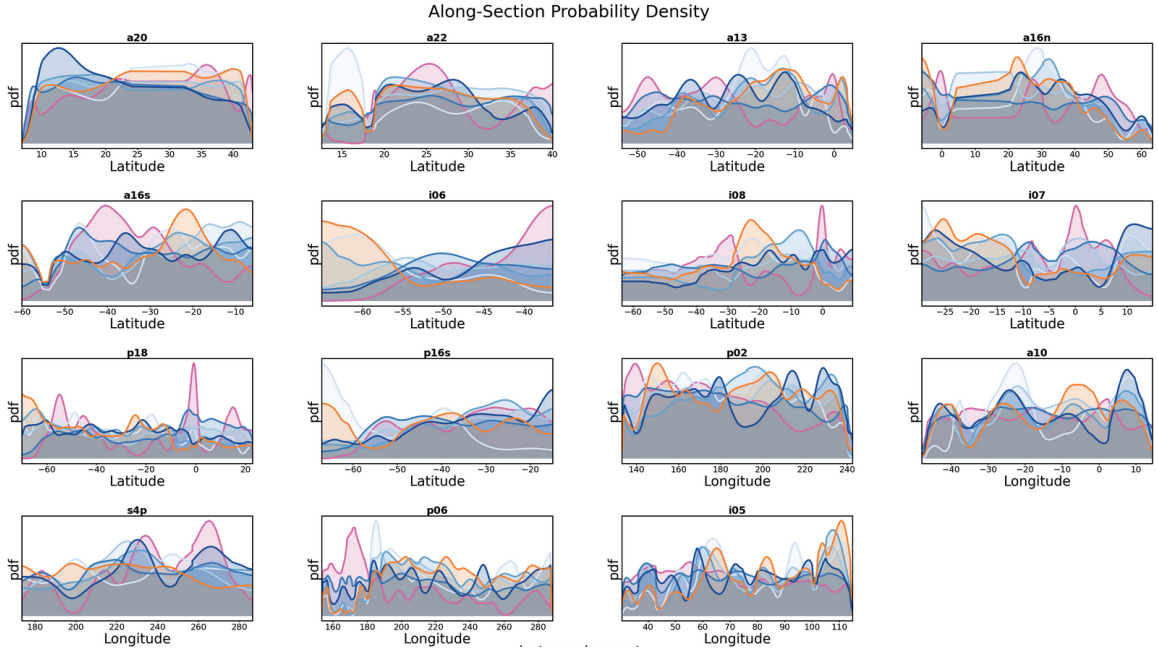

Figure 4.8. PDF showing the variation of individual clusters along each of the 15 GO-SHIP sections (See Figure **??** for locations).

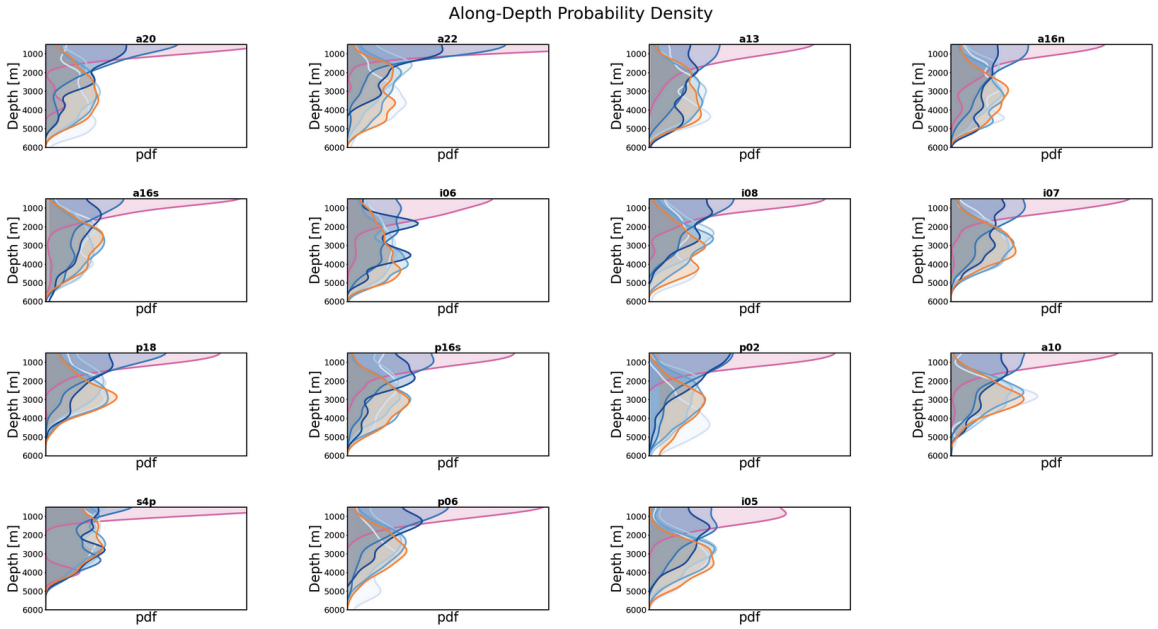

Figure 4.9. PDF showing the variation of individual clusters as a function of depth along each of the 15 GO-SHIP sections(See Figure **??** for locations).

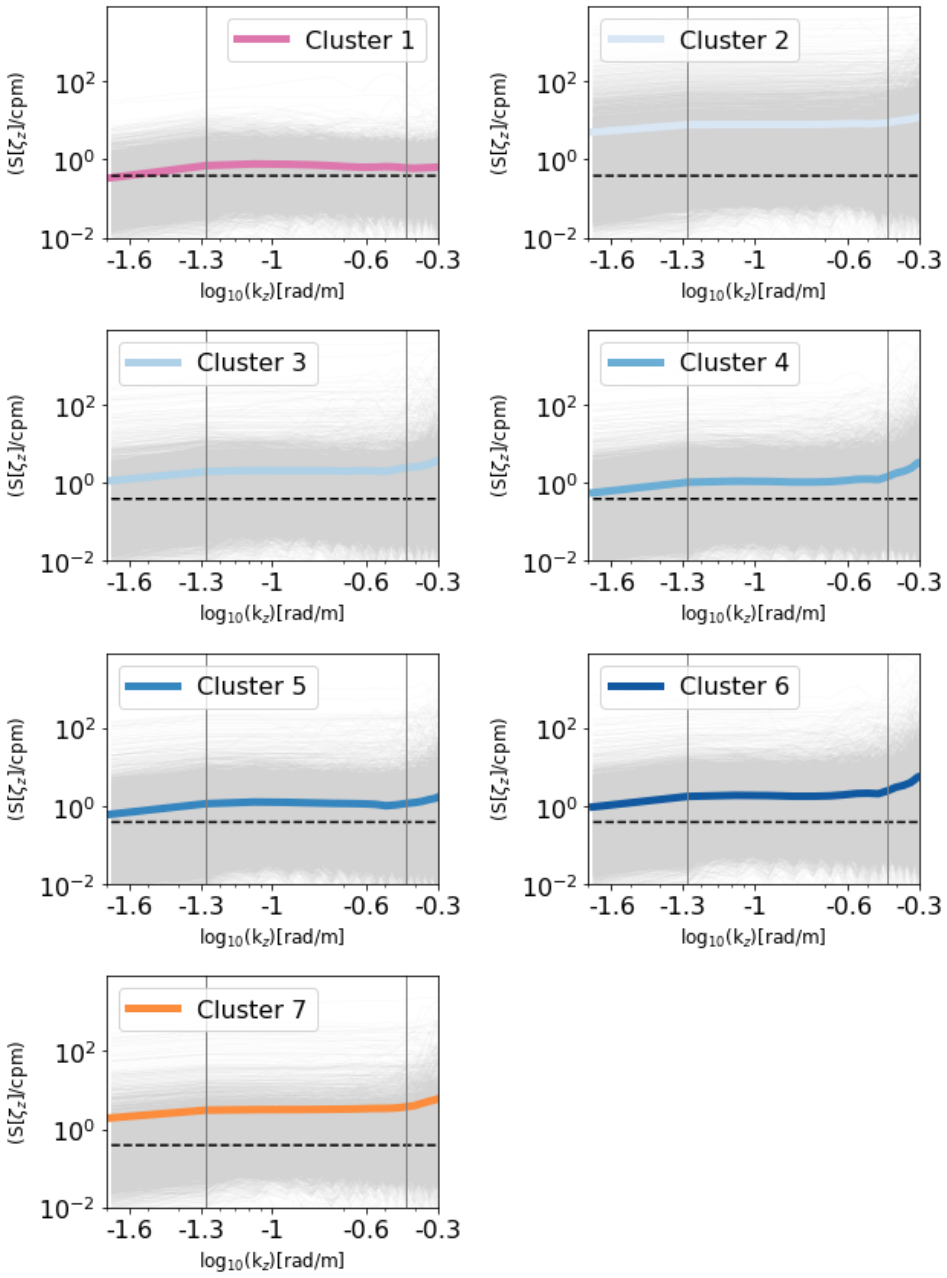

Figure 4.10. Individual strain spectra (dashed black) assigned to a given cluster with a posterior probability greater than 70% (Figure 4.3a) with the mean strain spectra (color) associated with each cluster (note: mean spectra are the same as Figure 4.4d)

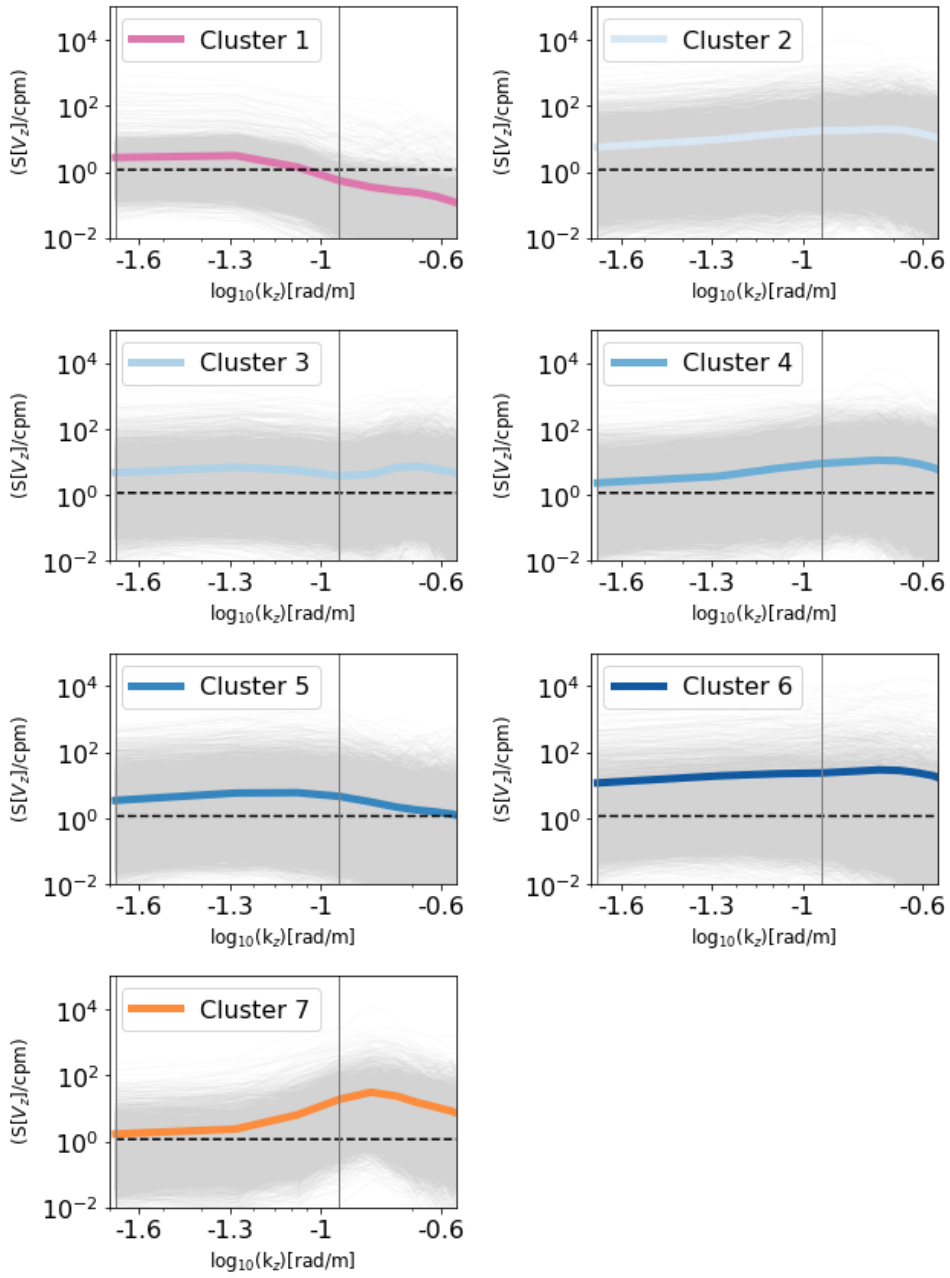

Figure 4.11. Individual shear spectra (dashed black) assigned to a given cluster with a posterior probability greater than 70% (Figure **??**a) with the mean shear spectra (color) associated with each cluster (again, mean spectra are the same as Figure 4.4e)

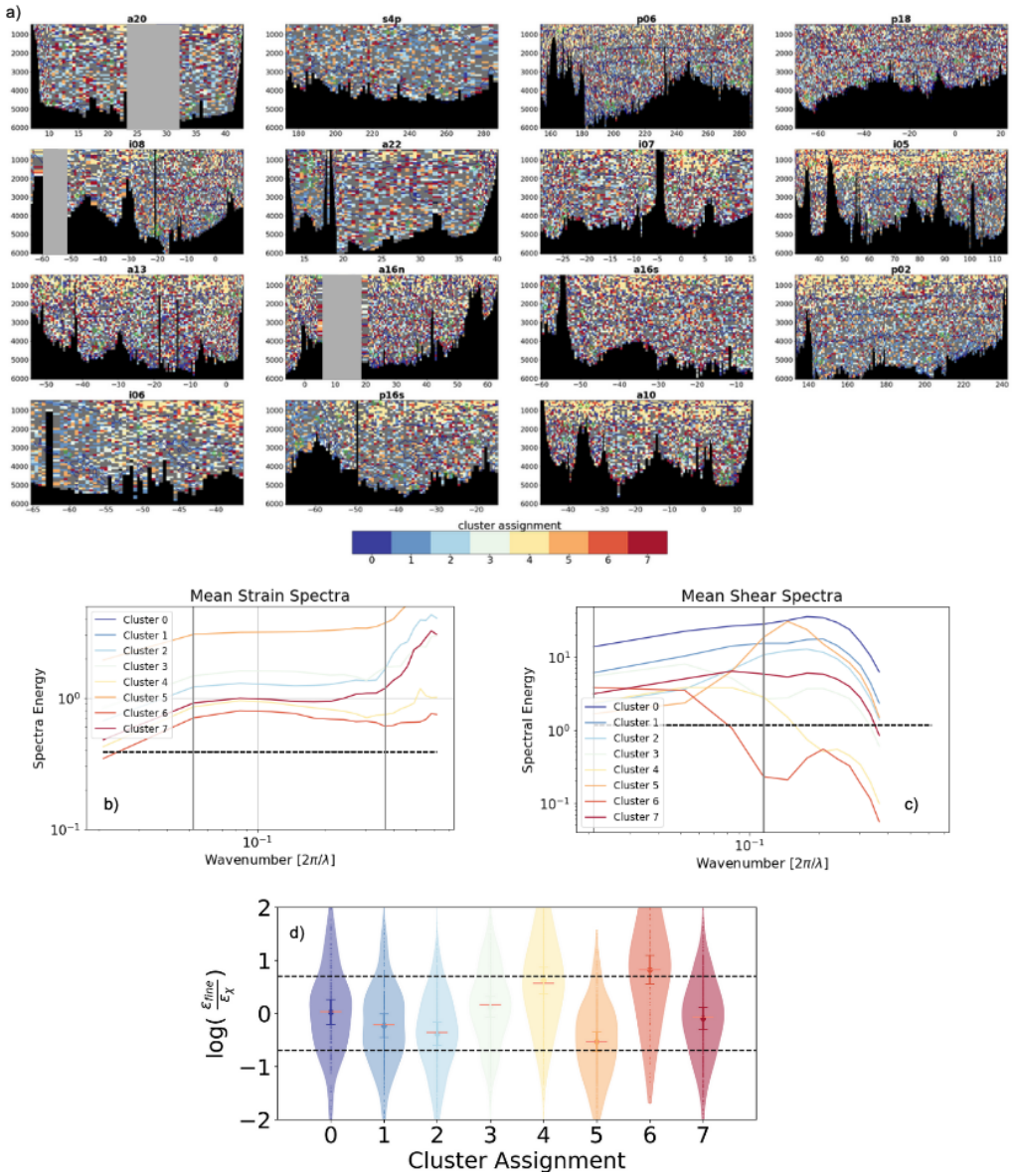

Figure 4.12. a) Clustering assignments along the 15 GO-SHIP lines produced by the GMM model using K=8 as the optimal number of clusters with feature matrix based on the NMF features (Figure 4.2a-d) as discussed in Text S1-S3. b-c) Mean strain and shear spectra computed as a composite average for the clusters computed using all 15 sections. The average GM spectral levels are shown in the dashed black line, with the integration limits to calculate strain and shear variance shown by solid gray vertical lines. Mean and 95% confidence intervals are shown in the violin plot computed for the ratio of $\log_{10}\left(\frac{\epsilon_{\text{fine}}}{\epsilon_{\chi\text{pod}}}\right)$ along P06 (following Figure 4.4c) for the eight clustered regions shown in panel (a, P06)

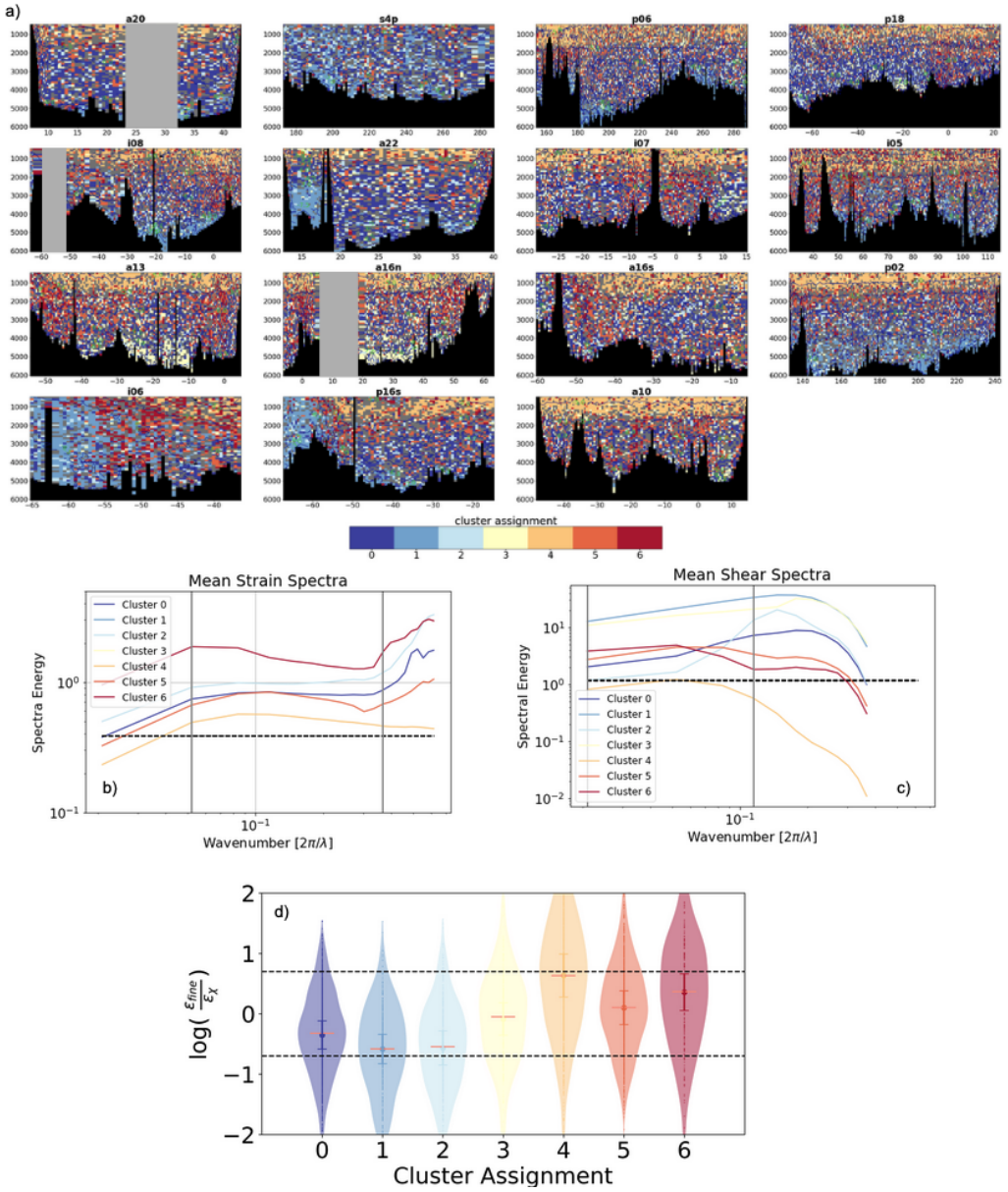

Figure 4.13. a) Resulting clustering along the 15 GO-SHIP lines produced by the GMM model using K=7 as the optimal number of clusters but with feature matrix based on the NMF spectral features and three additional features (Figure 4.2a-g) as discussed in Text S4. b-c) Mean strain and shear spectra computed as a composite average for the clusters computed using all 15 sections. The average GM spectral levels are shown in the dashed black line, with the integration limits to calculate strain and shear variance shown by solid gray vertical lines. Mean and 95% confidence intervals computed for the ratio $\log_{10}\left(\frac{\epsilon_{\text{fine}}}{\epsilon_{\chi\text{pod}}}\right)$ from Figure 4.4a for seven clustered regions shown in panel (a)

Chapter 5

A Full-Depth Sea Level Rise Budget in the Southwest Pacific Basin using Deep Argo

Abstract

The first Deep Argo Pilot array, located in the Southwest Pacific Basin, has collected nearly 9 years of data offering, for the first time, the ability to characterize deep ocean warming and steric expansion on spatial and temporal scales never before explored. Here, this novel data set is used (1) to quantify regional conservative temperature, salinity and density anomalies with respect to a long-term ship-based oceanographic climatology, (2) to calculate warming and steric trends over the 9 year period using the Deep Argo array only, and (3) close the 9 year local sea level budget using the observed top to bottom steric expansion calculated from the Deep Argo floats. Using the 4954 full-depth profiles collected between July 2014 and May 2023 by the 55 Deep Argo floats deployed to date, we find consistent warm anomalies below 2000 m ranging between 11±2 to 34 ±2 m^{o}C at the 95% confidence level, with temperature anomalies most pronounced (>20 m^{o}C) between 3500 and 5000 m. The temperature trend over the 9 year period shows a cooling between 2000- 4000 m and a significant warming trend below 4000 m with a maximum rate of 4±0.3 m m^{o}C yr^{-1} near 5000 m. This warming resulted in a integrated Steric Sea Level expansion between the bottom and 2000 m of 7.9 ± 1 mm compared to the climatological era and a trend of 1.3 ± 1.6 mm dec^{-1} over the 9 year Deep Argo period, a significant contribution to the local sea level budget. Finally, we examine the ability to close a full Sea Level Budget with the added contribution of the deep steric changes, to further demonstrate the value of a truly full-depth Argo array.

5.1 Introduction

The Earth's energy is currently out of balance, with the climate system accumulating 0.5-1 W m^{-2} over the 21st century (Hansen et al., 2011; Von Schuckmann et al., 2016; von Schuckmann et al., 2022; Trenberth et al., 2014; Llovel et al., 2014). One of the most direct and well-documented consequences of this energy imbalance is the rise of global mean surface temperatures and warming in the lower atmosphere (Hansen et al., 2011; Meyer et al, 2014; Steiner et al., 2020). Although these global mean surface temperatures and atmospheric warming effects are most perceptible, they account for a small fraction of the Earth's energy budget. The oceans accumulate roughly 85% - 90% of the excess warming and therefore play a dominant role in sequestering the excess heat and mediating the worst effects of rapid atmospheric warming (Domingues et al., 2008; Levitus et al., 2000, 2005, 2012; Meyer et al, 2014; Cheng et al., 2017; von Schuckmann et al., 2022). One consequence of the increase in ocean heat content is the rise in global mean sea level owing to the thermal expansion, accounting for roughly half the observed sea level rise over the last century (Von Schuckmann et al., 2016). Tide gauge records over the 20th century show an increase in the global mean sea level of roughly 2 mm yr^{-1} (Church & White, 2006, 2011; Dangendorf et al., 2017), while satellite altimetric estimates put this figure around 3.3 ± 0.4 mm yr^{-1} and show an acceleration during the 20th and 21st centuries (Watson et al., 2015; Dieng et al., 2015; Chambers et al., 2017; Nerem et al., 2018; Ablain et al., 2015; Cazenave et al., 2018).

Over the last 50 years, the increase in ocean heat content (OHC) has been most pronounced in the upper ocean, with the top 2000 m of the ocean absorbing about 90% of the total OHC, with some evidence of recent acceleration in abyssal warming rates over the last decade (Von Schuckmann et al., 2016; von Schuckmann et al., 2022). Deep and abyssal ocean warming or cooling could indicate a shift in the large scale overturning circulation. Observations have provided some evidence of a decline in Antarctic Bottom Water formation rates around Antarctica associated with deep ocean warming throughout the Southern Ocean, as well as decadal variability

in rate and properties of North Atlantic Deep Water (Purkey & Johnson, 2010, 2012b, 2013; Smeed et al., 2014). Moreover, modeling studies have pointed to a long-term slowdown in the overturning circulation in both hemispheres with potentially calamitous feedbacks into the global climate system (Li et al., 2023; Gunn et al., 2023; Ditlevsen & Ditlevsen, 2023).

Although satellite altimetry can monitor the total rate of sea level rise, it is necessary to understand the components and mechanisms leading to global mean sea level rise and its variability to better predict future sea level rise, as well as understand and quantify any errors in the satellite observations (Llovel et al., 2019; Chambers et al., 2017; Cazenave et al., 2018). Crucially, density-driven volumetric variation (steric variation) from changes in temperature and salinity changes (thermosteric and halosteric respectively) in the ocean is a significant contributor to sea level rise and the global sea level budget (Bindoff et al., 2007; Levitus et al., 2012; Cazenave et al., 2018; Llovel et al., 2019). *In-situ* hydrographic measurements sampling the ocean sub-surface are vital to measuring the steric component of sea level rise. For most of the 20th century, sampling of oceanographic properties was sporadic, with low spatial and temporal coverage. In the early 2000s, Argo (also referred to as core-Argo) revolutionized our ability to monitor steric variability in the upper 2000 m, maintaining a fleet of roughly 4000 floats worldwide, allowing for accurate monitoring of temperature and salinity changes on high temporal (1 month) and spatial (1 deg x 1 deg) resolution around the globe (Roemmich et al., 2019).

Despite these advances in global ocean observational capabilities in the last few decades, the deep ocean below 2000 m remains vastly undersampled in comparison. Most ocean observations including measurements from the core-Argo fleet are limited to the top 2000 m (Abraham et al., 2013), limiting our understanding of steric changes occurring in the deep ocean. Deep steric estimates rely on decadal observational programs such as the World Ocean Circulation Experiment and the Global Ocean Ship-based Hydrographic Investigations Program (GO-SHIP) (Talley et al., 2016; Gould et al., 2004; Roemmich et al., 2012; Riser et al., 2016). These hydrographic measurements have shown an increase in deep ocean temperatures in most

deep ocean basins below 4000 m, contributing to sea level rise estimates at a rate of approximately 1mm dec $^{-1}$ (Purkey & Johnson, 2010; Purkey et al., 2014; Desbruyères et al., 2016; Purkey et al., 2019), roughly 10-15% of total steric sea level rise (Von Schuckmann et al., 2016; von Schuckmann et al., 2022; Llovel et al., 2019). Efforts to infer deep steric changes as a residual in the sea level budget (sea level anomalies from satellite altimetry minus ocean mass changes from GRACE satellite data and the steric contribution between the surface and 2000 m from core-Argo float data) are fraught with errors, bias and uncertainties related to various instrumentation noise and mapping errors in data products and can lead to contradictory estimates of the deep steric signal (Dieng et al., 2015; Llovel et al., 2014).

The implementation of a 1250-float Deep Argo Array aims to alleviate obstacles of data-gathering in the deep and abyssal ocean (G. C. Johnson et al., 2015; Roemmich et al., 2019). The floats capable of measuring down to 4000 m or 6000 m depending on the model specifications, can potentially reduce deep steric uncertainty to a fifth of current estimates from using only hydrographic data. Pilot arrays of Deep Argo floats have been deployed since early 2014 in deep basins around the globe. Initial data at bi-monthly resolution from pilot Deep Argo arrays deployed in the Southwest Pacific, Argentine and Brazil basins have shown continued warming in the deepest parts of the basin below 4000 m and have provided warming rates in the Antarctic Bottom Water layers with a high degree of accuracy(G. C. Johnson et al., 2019, 2020; G. C. Johnson, 2022).

In this study, we analyze temperature and salinity data below 2000 m from 4954 full-depth profiles taken by 55 Deep Argo floats in the Southwest Pacific Basin between July 2014 and May 2023 to evaluate the continued deep warming trends in the basin. Further, we extend this analysis to estimate the total deep steric variability and trend (thermosteric + halosteric), to better assess the closure of the local sea level budget. Data and methodology used to analyze data from a core Argo climatology, Deep Argo float data, and satellite-gridded products of sea surface height and ocean mass are described in Section 5.2. We present the main results in Section 5.3, followed by a discussion surrounding the results in Section 5.4. These results highlight the consequences

of the deep ocean warming and steric sea level rise and demonstrates the value of making high quality, high resolution measurements of the deep ocean.

5.2 Data and Methods

We use the WOCE hydrographic climatology (Gouretski & Koltermann, 2004) to determine long-term average temperature and salinity in the basin. The WOCE climatology represents the averaged properties in the basin over the 1980-2004 time period, using data from hydrographic observations objectively mapped onto a $1^o \times 1^o$ spatial grid. The deep ocean data considered here below 2000 m consist of 15 depth levels from 2000 m to a maximum of 5750 m, with a depth-spacing of 250 m. Practical salinity and temperatures in depth for each grid point $1^o \times 1^o$ are converted to absolute salinity and conservative temperature Θ using TEOS-10 equation of state (Feistel, 2012; McDougall, 2011).

In the Southwest Pacific Basin between latitudes 10^oS and 50^oS and longitudes 170E^o and 130^oW, we consider a total of 55 floats in the region between July 2014 and May 2023 (Figure 5.1, yellow lines). Further, in the spatial regions defined for the Southwest Pacific basin, we only consider floats with at least one profile deeper than 4000 m in the study. Data from a total of full-depth downcast 4954 profiles from the 55 floats are used for the analysis. Of the profiles, 4948 profiles reach 3000 m, 4843 reach 4000 m, 4320 reach down to 5000 m, and 171 profile down to 5750 m and lower (Figure 5.7, purple). The SeaBird Scientific SBE-61 CTD (Conductivity-Temperature-Depth) sensors with accuracy of 0.002psu, 1m^o C and 2dbar, respectively. Only good quality flag data are considered. The salinity, temperature and pressure profile data are used to calculate absolute salinity, conservative temperature Θ and depth. The Deep Argo data is linearly interpolate in latitude, longitude and depth coordinates onto the WOCE grid. In depth, this results in the float data being mapped onto 15 depth levels with 250 m vertical spacing.

The temperature anomaly and trend are calculated using all floats in the basin. First,

the Θ anomalies are calculated as the difference between conservative temperature estimates along the float location and the WOCE climatology. Second, a linear trend in Θ over the 9 year float data period is calculated using a least squares fitting procedure following Wunsch (1996) at each vertical level (e.g. Figure 5.5, 5000 m). Degrees of freedom for computing confidence limits on Θ anomalies and trends at each vertical level are calculated by assuming statistical independence between profile data from each float. However, a temporal decorrelation time scale of 60 days is considered between profiles from the same float such that, if there a total N_{60} profiles within a 60-day period, each profile contributes $1/N_{60}$ degrees of freedom within that time frame (G. C. Johnson et al., 2015, 2019).

Following this procedure, the effective degrees of freedom generally decrease with an increase in depth and vary between 850-750 between 2000 m and 5000 m, a factor of ~6 reduction, whereas at 5500 m the effective degrees of freedom, reduce by a factor of ~4 to around 200 (Figure 5.7. We computed 5–95% confidence intervals (two-tailed 90%) using the standard deviations (σ) and the effective degrees of freedom estimated above assuming Student's t-distribution and use the same significance tests to assess confidence intervals throughout the rest of the study. The reduction in degrees of freedom has negligible (<1%) effect on the estimated confidence interval as the Student t-distribution score asymptotes to ~2 for such large values of degrees of freedom.

Temperature and salinity measurements made by the Deep Argo floats also allow us to calculate density anomalies at a given vertical level compared to the WOCE climatology allowing us to estimate the steric changes in the water column for a given depth range. Anomalies of density (ρ') are calculated in the same manner as Θ anomalies described above. The density anomaly ρ' computed as a function of ocean salinity, temperature and pressure variation is derived from the Deep Argo and WOCE Climatology profiles at a given location. Following Gill & Niller (1973) and Tomczak & Godfrey (1994), the steric sea-level anomaly η_s can be

computed as:

$$\eta_s = -\frac{1}{\rho_0}\int_{z_2}^{z_1} \rho' \tag{5.1}$$

where ρ_0 is a reference density and ρ' is the local density anomaly. The expression is vertically integrated from the maximum local depth z_2 to the top interface (z_1, here 2000 m). We use the Thermodynamic Equation of Seawater (TEOS-10, McDougall (2011) equation of state to calculate the steric sea level anomaly.

After the steric anomalies with respect to the climatology are calculated at each vertical level (Figure 5.3b), the anomalies are integrated between the bottom and the top (2000 m) to calculate the total steric contribution at each location (Figure 5.3b), hereafter referred to as "deep steric" anomalies. Since the bottom reference for integrating steric anomalies z_2 varies with changes in the bottom depth as the float traverses the basin, the total steric anomaly calculated from Equation 5.1 represents the deep steric contribution below 2000 m at each float location. Similarly, a least squares fitting is used to find the trend in the integrated deep steric between the bottom and 2000 m (Figure 5.8). The significance estimate on the trend is calculated similarly as for the trend inΘ using a Student t-distribution and effective degrees of freedom using a 60-day decorrelation timescale.

5.2.1 A Local Sea Level Budget using Deep Argo

To evaluate the applicability of using the Deep Argo data to monitor in-situ deep steric changes on local to regional scales, we select a single $5^o \times 5^o$ box in the Southwest Pacific Basin with over 5 years of Deep Argo coverage to examine the local sea level budget. The Mean Sea Level change (MSL) expressed as a function of time t can be written as :

$$MSL(t) = MSL_{\text{mass}}(t) + MSL_{\text{steric}_{(0-2000)}}(t) + MSL_{\text{steric}_{(2000-btm)}}(t) \tag{5.2}$$

where $MSL_{\text{steric}_{(0-2000)}}(t)$ represents the steric contribution of the ocean due to density-driven volumetric changes in the upper 2000 m in the mean sea level, whereas $MSL_{\text{mass}}(t)$ reflects the

mass anomaly in the region either due to the movement of water into and out of the region or addition to the ocean mass of the region. $MSL_{\text{steric}_{(2000-btm)}}(t)$ is the steric contribution below 2000 m, the "deep steric" signal.

The left-hand side of Equation 5.2 can be retrieved through satellite altimetry. We use monthly gridded sea level anomaly observations from AVISO
(AVISO website https://www.aviso.altimetry.fr/en/data/products/) to estimate $MSL(t)$ in the basin (Figure 5.9, top). The gridded sea surface height product consists of sea surface anomalies computed with respect to a 20-year reference period (1993-2012) and has an accuracy of ~1 cm for measuring Global MSL changes once instrumental and geophysical corrections have been applied to the dataset (Stammer & Cazenave, 2017; Cazenave et al., 2018).

The time series of variation of ocean mass, $MSL_{\text{mass}}(t)$, is estimated using NASA's GRACE data (Tapley et al., 2004) derived from the Jet Propulsion Laboratory (JPL) RL06M spherical mass concentration block "mascon" solutions (Watkins et al., 2015). The mascon solutions have shown improvements over spherical harmonic solutions established in the first decade of GRACE observations.The JPL RL06M uses a-priori constraints in space and time to estimate global, monthly gravity fields in terms of equal-area $3^o \times 3^o$ spherical cap mass concentration functions to minimize the effect of measurement errors resulting improved signal-to-noise (S/N) ratios (Watkins et al., 2015; Tapley et al., 2019). We use the GRACE mascon solution in the Southwest Pacific Basin to estimate $MSL_{\text{mass}}(t)$ in Equation 5.2 (Figure 5.9, bottom). The GRACE data have the largest footprint amongst the gridded data products used here. Although the mapped product available is of a higher resolution of $0.5^o \times 0.5^o$, the $3^o \times 3^o$ mascon approximately matches the accuracy and native resolution of the GRACE satellites (Wiese et al., 2016).

Lastly, the upper ocean steric height, $MSL_{\text{steric}_{(0-2000)}}(t)$, is estimated using the Argo Climatology (Roemmich & Gilson, 2009) which consists of temperature and salinity data from thousands of core-Argo float profiles, objectively mapped onto a $0.5^o \times 0.5^o$ grid worldwide. We use temperature and salinity data from the climatology in the basin to estimate the upper ocean

steric contribution above 2000 m using Equation 5.1 (Figure 5.9, middle).

We test closure of the sea level budget by focusing on a small $5^o \times 5^o$region within the Southwest Pacific Basin between 30^oS and 35^o and 170^oW and 165^oW (Figure 5.9, grey box). We use data from 3 Deep Argo Floats (WMO ID: 5902444, 5902528, 5905760) to calculate the deep steric anomalies in the $5^o \times 5^o$ region between the earliest float deployment in Spring 2016 and January 2023. The deep steric anomalies computed using the floats $MSL_{\text{steric}_{(2000-btm)}}(t)$ can be combined with the upper ocean steric anomalies from Argo climatology $MSL_{\text{steric}_{(0-2000)}}(t)$, to compute the full-depth steric anomaly time series between 2016 and 2023 (Figure 5.10, purple past 2016).

5.3 Results

Antarctic Bottom Water (AABW) fills the majority of the deep ocean volume within the Southwest Pacific Basin (G. C. Johnson, 2008; Talley et al., 2007). The cold, dense, nutrient rich AABW layer can often reach from the bottom up to 5000, in the abyssal plains and regions near the Tonga-Kermadec Trench and Deep Western Boundary Current. As the AABW production rates decline and the water mass undergoes contraction in various basins (Purkey & Johnson, 2012b), this deepest layer in the basin is increasingly a mix of warmer Circumpolar Deep Water from the Antarctic Circumpolar Current region. Warmer, saltier waters associated with North Atlantic Deep Water (NADW) sits above this layer roughly up to a depth of 3500 m (Talley et al., 2007). Between NADW and 2000 m is a mix of older unventilated Pacific Deep Water and ventilated intermediate and mode waters. Studies using hydrographic observations have estimated that the warming trend in the deep and abyssal waters in the basin is transforming the water mass properties in the basin (Purkey & Johnson, 2010, 2012b), with a rate of isopycnal heave between 10-25 m yr^{-1} in the deepest portions of the basin (Lele et al., 2021).

5.3.1 Θ and Steric Anomaly and Trends in the Basin

Using data from Deep Argo from 4954 profiles from 55 floats between July 2014 and May 2023 we calculate changes in Θ compared to a long-term WOCE hydrographic climatology (Gouretski & Koltermann, 2004) (1980-2004, mean 1995). We find statistically significant warming in the deepest portions of the basin, consistent with findings from previous studies which use both hydrographic and float data (Purkey & Johnson, 2010; Kouketsu, Kawano, et al., 2011; Lele et al., 2021). The Θ anomaly reveals that the entire depth range between 2000 m and bottom is warmer than the climatological era of roughly two to three decades prior. The warming is most pronounced between 3800 m and 4200 m with Θ anomalies in excess of 30±2.8 m ^{o}C. The warming in the deepest layer at 5750 m is roughly between 12±4 m ^{o}C (Figure 5.4). The uncertainties are largest near the bottom, where the effective degrees of freedom are smaller due to fewer total profiles in that depth range (Figure 5.7), as well as between 2000 m - 3000 m, which corresponds to an increase in vertical temperature gradient associated with the transition between NADW and other mode and intermediate waters (Talley et al., 2007).

The warming trend between 2014 and 2023 is positive and statistically significant below 4000 m in the basin. The average warming below 4000 m is 2.2 ±0.25 m m^{o}C yr^{-1} with the highest rate of temperature increase found near 5000 m of 4.1±0.31 m m^{o}C yr^{-1} (Figure 5.5,5.6). Between 5000 m and the bottom the rate of increase in Θ is roughly 3.1 ±0.3 m m^{o}C yr^{-1} and is consistent with previous studies which have found similar rate of warming in the abyssal AABW layers of the Southwest Pacific Basin (Purkey & Johnson, 2010; Purkey et al., 2019; G. C. Johnson et al., 2019). Although the layers shallower than 4000 m have warmed on average 21 ±3 ^{o}C compared to the WOCE climatology period (Figure 5.4), a cooling trend has been observed by the floats in the 9 year period of -1.2 ±0.28 m m^{o}C yr^{-1} between 4000 m and 2000 m, with a maximum cooling trend near 2500 m of -1.96 ±0.46 m m^{o}C yr^{-1} (Figure 5.6). The accelerated warming in the deep and abyssal waters below 4000 m is associated with isotherm heaving and the shrinking in the volume of the AABW layer and homogenization of temperature

and density gradients for much of the basin westward of the East Pacific Rise ($\sim 130^o$W).

We calculate the total steric anomaly integrated between 2000 m and the bottom for all 4954 profiles and find the average deep steric expansion of 7.9 ± 1 mm compared to the climatology. The float data indicate that the trend in deep steric contribution to the local sea level rise budget is 1.3 ± 1.6 mm dec^{-1} (Figure 5.8). While the data along the float trajectories show a seasonal dependence to the deep steric variability integrated up to 2000 m (Figure 5.3), seasonality diminishes considerably below 3500 m and is negligible below 4500 m. Seasonality in the deep steric signal as well as the total integrated steric signal has a spatial functional dependence too, where mesoscale eddy activity especially between the Tonga-Kermadec Trend (179^oW) and East Pacific Rise, as well as Ekman pumping within the sub-tropical gyre can perturb the underlying steric field (Chelton et al., 2011; Hernández-Guerra & Talley, 2016). Overall, the deep steric trends in the Southwest Pacific basin are robust and statistically significant over the 9 year period considered here. We also find agreement between our estimates and previous estimates in the basin using decadal hydrographic surveys (Purkey & Johnson, 2010), in addition to global mean residual estimates computed using residuals combining satellite altimetry and gravimetry (Llovel et al., 2019; Cazenave et al., 2018; Horwath et al., 2022).

5.3.2 Sea Level Budget Closure in a $5^o \times 5^o$ Region : A Case for Sustained Deep Argo Measurements

We formulate a local sea level budget in the Southwest Pacific Basin using the sea level budget equation in Section 5.2.1 (Equation 5.2) in a $5^o \times 5^o$region between 30^oS and 35^o and 170^oW and 165^oW (Figure 5.9, grey box). We estimate terms in the sea level budget equation using satellite and gridded data products, with the exception of adding the "deep steric" signal measured by Deep Argo floats in the basin. We estimate $MSL(t)$, the sea surface anomaly using AVISO's gridded sea surface anomaly product, $MSL_{\text{mass}}(t)$ using NASA GRACE JPL RLM06 mascons solutions (Wiese et al., 2016) and $MSL_{\text{steric}_{(0-2000)}}(t)$ using the Argo climatology (Roemmich & Gilson, 2009).

Data from three floats in the region (WMO ID: 5902444, 5902528, 5905760) are used to estimate $MSL_{\text{steric}_{(2000-btm)}}(t)$ within the confines of the $5^o \times 5^o$ region of study. Data prior to 2016 only contain steric contribution from the upper 2000 m estimated from the Argo Climatology. However, with the additional deep steric information available post-2016, we estimate an average deep steric contribution from three floats of 7.2mm to the total steric anomaly between 2016 and 2023 (Figure 5.12, purple). The estimates from the 3 floats in the $5^o \times 5^o$ region are within the our previously calculated estimates for the basin below 2000 m of 7.9 ± 1 mm (Section 5.3.1)

All terms in Equation 5.2 show a strong seasonal cycle in this region of the subtropical South Pacific. Amplitudes in sea level anomaly (SLA) are 50 mm or greater in most years. Steric (0-2000 m), Full Steric (0-5750 m) and GRACE data show roughly similar amplitudes and seasonal variability of roughly 25-30 mm (Figure 5.11). Next, we determine the value of in-situ deep steric measurements in the sea level budget by computing the residual between SLA and the Steric signal (SLA - Deep Argo and SLA - Argo, respectively) which are compared against satellite-derived GRACE mass anomaly estimates (Figure 5.12). We find that both residual estimates lead the GRACE signal by 3 months, calculated using a lag correlation between the two signals (Figure 5.12,a).

A 3-month correction between the GRACE and residual estimates renders a much better match with the original GRACE and residual data (Figure 5.12,b). With the 3-month lag-correction, the average yearly amplitude shows a mean absolute difference between GRACE and SLA - Deep Argo estimates of 3±0.25 over the period between 2016 and 2022, excluding the the period between June 2017-June 2018 between the GRACE and GRACE-Follow On mission which render no data, as seen in the GRACE time series (Figure 5.11,5.12). However, as seen in Figure 5.12, at sub-yearly and inter-monthly time scales the disagreement is larger and could be due to a variety of factors including different footprints of the satellite data in space and in time, artifacts of various interpolation and mapping schemes used to create the gridded products among others.

We find that the residual estimates which incorporate the deep steric anomaly from

Deep Argo (SLA - Deep Argo, Figure 5.12a,b, blue) explains roughly 5% more variance in the underlying GRACE signal than the residual without this estimate. While the increase in explained variance is comparatively modest, we note the small spatial scale of the sea level budget analysis. Incorporating more float data over a larger spatial scale as well as averaging out satellite signals from a larger swath of the Southwest Pacific could perhaps yield more favorable results. Assessing the reasons behind lag in the seasonal signal of GRACE data in the region compared to the SLA and Steric signals is a potential direction for future analysis. Previous studies on constraining the global sea level budget (e.g., Chen et al., 2020) have found systematic phase differences of $\sim 10^o$ between GRACE and SLA - Steric and have attributed it to artifacts in the global mean atmospheric mass signal, which need to be removed from both spherical harmonic and mascon solutions, and can have a notable impact in the overall agreement between the residual estimates and GRACE data.

5.4 Discussion and Conclusions

Using Deep Argo float data in the Southwest Pacific basin from the past 9 years we find that the AABW layer in the basin has warmed on average between 12±4 m ^{o}C (Figure 5.4) compared to the WOCE-era leading to the disappearance of the coldest isotherms and reducing stratification in abyssal parts of the basin, consistent with other studies that have relied on decadal hydrographic observations (Purkey & Johnson, 2010; Lele et al., 2021). The data also show substantial warming at mid-depths between 2000 m - 4000 m with a peak warming 30±2.8 m ^{o}C. The availability of nearly a decade of full-depth bi-monthly observations spanning the basin with over 4954 profiles prove valuable in reducing statistical uncertainty, which can often plague the determination of statistical significance in results from decadal hydrographic observations.

The rate of warming implied by our results is also consistent with the idea of accelerated warming in the deepest portions of the basin. Hydrographic data collected between the 1990s and 2000s found the warming rate to be roughly 1 m^{o}C yr^{-1} (Purkey & Johnson, 2010) in the basin,

which had accelerated to 2 m^{o}C yr^{-1} in the subsequent decade between 2000s and 2010s (Purkey et al., 2019). Further more, a similar study conducted using Deep Argo within the basin found warming rates between 3±1 m^{o}C yr^{-1} in the bottom water regime below 5000 m (G. C. Johnson et al., 2019). Here, we find the warming trends to be slightly higher than previously estimated of 3.1 ±0.3 m^{o}C yr^{-1} below 5000 m peaking at maximum of 4.1 ±0.31 m^{o}C yr^{-1} and a rate below 4000 m of 2.2 ±0.25 m m^{o}C yr^{-1}.

We note that the using a decadal climatology such as WOCE which uses sparse hydrographical data from ship-based surveys, mapped into an optimally interpolated product can introduce additional uncertainty and bias in the results. Regions in the basin such as the East Pacific Rise and the abyssal plains west of the Rise with multiple different repeat hydrographic lines passing through them (e.g. P06, P15 and P16 and P31), could have much less uncertainty and better signal-to-noise ratios than large swaths of regions with only one or two decadal full-depth observations. However, temperature anomalies and trends calculated from thousands of profiles over almost a decade, as well as agreement with past estimates in the basin, lend substantial credence to the results presented in this study.

A key advantage of Deep Argo measurements is the ability to make full-depth temperature, salinity measurements at high temporal resolution which allow for estimation of the full steric anomaly signal. The data collected from floats in various parts of the basin can provide valuable in-situ observations at sub-monthly temporal resolution in order to monitor seasonal to interannual changes and trends in the deep ocean without the need to rely only on decadal repeat hydrographic observations, as well as reducing statistical uncertainty in these estimates with the sheer number of total observations collected.

We use the simultaneous temperature and salinity measurements by all the 55 floats in the basin to compute density anomalies and steric anomalies compared to the WOCE climatological data, at each each vertical level between 2000 m and 5750 m or the bottom using Equation 5.1 (e.g. Figure 5.3b). Our estimate of deep steric sea level rise of 1.3 ± 1.6 mm dec^{-1} is robust and falls within previous estimates in the basin conducted using hydrography, as well as other global

estimates using residual sea level rise budget calculations (Purkey & Johnson, 2010; Purkey et al., 2019; Llovel et al., 2019). We also demonstrate a slight improvement in the overall closure of a local sea level budget estimated within a $5^o \times 5^o$ region of the basin. Overall, when the vision of a global Deep Argo array is realized, the data will prove invaluable in providing insights into the changing abyssal oceans, better inform climate models and future projections of sea level rise.

Acknowledgements

We thank the WOCE program for collection of the hydrographic data used in the development of the WOCE hydrographic climatology. Thanks to the crews and science parties of various research vessels for Deep Argo float. Floats were largely built and deployed by the Scripps Institution of Oceanography (SIO) Instrument Development Group as part of the US Argo Program. The Argo data were downloaded from Argo Global Data Assembly Center. GRACE/GRACE-FO Mascon data are available at http://grace.jpl.nasa.gov. The sea level anomaly product can be downloaded from https://www.aviso.altimetry.fr/en/data/products/sea-surface-height-products/global/gridded-sea-level-heights-and-derived-variables.html . The Argo data were collected and made freely available by the International Argo Program and the national programs that contribute to it (http://www.argo.ucsd.edu, http://argo.jcommops.org). The Argo Program is part of the Global Ocean Observing System. Lele was supported by the NASA FINESST program (Grant 80NSSC20K1609) and NSF (OCE-2023289). Purkey was supported by US NOAA Argo Program (NOAA - NA20OAR4320278).

Chapter Five, is currently being prepared for submission for publication of the material. R. Lele and S.G. Purkey, A Full-Depth Sea Level Rise Budget in the Southwest Pacific Basin using Deep Argo (In Preparation, Preliminary Title). The dissertation author was the primary investigator and author of this material.

Figures

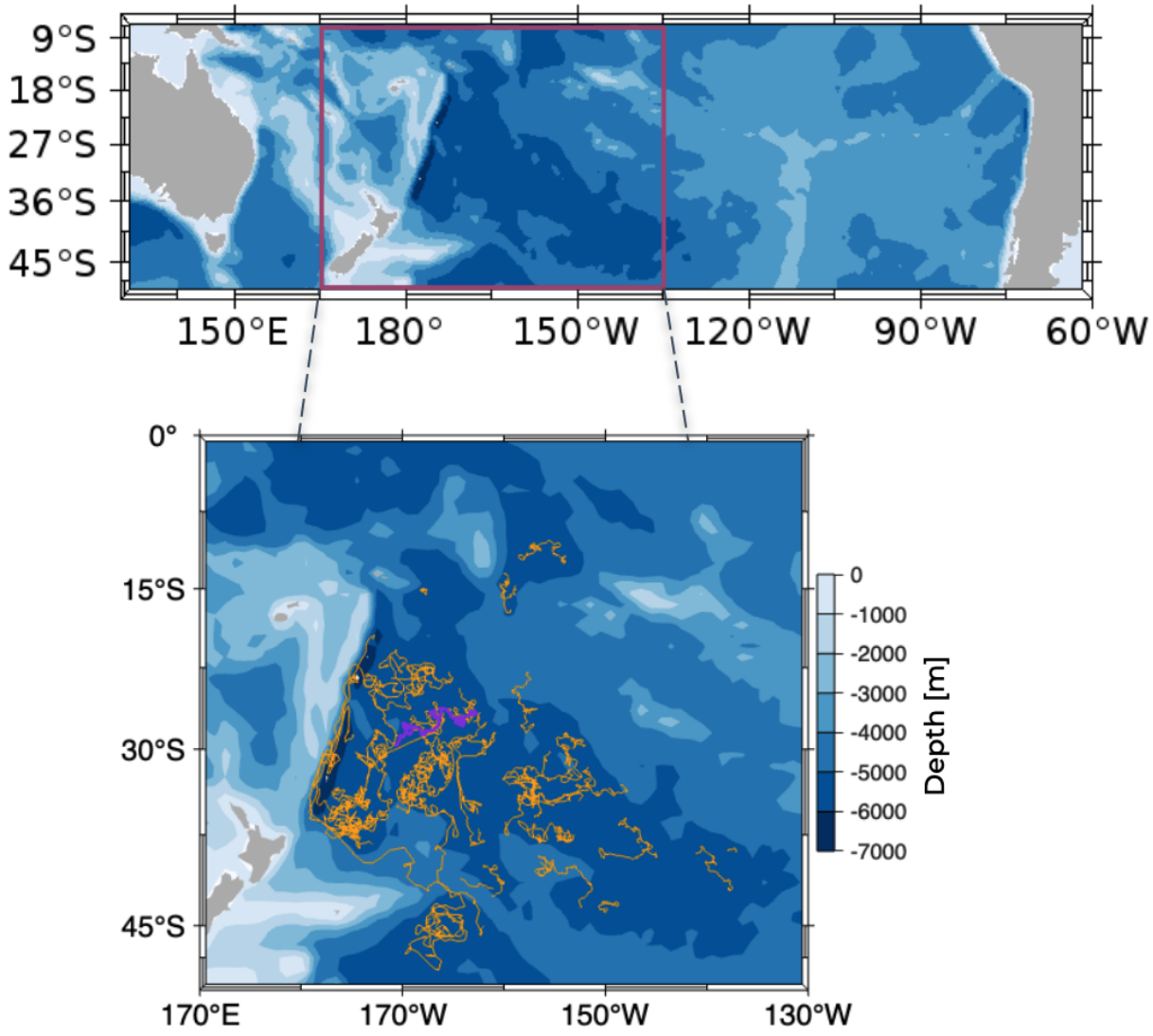

Figure 5.1. (Top) Map of the South Pacifc with the Southwest Pacific Basin highlighted (purple). (Bottom) The location of 55 Deep Argo floats in the Southwest Pacific Basin used in the study. Purple marks the location of float profiles shown in Figure 5.2 and 5.3.

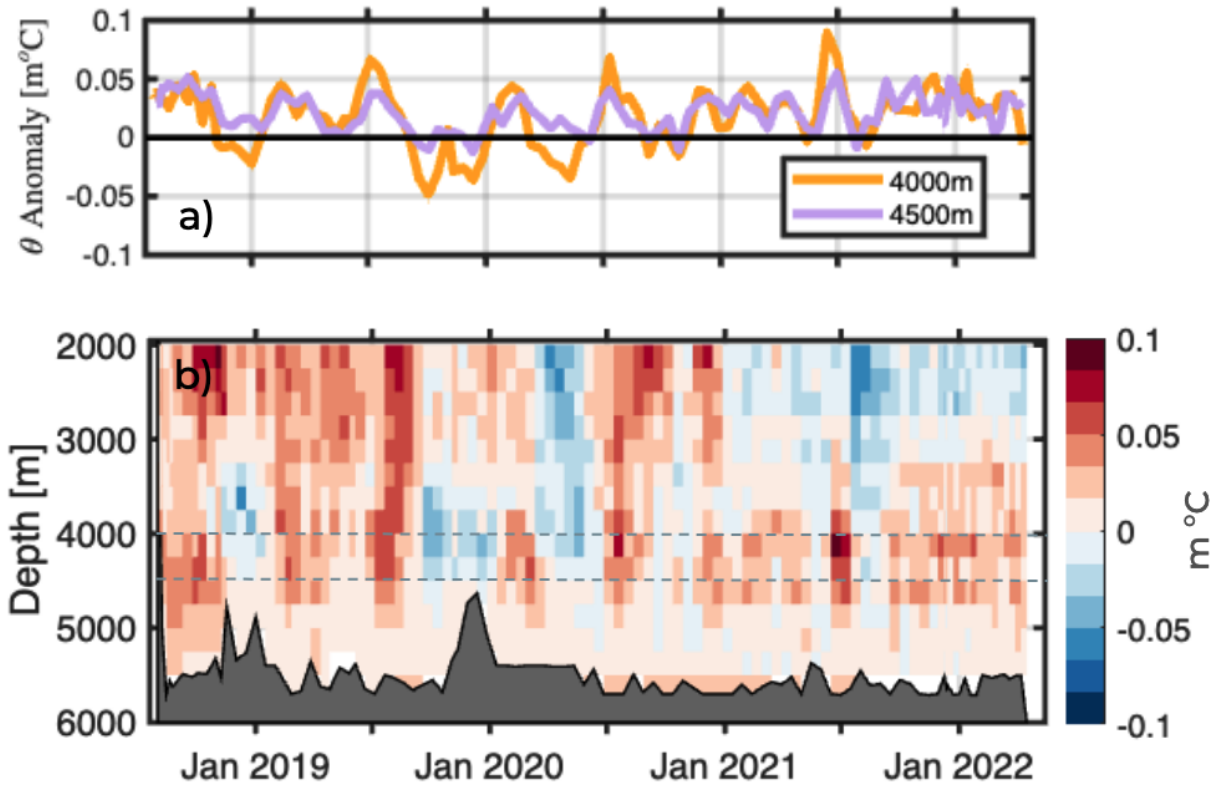

Figure 5.2. a) Conservative Temperature (Θ) anomaly time series at 4000 m and 4500 m computed with respect to the WOCE hydrographic climatology along the Deep Argo float trajectory (Figure 5.1, purple), b) Θ anomalies along the float trajectory between 2000 m and the bottom, also computed referenced to the WOCE climatology. Locations of time series in panel a) marked by the horizontal dashed line

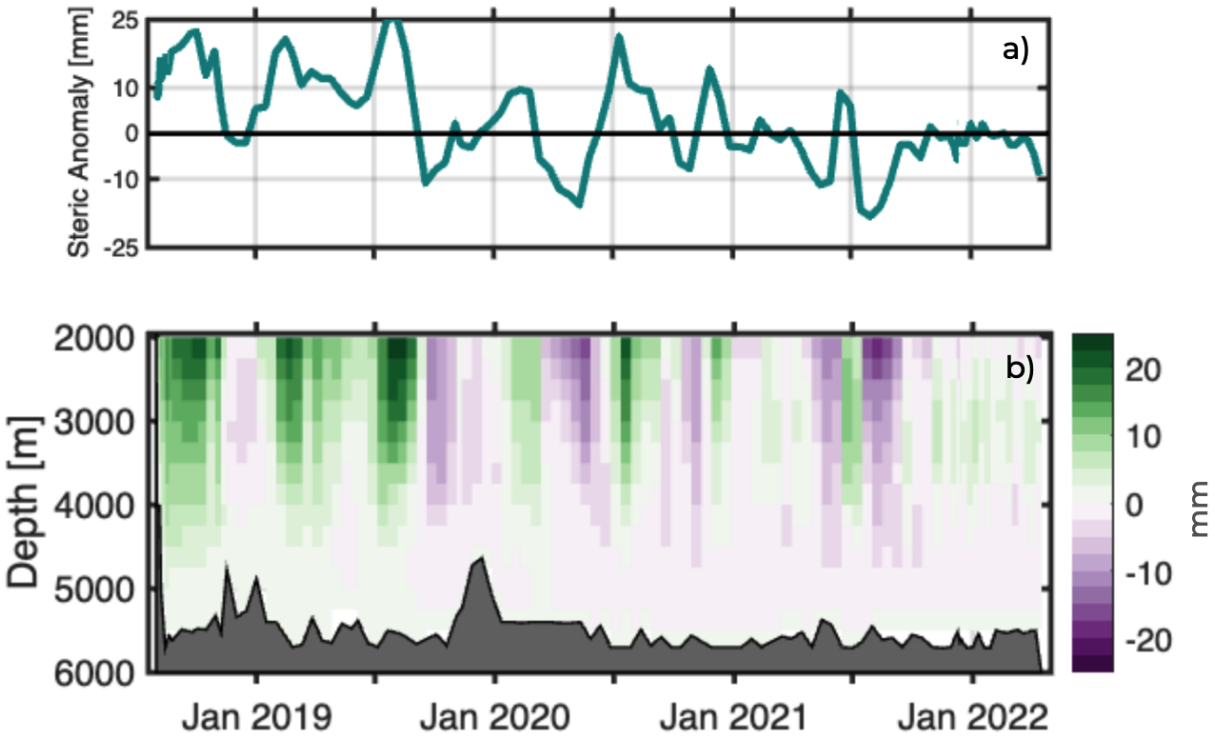

Figure 5.3. Steric Anomaly(2000 m-5750 m) time series (top) and Steric Anomaly along one Deep Argo float referenced to the WOCE climatology along the float trajectory. Float location in the basin shown is shown in Figure 5.1 (purple).

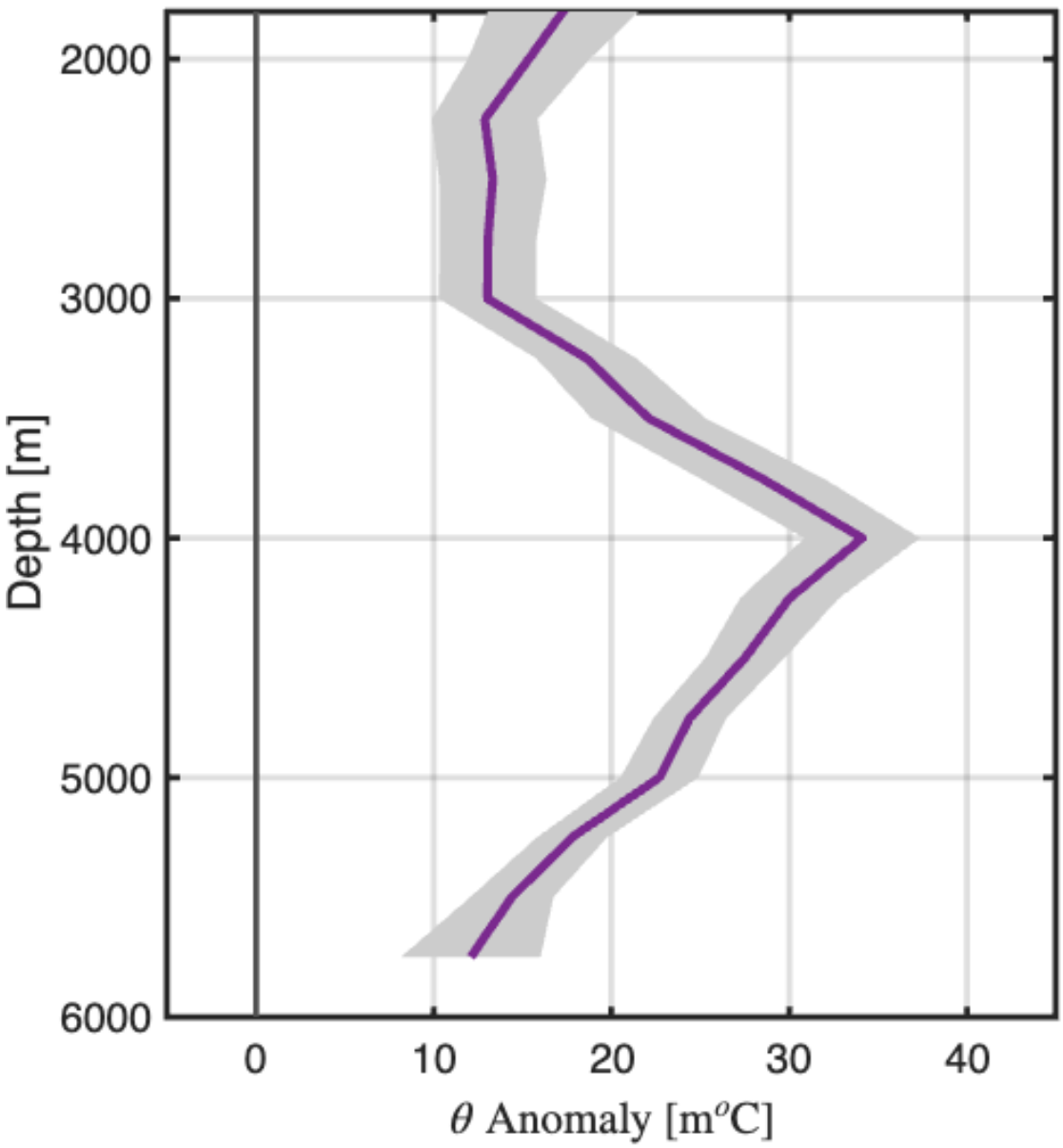

Figure 5.4. Conservative temperature Θ anomaly computed using all Deep Argo profiles in the basin with 95% confidence intervals (grey shading).

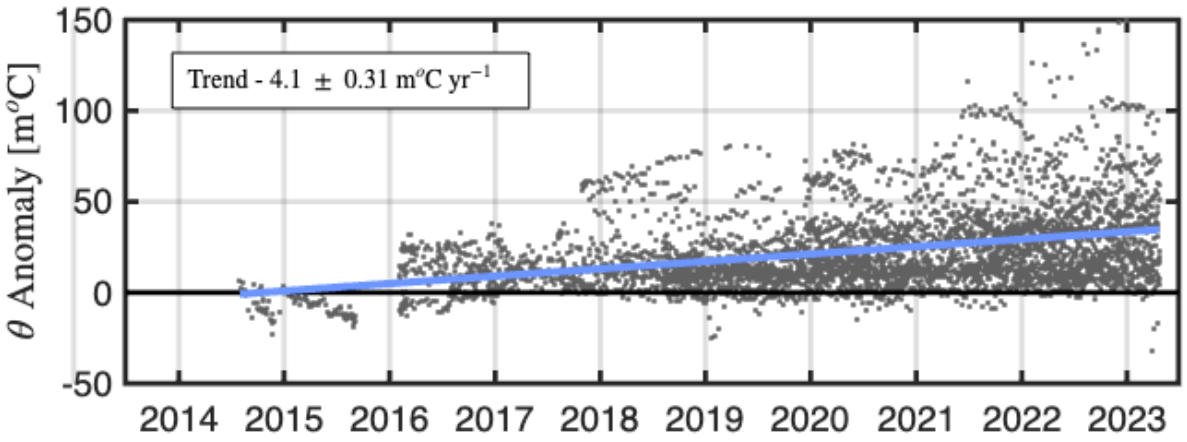

Figure 5.5. Θ anomaly trend [m^{o}C yr^{-1}] computed at 5000 m using all available Deep Argo profiles in the basin. The anomaly and confidence intervals are the same as in Figure 5.6.

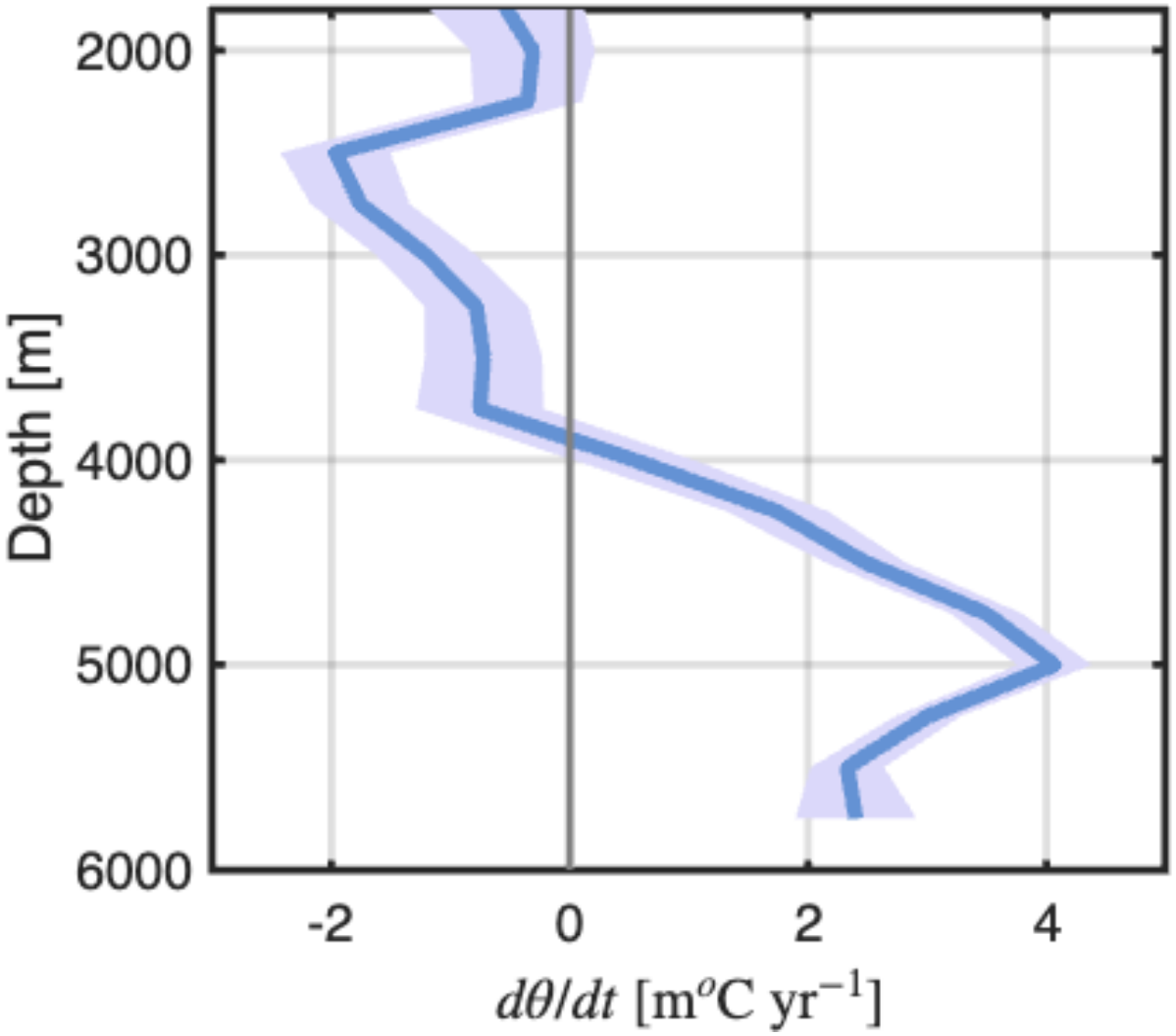

Figure 5.6. Θ anomaly trend [m^{o}C yr^{-1}] computed between each each vertical depth level between 2000 m and 5750 m with 95% confidence intervals (purple shading).

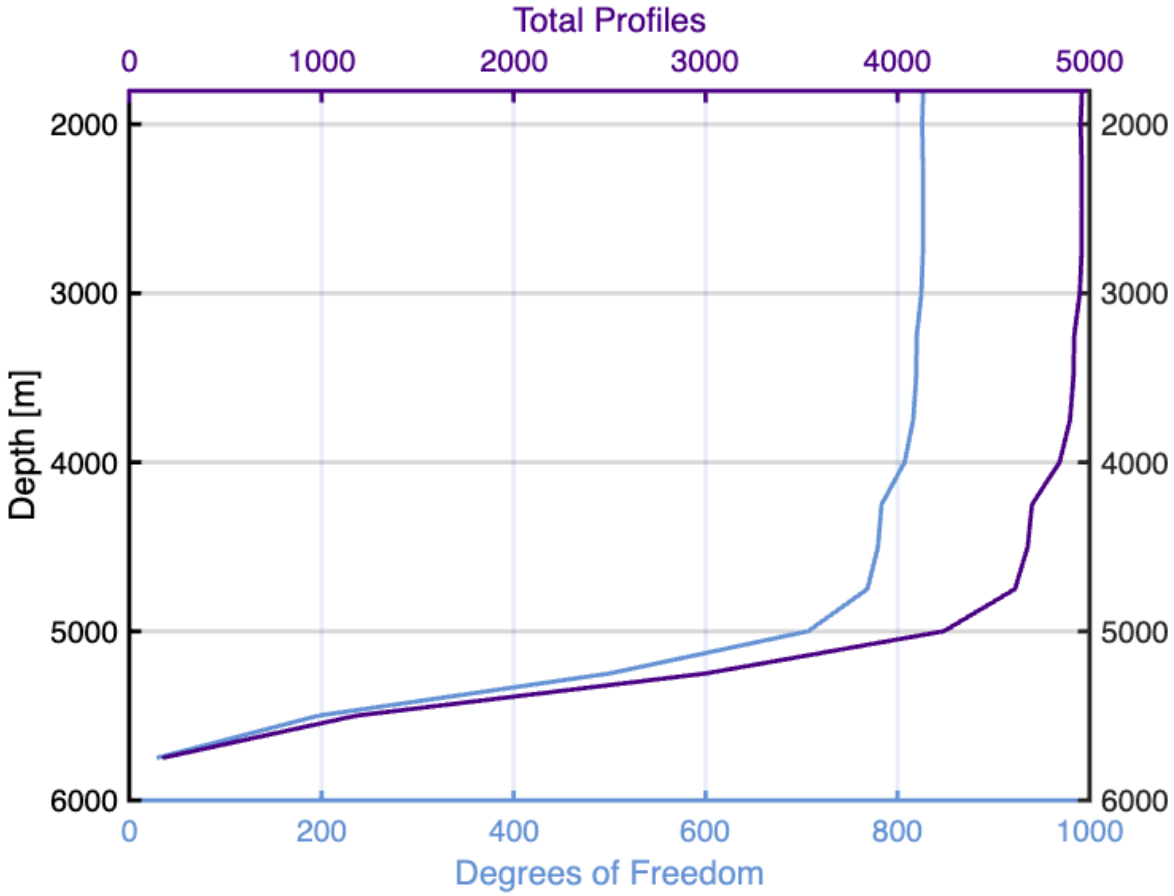

Figure 5.7. Degrees of freedom (blue) and total number of profiles (purple) as a function of depth used for calculating linear fits versus time as a function of depth (e.g. Figure 5.5,5.6).

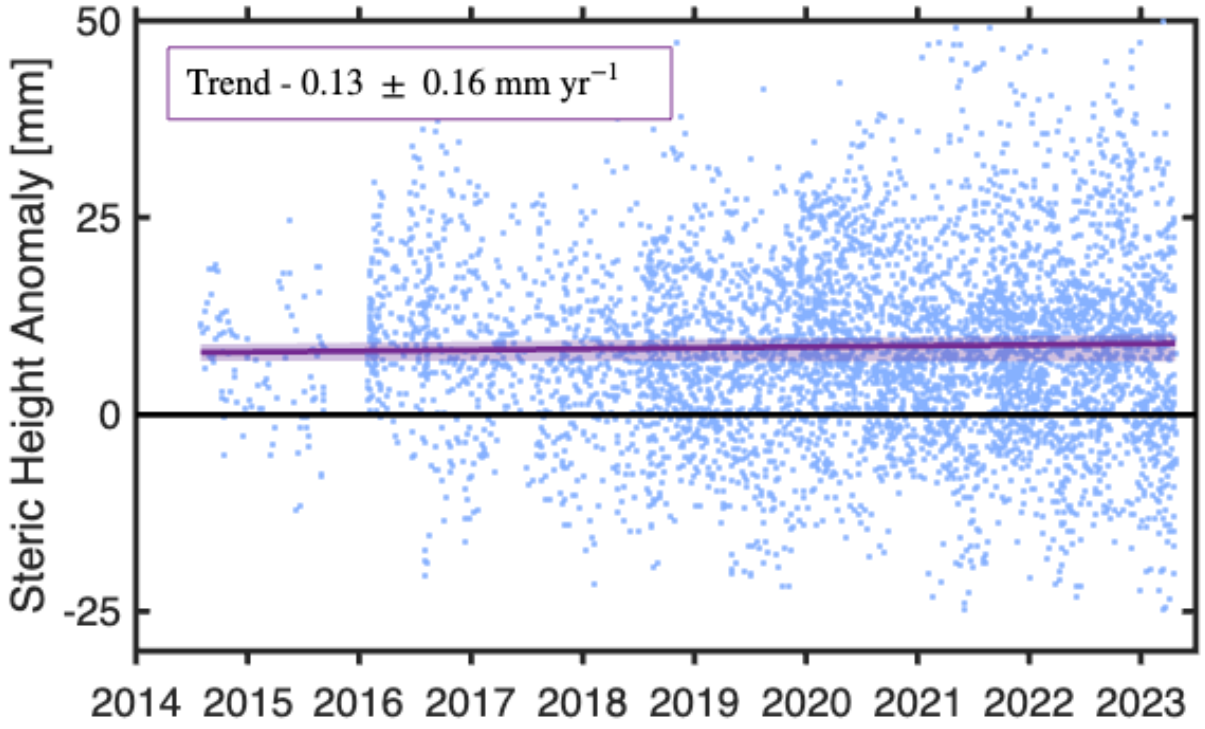

Figure 5.8. Trend in deep steric anomalies [mm yr $^{-1}$] between 2000 m and 5750 m computed from data from all Deep Argo profiles used in the study.

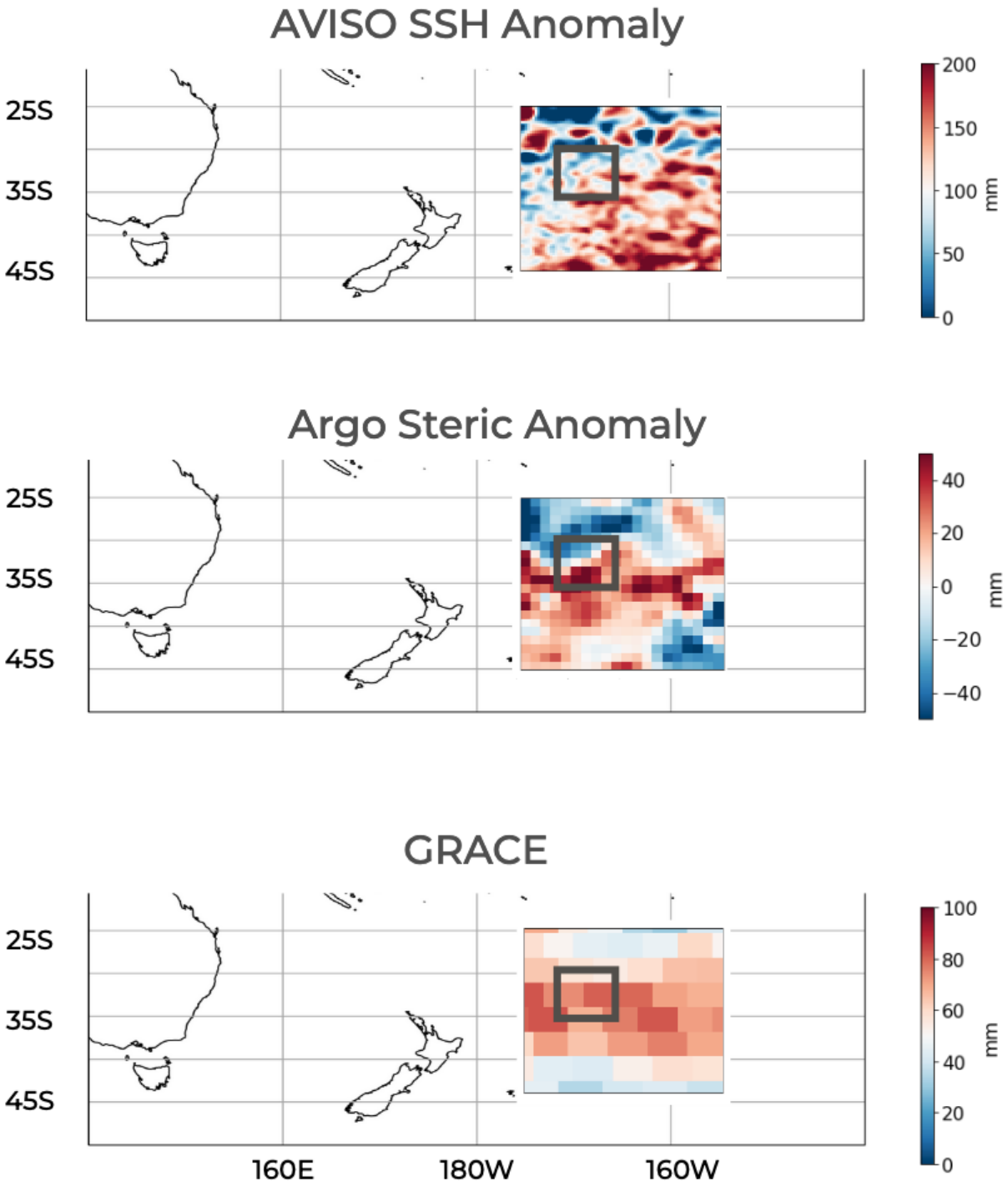

Figure 5.9. Components of the sea level budget in the Southwest Pacific Basin, a) Sea surface height (SSH) anomalies b) Steric anomalies (0-2000 m) derived from Argo climatology and c) mass anomalies from NASA GRACE JPL RL06M mascon solutions. The $5^o \times 5^o$ region considered for the sea level budget in the study is shown in the grey box.

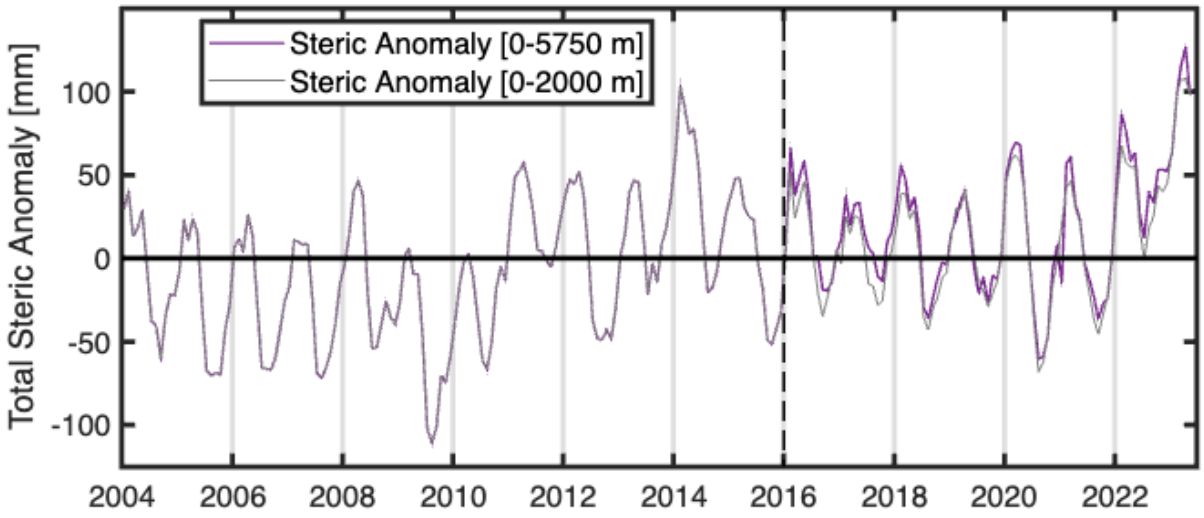

Figure 5.10. Steric Anomaly between 0-2000 m calculated from Argo Climatology. We add the deep steric component using 3 deep Argo floats in the 5x5 region considered in the sea level budget (Figure 5.9, grey box)

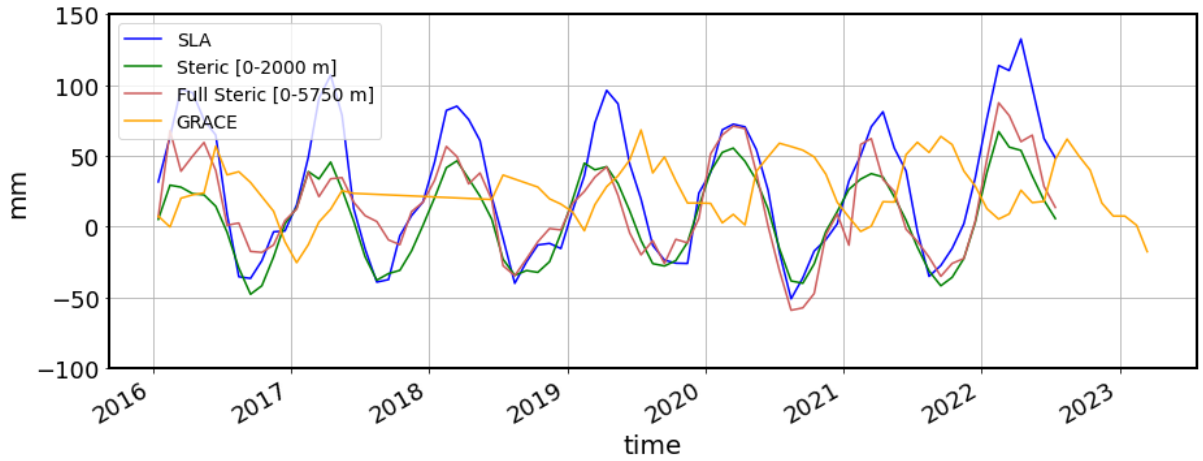

Figure 5.11. Times series of the components in the sea level budget considered in the study in the 5x5 degree region of the Southwest Pacific Basin. To consider the contribution of the deep steric estimates made using Deep Argo to the budget, we only consider the time period beyond 2016 marking the beginning of the float deployment in this 5x5 region.

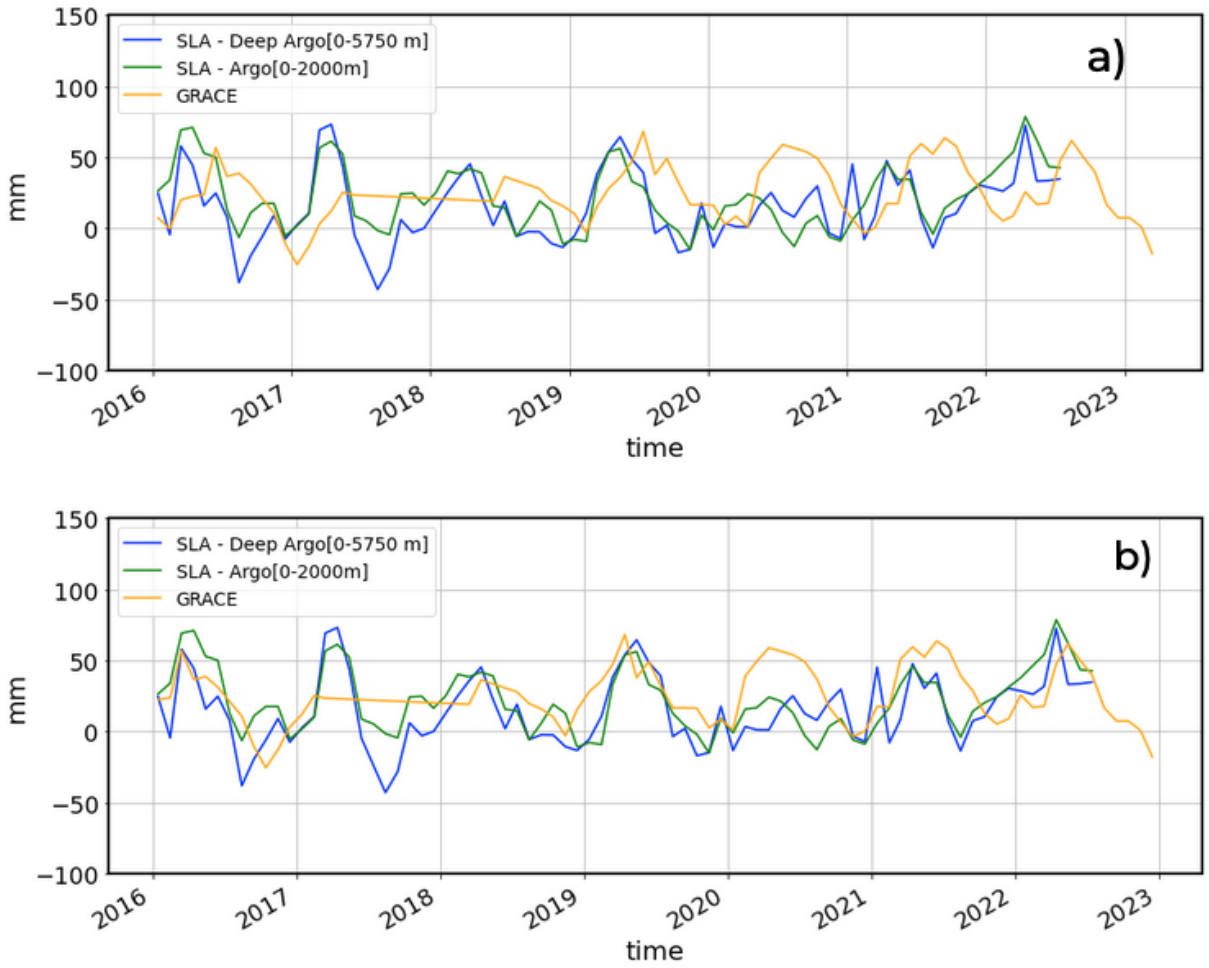

Figure 5.12. a) Residuals calculated by taking the difference between sea level anomaly (SLA) and the full steric signal (Deep Argo 0-5750 m) in blue, residual difference between SLA and the upper ocean (0-2000 m) steric anomaly from Argo climatology (green) compared to the GRACE mass anomalies (orange), b) same as a) but with a 3-month lag applied to the GRACE data.

Summary and Concluding Statements

Observing and documenting changes in the deep and abyssal oceans, a precursor to understanding its circulation, dynamics and role in the global climate system has been a grand challenge since the early days in the field observational physical oceanography. Obtaining reliable physical measurements from the remote and harsh environment in the abyss poses a significant logistical and engineering challenge. Despite this, the modern-era of physical oceanography is blessed with the development of novel instrumentation, data infrastructure, funding resources as well the collective mental bandwidth of passionate oceanographers world over to make scientific advances in leaps and bounds in furthering our understanding of the vast unknowns of the abyss.

This thesis is a small scientific endeavor to that end, incorporating observations from ship-based hydrographic data, novel instrumentation characterizing the nature of turbulence in the ocean, autonomous float measurements as well as novel machine learning approaches to parse the wealth of data collected from these instrumentation. In particular, we demonstrate using a variety of techniques, our current ability to measure and monitor large-scale circulation with data gathered on ships spanning three decades (Chapter 2), we develop a statistical methodology to filter our spurious and contaminated data from noisy measurements of oceanic turbulence from a novel instrumentation deployed on ships (Chapter 3). We use thousands of ship-based measurements combined with machine learning to identify unique spectral characteristics in oceanic shear and strain, which induce biases in current mixing parameterizations (Chapter 4), and finally with the use of data collected by novel Deep Argo autonomous floats, we estimate the rate of sea level rise and contribution of the deep and abyssal ocean warming to the sea level budget in the Southwest Pacific (Chapter 5).

As we attempted to answer some of these questions outlined in the thesis, more unanswered questions and directions for inquiry have emerged from it. For example, how is the large-scale circulation and transport of cold, dense waters of Antarctic origin changing in ocean basins globally and are there better approaches to resolve these changes than through hydrography at decadal timescales? What is the spatial distribution and geography of mixing in the abyssal ocean and what are underlying mechanisms and processes in these regions which result in turbulent mixing? What innovative approaches could be applied to extract and identify signatures and various forms of internal wave activity in the ocean, how different are deep steric changes in various deep ocean basins global and what is the rate of increase in heat storage and sea level rise potential from the deep ocean in areas around the globe?

The future of our further understanding and answers to some of these questions lie in the rapid innovation in the ocean observing technologies. For example - sensitive instrumentation such as the χ-Pod deployed on CTD rosettes combined with reliable quality control procedures has the potential to yield a wealth of high resolution data and engender greater insights into the spatial distribution of turbulent mixing from the ocean surface to the abyssal bottom boundary layer. Furthermore, Deep Argo's expansion from the pilot phase into basins globally will be critical to obtaining a high resolution mapping of the world's global deep ocean at monthly to bi-monthly resolution. Overall, this work reiterates the pivotal role that high quality oceanographic observations play in furthering our understanding of the deep ocean's role in modulating the climate system, and it makes a case for continued sustained observations in the abyss.

Bibliography

Ablain, M., Cazenave, A., Larnicol, G., Balmaseda, M., Cipollini, P., Faugère, Y., . . . Benveniste, J. (2015). *Improved sea level record over the satellite altimetry era (1993-2010) from the Climate Change Initiative project.* doi: 10.5194/os-11-67-2015

Abraham, J., Baringer, M., Bindoff, N., Boyer, T., Cheng, L., Church, J., . . . others (2013). A review of global ocean temperature observations: Implications for ocean heat content estimates and climate change. *Reviews of Geophysics*, *51*(3), 450–483.

Alford, M., & Pinkel, R. (2000). Patterns of turbulent and double diffusive phenomena: Observations from a rapid profiling conductivity probe. *J. Phys. Oceanogr.*, *30*, 833-854.

Alford, M. H. (2003). Improved global maps 54-year history of wind-work on ocean inertial motions. *Geophysical Research Letters*, *30*. doi: 10.1029/2002GL016614

Alford, M. H., Gerdt, D. W., & Adkins, C. M. (2006). An ocean refractometer: Resolving millimeter-scale turbulent density fluctuations via the refractive index. *J. Atmos. Ocean. Tech.*, *23*(1), 121–137.

Batchelor, G. K. (1959). Small-scale variation of convected quantities like temperature in turbulent fluid Part 1. General discussion and the case of small conductivity. *J. Fluid Mech.*, *5*(1), 113–133.

Berry, M. W., Browne, M., Langville, A. N., Pauca, V. P., & Plemmons, R. J. (2007). Algorithms and applications for approximate nonnegative matrix factorization. *Computational Statistics and Data Analysis*, *52*(1), 155–173. doi: 10.1016/j.csda.2006.11.006

Bindoff, N. L., Willebrand, J., Artale, V., A, C., Gregory, J., Gulev, S., . . . Unnikrishnan, A. (2007). Climate Change 2007: The Physical Science Basis. Contribution of Working Group I to the Fourth Assessment Report of the Intergovernmental Panel on Climate Change. In S. Solomon et al. (Eds.), (chap. Observations: Oceanic Climate Change and Sea Level.). New York: Cambridge University Press.

Bishop, C. M. (2006). *Pattern recognition and machine learning*. New York : Springer, [2006] ©2006.

Boehme, L., & Rosso, I. (2021). Classifying Oceanographic Structures in the Amundsen Sea, Antarctica. *Geophysical Research Letters*, *48*(5). doi: 10.1029/2020GL089412

Bogucki, D., Dickey, T., & Redekopp, L. (1997). Sediment resuspension and mixing by resonantly generated internal solitary waves. *J. Phys. Oceanogr.*, *27*(7), 1181–1196.

Bogucki, D., Luo, H., & Domaradzki, J. (2012). Experimental evidence of the Kraichnan scalar spectrum at high Reynolds numbers. *Journal of physical oceanography*, *42*(10), 1717–1728.

Böning, C. W., Dispert, A., Visbeck, M., Rintoul, S. R., & Schwarzkopf, F. U. (2008). The response of the antarctic circumpolar current to recent climate change. *Nature Geoscience*, *1*(12), 864–869. doi: 10.1038/ngeo362

Brink, K. H. (1995). Tidal and lower frequency currents above Fieberling Guyot. *Journal of Geophysical Research*, *100*. doi: 10.1029/95jc00998

Brunton, S. L., Noack, B. R., & Koumoutsakos, P. (2020). *Machine Learning for Fluid Mechanics.* doi: 10.1146/annurev-fluid-010719-060214

Bryan, F. (1987). Parameter sensitivity of primitive equation ocean general circulation models. *Journal of Physical Oceanography*, *17*, 970–985. doi: 10.1175/1520-0485(1987)017⟨0970:psopeo⟩2.0.co;2

Callaham, J. L., Koch, J. V., Brunton, B. W., Kutz, J. N., & Brunton, S. L. (2021). Learning dominant physical processes with data-driven balance models. *Nature Communications*, *12*(1016). doi: 10.1038/s41467-021-21331-z

Callies, J., Ferrari, R., Joern, C., & Ferrari Raffaele. (2018). Dynamics of an Abyssal Circulation Driven by Bottom-Intensified Mixing on Slopes. *Journal of physical oceanography*, *48*(6), 1257–1282. doi: 10.1175/JPO-D-17-0125.1

Cazenave, A., Dominh, K., Guinehut, S., Berthier, E., Llovel, W., Ramillien, G., . . . Larnicol, G. (2009). Sea level budget over 2003-2008: A reevaluation from GRACE space gravimetry, satellite altimetry and Argo. *Global and Planetary Change*. doi: 10.1016/j.gloplacha.2008.10.004

Cazenave, A., Meyssignac, B., Ablain, M., Balmaseda, M., Bamber, J., Barletta, V., . . . Wouters, B. (2018). Global sea-level budget 1993-present. *Earth System Science Data*, *10*(3), 1551–1590. doi: 10.5194/essd-10-1551-2018

Chambers, D. P. (2006). Observing seasonal steric sea level variations with GRACE and satellite altimetry. *Journal of Geophysical Research: Oceans*, *111*(3), 1–13. doi: 10.1029/2005JC002914

Chambers, D. P., Cazenave, A., Champollion, N., Dieng, H., Llovel, W., Forsberg, R., ... Wada, Y. (2017). *Evaluation of the Global Mean Sea Level Budget between 1993 and 2014.* doi: 10.1007/s10712-016-9381-3

Chambers, D. P., & Willis, J. K. (2010). A global evaluation of ocean bottom pressure from GRACE, OMCT, and steric-corrected altimetry. *Journal of Atmospheric and Oceanic Technology*, *27*(8), 1395–1402. doi: 10.1175/2010JTECHO738.1

Chatfield, C., Bendat, J. S., & Piersol, A. G. (1987). Random Data: Analysis and Measurement Procedures. *Journal of the Royal Statistical Society. Series A (General)*. doi: 10.2307/2981634

Chelton, D. B., Schlax, M. G., & Samelson, R. M. (2011). Global observations of nonlinear mesoscale eddies. *Progress in Oceanography*, *91*(2), 167–216.

Chen, J., Tapley, B., Wilson, C., Cazenave, A., Seo, K. W., & Kim, J. S. (2020). Global Ocean Mass Change From GRACE and GRACE Follow-On and Altimeter and Argo Measurements. *Geophysical Research Letters*, *47*(22), 1–9. doi: 10.1029/2020GL090656

Cheng, L., Abraham, J. P., Hausfather, Z., & Trenberth, K. E. (2019). *How fast are the oceans warming?* doi: 10.1126/science.aav7619

Cheng, L., Trenberth, K. E., Fasullo, J., Boyer, T., Abraham, J. P., & Zhu, J. (2017). *Improved estimates of ocean heat content from 1960 to 2015.* doi: 10.1126/sciadv.1601545

Chinn, B. S., Girton, J. B., & Alford, M. H. (2016). The impact of observed variations in the shear-to-strain ratio of internal waves on inferred turbulent diffusivities. *Journal of Physical Oceanography*, *46*(11), 3299–3320. doi: 10.1175/JPO-D-15-0161.1

Church, J., & White, N. J. (2006). A 20th century acceleration in global sea-level rise. *Geophysical Research Letters*, *33*. doi: 10.1029/2005GL024826

Church, J., & White, N. J. (2011). Sea-Level Rise from the Late 19th to the Early 21st Century. *Surveys in Geophysics*, *32*. doi: 10.1007/s10712-011-9119-1

Cimoli, L., Mashayek, A., Johnson, H. L., Marshall, D. P., Naveira Garabato, A. C., Whalen, C. B., ... MacKinnon, J. A. (2023). Significance of diapycnal mixing within the Atlantic meridional overturning circulation. *AGU Advances*, *4*(2), e2022AV000800.

Dangendorf, S., Marcos, M., Wöppelmann, G., Conrad, C. P., Frederikse, T., & Riva, R. (2017). Reassessment of 20th century global mean sea level rise. *Proceedings of the National Academy of Sciences of the United States of America*. doi: 10.1073/pnas.1616007114

Desbruyères, D. G., Purkey, S. G., McDonagh, E. L., Johnson, G. C., & King, B. A. (2016). Deep and abyssal ocean warming from 35 years of repeat hydrography. *Geophysical Research*

Letters, *43*(19), 356–10. doi: 10.1002/2016GL070413

Dieng, H. B., Palanisamy, H., Cazenave, A., Meyssignac, B., & von Schuckmann, K. (2015). *The Sea Level Budget Since 2003: Inference on the Deep Ocean Heat Content.* doi: 10.1007/s10712-015-9314-6

Dillon, T. M. (1982). Vertical overturns: A comparison of Thorpe and Ozmidov length scales. *J. Geophys. Res.*, *87*, 9601–9613.

Dillon, T. M., & Caldwell, D. R. (1980, april). The Batchelor spectrum and dissipation in the upper ocean. *J. Geophys. Res.*, *85*(C4), 1910–1916.

Ditlevsen, P., & Ditlevsen, S. (2023). Warning of a forthcoming collapse of the Atlantic meridional overturning circulation. *Nature Communications*, *14*(1), 4254. Retrieved from https://doi.org/10.1038/s41467-023-39810-w doi: 10.1038/s41467-023-39810-w

Domingues, C., Church, J., White, N., Gleckler, P., Wijffels, S., Barker, P., & Dunn, J. (2008). Improved estimates of upper-ocean warming and multi-decadal sea-level rise. *Nature*, *453*(7198), 1090–1093.

Doos, K., & Webb, D. J. (1994). The Deacon cell and the other meridional cells of the Southern Ocean. *Journal of Physical Oceanography*, *24*. doi: 10.1175/1520-0485(1994)024⟨0429:TDCATO⟩2.0.CO;2

Drake, H. F., Ferrari, R., & Callies, J. (2020). Abyssal Circulation Driven by Near-Boundary Mixing: Water Mass Transformations and Interior Stratification. *Journal of Physical Oceanography*, *50*(8), 2203–2226. doi: 10.1175/JPO-D-19-0313.1

Egbert, G. D., & Ray, R. D. (2000). Significant dissipation of tidal energy in the deep ocean inferred from satellite altimeter data. *Nature*, *405*. doi: 10.1038/35015531

Eriksen, C. C. (1978). Measurements and models of fine structure, internal gravity waves, and wave breaking in the deep Ocean. *Journal of Geophysical Research*, *83*(C6), 2989–3009. doi: 10.1029/jc083ic06p02989

Eriksen, C. C. (1985). Implications of Ocean Bottom Reflection for Internal Wave Spectra and Mixing. *Journal of Physical Oceanography*, *15*. doi: 10.1175/1520-0485(1985)015⟨1145:ioobrf⟩2.0.co;2

Eriksen, C. C. (1998). Internal wave reflection and mixing at Fieberling Guyot. *Journal of Geophysical Research: Oceans*, *103*. doi: 10.1029/97jc03205

Feistel, R. (2012). TEOS-10: A new international oceanographic standard for seawater, ice, fluid water, and humid air. *International Journal of Thermophysics*, *33*. doi: 10.1007/

s10765-010-0901-y

Ferrari, R., Mashayek, A., McDougall, T. J., Nikurashin, M., & Campin, J.-M. (2016). Turning Ocean Mixing Upside Down. *Journal of Physical Oceanography*, *46*(7), 2239–2261. Retrieved from http://journals.ametsoc.org/doi/10.1175/JPO-D-15-0244.1 doi: 10.1175/JPO-D-15-0244.1

Ferron, B., Mercier, H., Speer, K., Gargett, A., & Polzin, K. (1998). Mixing in the Romanche Fracture Zone. *Journal of Physical Oceanography*. doi: 10.1175/1520-0485(1998)028⟨1929:MITRFZ⟩2.0.CO;2

Fukasawa, M., Freeland, H., Perkin, R., Watanabe, T., Uchida, H., & Nishina, A. (2004). Bottom water warming in the North Pacific Ocean. *Nature*, *427*, 825–827. doi: 10.1038/nature02337

Galbraith, P. S., & Kelley, D. E. (1996, june). Identifying overturns in CTD profiles. *J. Atmos. Ocean. Tech.*, *13*, 688-702.

Ganachaud, A., & Wunsch, C. (2000). Improved estimates of global ocean circulation, heat transport and mixing from hydrographic data. *Nature*, *408*(6811), 453–457. doi: 10.1038/35044048

Ganachaud, A., & Wunsch, C. (2003). Large-scale ocean heat and freshwater transports during the world ocean circulation experiment. *Journal of Climate*, *16*(4), 696–705. doi: 10.1175/1520-0442(2003)016⟨0696:LSOHAF⟩2.0.CO;2

Gargett, A. E. (1985). Evolution of scalar spectra with the decay of turbulence in a stratified fluid. *J. Fluid Mech.*, *159*, 379–407.

Gargett, A. E. (1990). Do we really know how to scale the turbulent kinetic energy dissipation rate ϵ due to breaking of oceanic internal waves? *Journal of Geophysical Research*, *95*(C9), 15971–15974. doi: 10.1029/jc095ic09p15971

Gargett, A. E., Hendricks, P. J., Sanford, T. B., Osborn, T. R., & Williams, A. J. (1981). A Composite Spectrum of Vertical Shear in the Upper Ocean. *Journal of Physical Oceanography*, *11*. doi: 10.1175/1520-0485(1981)011⟨1258:acsovs⟩2.0.co;2

Garrett, C., & Munk, W. (1972). Space-Time scales of internal waves. *Geophysical Fluid Dynamics*, *3*(3), 225–264. doi: 10.1080/03091927208236082

Garrett, C., & Munk, W. (1975). Space-time scales of internal waves: A progress report. *Journal of Geophysical Research*, *80*. doi: 10.1029/jc080i003p00291

Garrett, C., & Munk, W. (1979). Internal Waves in the Ocean. *Annual Review of Fluid Mechanics*, *11*. doi: 10.1146/annurev.fl.11.010179.002011

Giglio, D., Lyubchich, V., & Mazloff, M. R. (2018). Estimating Oxygen in the Southern Ocean Using Argo Temperature and Salinity. *Journal of Geophysical Research: Oceans*, *123*(6), 4280–4297. doi: 10.1029/2017JC013404

Gill, A. E., & Niller, P. P. (1973). The theory of the seasonal variability in the ocean. *Deep-Sea Research and Oceanographic Abstracts*. doi: 10.1016/0011-7471(73)90049-1

Goto, Y., Yasuda, I., & Nagasawa, M. (2016). Turbulence estimation using fast-response thermistors attached to a free-fall vertical microstructure profiler. *Journal of Atmospheric and Oceanic Technology*, *33*(10), 2065-2078. Retrieved from https://doi.org/10.1175/JTECH-D-15-0220.1 doi: 10.1175/JTECH-D-15-0220.1

Goto, Y., Yasuda, I., & Nagasawa, M. (2018a). Comparison of turbulence intensity from CTD-attached and free-fall microstructure profilers. *Journal of Atmospheric and Oceanic Technology*, *35*(1), 147–162. doi: 10.1175/JTECH-D-17-0069.1

Goto, Y., Yasuda, I., & Nagasawa, M. (2018b). Comparison of turbulence intensity from CTD-attached and free-fall microstructure profilers. *Journal of Atmospheric and Oceanic Technology*, *35*(1), 147-162. Retrieved from https://doi.org/10.1175/JTECH-D-17-0069.1 doi: 10.1175/JTECH-D-17-0069.1

Gould, J., Roemmich, D., Wuffels, S., Freeland, H., Ignaszewsky, M., Jianplng, X., ... Riser, S. (2004). Argo profiling floats bring new era of in situ ocean observations. *Eos*, *85*. doi: 10.1029/2004eo190002

Gouretski, V., & Koltermann, K. P. (2004). WOCE global hydrographic climatology. *Berichte des BSH*, *35*, 1–52. doi: 10.5065/GS51-V170

Grant, H. L., Stewart, R. W., & Moilliet, A. (1962). Turbulence spectra from a tidal channel. *J. Fluid Mech.*, *12*, 241–268.

Gregg, M. (1987). *Diapycnal Mixing in the Thermocline: A Review.* doi: 10.1029/JC092iC05p05249

Gregg, M. (1989). Scaling turbulent dissipation in the thermocline. *Journal of Geophysical Research*, *94*(C7), 9686–9698. doi: 10.1029/jc094ic07p09686

Gregg, M. (1999). Uncertainties and limitations in measuring ϵ and χ(T). *Journal of Atmospheric and Oceanic Technology*, *16*, 1483–1490. doi: 10.1175/1520-0426(1999)016⟨1483:ualima⟩2.0.co;2

Gregg, M., D'Asaro, E., Riley, J., & Kunze, E. (2018). Mixing Efficiency in the Ocean. *Annual Review of Marine Science*, *10*(1), 443–473. doi: 10.1146/annurev-marine-121916-063643

Gregg, M., & Kunze, E. (1991). Shear and strain in Santa Monica Basin. *Journal of Geophysical Research: Oceans*, *96*(C9), 16709–16719. Retrieved from http://dx.doi.org/10.1029/91JC01385 doi: 10.1029/91JC01385

Gregg, M., & Meagher, T. (1980). The dynamic response of glass rod thermistors. *J. Geophys. Res.*, *85*, 2779–2786.

Gregg, M., Sanford, T. B., & Winkel, D. P. (2003). Reduced mixing from the breaking of internal waves in equatorial waters. *Nature*. doi: 10.1038/nature01507

Gunn, K. L., Rintoul, S. R., England, M. H., & Bowen, M. M. (2023). Recent reduced abyssal overturning and ventilation in the Australian Antarctic Basin. *Nature Climate Change*, *13*. doi: 10.1038/s41558-023-01667-8

Hansen, J., Sato, M., Kharecha, P., & Von Schuckmann, K. (2011). Earth's energy imbalance and implications. *Atmospheric Chemistry and Physics*. doi: 10.5194/acp-11-13421-2011

Henyey, F. S., Wright, J., & Flatté, S. M. (1986). Energy and action flow through the internal wave field: An eikonal approach. *Journal of Geophysical Research*, *91*. doi: 10.1029/jc091ic07p08487

Hernández-Guerra, A., & Talley, L. D. (2016). Meridional overturning transports at 30°S in the Indian and Pacific Oceans in 2002–2003 and 2009. *Progress in Oceanography*, *146*, 89–120. doi: 10.1016/j.pocean.2016.06.005

Heywood, K. J., Naveira Garabato, A. C., & Stevens, D. P. (2002). High mixing rates in the abyssal Southern Ocean. *Nature*, *415*(6875), 1011–1014. doi: 10.1038/4151011a

Hieronymus, M., Nycander, J., Nilsson, J., Döös, K., & Hallberg, R. (2019). Oceanic overturning and heat transport: The role of background diffusivity. *Journal of Climate*, *32*. doi: 10.1175/JCLI-D-18-0438.1

Hofmann, M., & Maqueda, M. A. (2009). Geothermal heat flux and its influence on the oceanic abyssal circulation and radiocarbon distribution. *Geophysical Research Letters*, *36*(3). doi: 10.1029/2008GL036078

Hogg, N., Biscaye, P., Gardner, R., & Schmitz, W. (1982). On the transport and modification of Antarctic Bottom Water in the Vema Channel. *J. Mar. Res*, *40*(23), l-263.

Holmes, R., Moum, J., & Thomas, L. (2016). Evidence for seafloor-intensified mixing by surface-generated equatorial waves. *Geophysical Research Letters*, *43*(3), 1202–1210.

Holmes, R. M., de Lavergne, C., & McDougall, T. J. (2018). Ridges, Seamounts, Troughs, and Bowls: Topographic Control of the Dianeutral Circulation in the Abyssal Ocean. *Journal of*

Physical Oceanography, *48*(4), 861–882. doi: 10.1175/jpo-d-17-0141.1

Horwath, M., Gutknecht, B. D., Cazenave, A., Palanisamy, H. K., Marti, F., Marzeion, B., ... Benveniste, J. (2022). *Global sea-level budget and ocean-mass budget, with a focus on advanced data products and uncertainty characterisation.* doi: 10.5194/essd-14-411-2022

Huussen, T. N., Naveira-Garabato, A. C., Bryden, H. L., & McDonagh, E. L. (2012). Is the deep Indian Ocean MOC sustained by breaking internal waves? *Journal of Geophysical Research: Oceans*, *117*(8). doi: 10.1029/2012JC008236

Ijichi, T., & Hibiya, T. (2015). Frequency-based correction of finescale parameterization of turbulent dissipation in the deep ocean. *Journal of Atmospheric and Oceanic Technology*, *32*(8), 1526–1535. doi: 10.1175/JTECH-D-15-0031.1

Itsweire, E. C., Koseff, J. R., Briggs, D. A., & Ferziger, J. H. (1993). Turbulence in stratified shear flows: implications for interpreting shear-induced mixing in the ocean. *Journal of Physical Oceanography*, *23*, 1508–1522. doi: 10.1175/1520-0485(1993)023⟨1508:TISSFI⟩2.0.CO;2

Ivezic, Z., Connolly, A., Vanderplas, J., & Gray, A. (2014). *Statistics, data mining, and machine learning in astronomy: a practical Python guide for the analysis of survey data*. doi: 10.5860/choice.52-0257

Jackett, D. R., & McDougall, T. J. (1997). A neutral density variable for the world's oceans. *Journal of Physical Oceanography*, *27*(2), 237–263. doi: 10.1175/1520-0485(1997)027⟨0237:ANDVFT⟩2.0.CO;2

Jeff A. Bilmes. (1998). A Gentle Tutorial of the EM Algorithm. *International Computer Science Institute*, *4*(510).

Jiang, J., Lu, Y., & Perrie, W. (2005). Estimating the energy flux from the wind to ocean inertial motions: The sensitivity to surface wind fields. *Geophysical Research Letters*, *32*. doi: 10.1029/2005GL023289

Jochum, M., Briegleb, B. P., Danabasoglu, G., Large, W. G., Norton, N. J., Jayne, S. R., ... Bryan, F. O. (2013). The impact of oceanic near-inertial waves on climate. *Journal of Climate*, *26*. doi: 10.1175/JCLI-D-12-00181.1

Johnson, C. W., Ben-Zion, Y., Meng, H., & Vernon, F. (2020). Identifying Different Classes of Seismic Noise Signals Using Unsupervised Learning. *Geophysical Research Letters*, *47*(15), 1–10. doi: 10.1029/2020GL088353

Johnson, G. C. (2008). Quantifying Antarctic Bottom Water and North Atlantic Deep Water volumes. *Journal of Geophysical Research: Oceans*, *113*(5), 1–13. doi: 10.1029/2007JC004477

Johnson, G. C. (2022). Antarctic Bottom Water Warming and Circulation Slowdown in the Argentine Basin From Analyses of Deep Argo and Historical Shipboard Temperature Data. *Geophysical Research Letters*, *49*(18). doi: 10.1029/2022GL100526

Johnson, G. C., Cadot, C., Lyman, J. M., McTaggart, K. E., & Steffen, E. L. (2020). Antarctic Bottom Water Warming in the Brazil Basin: 1990s Through 2020, From WOCE to Deep Argo. *Geophysical Research Letters*, *47*(18). doi: 10.1029/2020GL089191

Johnson, G. C., & Chambers, D. P. (2013). Ocean bottom pressure seasonal cycles and decadal trends from GRACE Release-05: Ocean circulation implications. *Journal of Geophysical Research: Oceans*, *118*(9), 4228–4240. doi: 10.1002/jgrc.20307

Johnson, G. C., Lyman, J. M., & Purkey, S. G. (2015). Informing deep argo array design using argo and full-depth hydrographic section data. *Journal of Atmospheric and Oceanic Technology*, *32*. doi: 10.1175/JTECH-D-15-0139.1

Johnson, G. C., Purkey, S. G., Zilberman, N. V., & Roemmich, D. (2019). Deep Argo quantifies bottom water warming rates in the Southwest Pacific Basin. *Geophysical Research Letters*, *46*(5), 2662–2669. doi: 10.1029/2018GL081685

Johnston, T. M., & Rudnick, D. L. (2015). Trapped diurnal internal tides, propagating semidiurnal internal tides, and mixing estimates in the California Current System from sustained glider observations, 2006-2012. *Deep-Sea Research Part II: Topical Studies in Oceanography*, *112*, 61–78. doi: 10.1016/j.dsr2.2014.03.009

Jones, D. C., Holt, H. J., Meijers, A. J., & Shuckburgh, E. (2019). Unsupervised Clustering of Southern Ocean Argo Float Temperature Profiles. *Journal of Geophysical Research: Oceans*, *124*(1), 390–402. doi: 10.1029/2018JC014629

Kaiser, B. E., Saenz, J. A., Sonnewald, M., & Livescu, D. (2022). Automated identification of dominant physical processes. *Engineering Applications of Artificial Intelligence*, *116*, 105496.

Katsumata, K., Talley, L. D., Capuano, T. A., & Whalen, C. B. (2021). Spatial and Temporal Variability of Diapycnal Mixing in the Indian Ocean. *Journal of Geophysical Research: Oceans*, *126*(7), 1–27. doi: 10.1029/2021JC017257

Kawano, T., Aoyama, M., Joyce, T., Uchida, H., Takatsuki, Y., & Fukasawa, M. (2006). The latest batch-to-batch difference table of standard seawater and its application to the WOCE onetime sections. *Journal of Oceanography*, *62*, 777–792. doi: 10.1007/s10872-006-0097-8

Klymak, J. M., Pinkel, R., & Rainville, L. (2008). Direct Breaking of the Internal Tide near Topography: Kaena Ridge, Hawaii. *Journal of Physical Oceanography*, *38*, 380–399. doi: 10.1175/2007JPO3728.1

Konishi, S., Ando, T., & Imoto, S. (2004). Bayesian information criteria and smoothing parameter selection in radial basis function networks. *Biometrika*, *91*(1). doi: 10.1093/biomet/91.1.27

Kouketsu, S., Doi, T., Kawano, T., Masuda, S., Sugiura, N., Sasaki, Y., . . . Awaji, T. (2011). Deep ocean heat content changes estimated from observation and reanalysis product and their influence on sea level change. *Journal of Geophysical Research*, *116*(C3). doi: doi:10.1029/2010jc006464

Kouketsu, S., Fukasawa, M., Kaneko, I., Kawano, T., Uchida, H., Doi, T., . . . Murakami, K. (2009). Changes in water properties and transports along 24°N in the North pacific between 1985 and 2005. *Journal of Geophysical Research: Oceans*, *114*(C1). doi: 10.1029/2008JC004778

Kouketsu, S., Kawano, T., Masuda, S., Sugiura, N., Sasaki, Y., Toyoda, T., . . . others (2011). Deep ocean heat content changes estimated from observation and reanalysis product and their influence on sea level change. *J. Geophys. Res.*, *116*(C3).

Kunze, E. (2017a). The Internal-Wave-Driven Meridional Overturning Circulation. *Journal of Physical Oceanography*, *47*(11), 2673–2689. doi: 10.1175/JPO-D-16-0142.1

Kunze, E. (2017b). Internal-Wave-Driven Mixing: Global Geography and Budgets. *Journal of Physical Oceanography*, *47*(6), 1325–1345. Retrieved from http://journals.ametsoc.org/doi/10.1175/JPO-D-16-0141.1 doi: 10.1175/JPO-D-16-0141.1

Kunze, E., Firing, E., Hummon, J., Chereskin, T. K., & Thurnherr, A. (2006b). Global abyssal mixing inferred from lowered ADCP shear and CTD strain profiles. *Journal of Physical Oceanography*, *36*(8), 1553–1576.

Kunze, E., Firing, E., Hummon, J. M., Chereskin, T. K., & Thurnherr, A. M. (2006a). Global Abyssal Mixing Inferred from Lowered ADCP Shear and CTD Strain Profiles. *Journal of Physical Oceanography*, *36*(8), 1553–1576. doi: 10.1175/JPO2926.1

Kunze, E., Rosenfeld, L. K., Carter, G. S., & Gregg, M. (2002). Internal waves in Monterey Submarine Canyon. *Journal of Physical Oceanography*, *32*. doi: 10.1175/1520-0485(2002)032⟨1890:IWIMSC⟩2.0.CO;2

Kunze, E., & Toole, J. M. (1997). Tidally driven vorticity, diurnal shear, and turbulence atop Fieberling Seamount. *Journal of Physical Oceanography*, *27*. doi: 10.1175/1520-0485(1997)027⟨2663:TDVDSA⟩2.0.CO;2

Lago, V., & England, M. H. (2019). Projected slowdown of antarctic bottom water formation in response to amplified meltwater contributions. *Journal of Climate*, *615*. doi: 10.1175/JCLI-D-18-0622.1

Ledwell, J. R., Montgomery, E. T., Polzin, K. L., Laurent, L. C. S., Schmitt, R. W., & Toole, J. M.

(2000). Evidence for enhanced mixing over rough topography in the abyssal ocean. *Nature*, *403*, 179–182. doi: 10.1038/35003164

Ledwell, J. R., Watson, A. J., & Law, C. S. (1998a). Mixing of a tracer in the pycnocline. *Journal of Geophysical Research: Oceans*, *103*. doi: 10.1029/98JC01738

Ledwell, J. R., Watson, A. J., & Law, C. S. (1998b). Mixing of a tracer in the pycnocline. *J. Geophys. Res.*, *103*, 21499–21529.

Lee, D. D., & Seung, H. S. (1999). Learning the parts of objects by non-negative matrix factorization. *Nature*, *401*, 788–791. doi: 10.1038/44565

Lele, R., Purkey, S. G., Nash, J. D., Mackinnon, J. A., Thurnherr, A. M., Whalen, C. B., ... Talley, L. D. (2021). Abyssal Heat Budget in the Southwest Pacific Basin. *Journal of Physical Oceanography*, *51*(11), 3317–3333. doi: 10.1175/JPO-D-21-0045.1

Levitus, S., Antonov, J., & Boyer, T. (2005). Warming of the world ocean, 1955–2003. *Geophys. Res. Lett.*, *32*(2).

Levitus, S., Antonov, J. I., Boyer, T. P., Baranova, O. K., Garcia, H. E., Locarnini, R. A., ... Zweng, M. M. (2012). World ocean heat content and thermosteric sea level change (0–2000 m), 1955–2010. *Geophys. Res. Lett.*, *39*(10). doi: 10.1029/2012GL051106

Levitus, S., Antonov, J. I., Boyer, T. P., & Stephens, C. (2000). Warming of the world ocean. *Science*. doi: 10.1126/science.287.5461.2225

Li, Q., England, M. H., Hogg, A. M. C., Rintoul, S. R., & Morrison, A. K. (2023). Abyssal ocean overturning slowdown and warming driven by Antarctic meltwater. *Nature*, *615*. doi: 10.1038/s41586-023-05762-w

Liu, C., Liang, X., Chambers, D. P., & Ponte, R. M. (2020). Global Patterns of Spatial and Temporal Variability in Salinity from Multiple Gridded Argo Products. *Journal of Climate*, *33*(20), 8751–8766. doi: 10.1175/JCLI-D-20-0053.1

Llovel, W., & Lee, T. (2015). Importance and origin of halosteric contribution to sea level change in the southeast Indian Ocean during 2005–2013. , 1148–1157. doi: 10.1002/2014GL062611.Received

Llovel, W., Purkey, S., Meyssignac, B., Blazquez, A., Kolodziejczyk, N., & Bamber, J. (2019). Global ocean freshening , ocean mass increase and global mean sea level rise over 2005 – 2015. *Scientific Reports*, 1–10. Retrieved from http://dx.doi.org/10.1038/s41598-019-54239-2 doi: 10.1038/s41598-019-54239-2

Llovel, W., Willis, J. K., Landerer, F. W., & Fukumori, I. (2014). Deep-ocean contribution to sea

level and energy budget not detectable over the past decade. *Nature Climate Change*, *4*. doi: 10.1038/nclimate2387

Lueck, R. G., & Mudge, T. D. (2009). Seamount Topographically Induced Mixing Around a Shallow Seamount. , *1831*(1997). doi: 10.1126/science.276.5320.1831

Lumpkin, R., & Speer, K. (2007). Global Ocean Meridional Overturning. *Journal of Physical Oceanography*, *37*(10), 2550–2562. doi: 10.1175/JPO3130.1

Macdonald, A. M., Mecking, S., Robbins, P. E., Toole, J. M., Johnson, G. C., Talley, L. D., ... Wijffels, S. E. (2009). The WOCE-era 3-D Pacific Ocean circulation and heat budget. *Progress in Oceanography*, *82*(4), 281–325. Retrieved from http://dx.doi.org/10.1016/j.pocean.2009.08.002 doi: 10.1016/j.pocean.2009.08.002

MacKinnon, J. A., & Gregg, M. (2003). Mixing on the Late-Summer New England Shelf—Solibores, Shear, and Stratification. *Journal of Physical Oceanography*, *35*(12), 2408–2424. doi: 10.1175/1520-0485(2003)033⟨1476:motlne⟩2.0.co;2

MacKinnon, J. A., Zhao, Z., Whalen, C. B., Waterhouse, A. F., Trossman, D. S., Sun, O. M., ... Alford, M. H. (2017a). Climate process team on internal wave-driven ocean mixing. *Bulletin of the American Meteorological Society*, *98*(11), 2429–2454. doi: 10.1175/BAMS-D-16-0030.1

MacKinnon, J. A., Zhao, Z., Whalen, C. B., Waterhouse, A. F., Trossman, D. S., Sun, O. M., ... Alford, M. H. (2017b). Climate process team on internal wave driven ocean mixing. *Bulletin of the American Meteorological Society*, *98*(11), 2429-2454. Retrieved from https://doi.org/10.1175/BAMS-D-16-0030.1 doi: 10.1175/BAMS-D-16-0030.1

Marshall, J., & Speer, K. (2012). Closure of the meridional overturning circulation through Southern Ocean upwelling. *Nature Geoscience*, *5*(3), 171–180. doi: 10.1038/ngeo1391

Mashayek, A., Ferrari, R., Merrifield, S., Ledwell, J. R., St Laurent, L., & Garabato, A. C. (2017). Topographic enhancement of vertical turbulent mixing in the Southern Ocean. *Nature Communications*, *8*, 1–12. doi: 10.1038/ncomms14197

Mashayek, A., Reynard, N., Zhai, F., Srinivasan, K., Jelley, A., Naveira Garabato, A., & Caulfield, C. P. (2022). Deep ocean learning of small scale turbulence. *Geophysical Research Letters*, *49*(15), e2022GL098039.

Masuda, S., Awaji, T., Sugiura, N., Matthews, J. P., Toyoda, T., Kawai, Y., ... Fukasawa, M. (2010). Simulated rapid warming of abyssal North Pacific waters. *Science*, *329*(5989), 319–322. doi: 10.1126/science.1188703

Mater, B. D., Venayagamoorthy, S. K., Laurent, L. S., & Moum, J. N. (2015). Biases in Thorpe scale estimates of turbulence dissipation Part I: Assessments from large-scale overturns in

oceanographic data. *J. Phys. Oceanogr.*, *45*(2015), 2497–2521.

Maze, G., Mercier, H., Fablet, R., Tandeo, P., Lopez Radcenco, M., Lenca, P., . . . Le Goff, C. (2017). Coherent heat patterns revealed by unsupervised classification of Argo temperature profiles in the North Atlantic Ocean. *Progress in Oceanography*, *151*. doi: 10.1016/j.pocean.2016.12.008

Mazloff, M. R., Heimbach, P., & Wunsch, C. (2010). An eddy-permitting Southern Ocean state estimate. *Journal of Physical Oceanography*, *40*(5), 880–899. doi: 10.1175/2009JPO4236.1

McComas, C. H., & Müller, P. (1981). The dynamic balance of internal waves. *Journal of Physical Oceanography*, *11*(7), 970–986. doi: 10.1175/1520-0485(1981)011⟨0970:TDBOIW⟩2.0.CO;2

McDougall, P., Trevor J. ; Barker. (2011). Getting started with TEOS-10 and the Gibbs Seawater (GSW) Oceanographic Toolbox. *Scor/Iapso Wg127*.

Meehl, G. A., Washington, W. M., Santer, B. D., Collins, W. D., Arblaster, J. M., Hu, A., . . . Strand, W. G. (2006). Climate change projections for the twenty-first century and climate change commitment in the CCSM3. *Journal of Climate*, *19*(11), 2597–2616. doi: 10.1175/JCLI3746.1

Melet, A., Hallberg, R., Legg, S., & Nikurashin, M. (2014). Sensitivity of the ocean state to lee wave-driven mixing. *Journal of Physical Oceanography*, *44*(3), 900–921. doi: 10.1175/JPO-D-13-072.1

Melet, A., Hallberg, R., Legg, S., & Polzin, K. (2013a). Sensitivity of the ocean state to the vertical distribution of internal-tide-driven mixing. *Journal of Physical Oceanography*, *43*(3), 602–615. Retrieved from http://journals.ametsoc.org/doi/abs/10.1175/JPO-D-12-055.1 doi: 10.1175/JPO-D-12-055.1

Melet, A., Hallberg, R., Legg, S., & Polzin, K. L. (2013b). Sensitivity of the ocean state to the vertical distribution of internal-tide-driven mixing. *J. Phys. Oceanogr.*, *43*(3), 602-615. doi: http://dx.doi.org/10.1175/JPO-D-12-055.1

Melet, A., Legg, S., & Hallberg, R. (2016). Climatic impacts of parameterized local and remote tidal mixing. *Journal of Climate*, *29*(10), 3473–3500. doi: 10.1175/JCLI-D-15-0153.1

Meyer et al. (2014). *Climate Change 2014*.

Morris, M. Y., Hall, M. M., St. Laurent, L. C., & Hogg, N. G. (2001). Abyssal Mixing in the Brazil Basin. *Journal of Physical Oceanography*, *31*(11), 3331–3348. doi: https://doi.org/10.1175/1520-0485(2001)031{\%}3C3331:AMITBB{\%}3E2.0.CO;2

Moum, J., Gregg, M., Lien, R., & Carr, M. (1995). Comparison of turbulence kinetic energy dissipation rate estimates from two ocean microstructure profilers. *Journal of Atmospheric and Oceanic Technology*, *12*(2), 346-366.

Moum, J., & Nash, J. (2009). Mixing measurements on an equatorial ocean mooring. *J. Atmos. Ocean. Tech.*, *26*, 317–336.

Moum, J. N. (2015). Ocean speed and turbulence measurements using pitot-static tubes on moorings. *Journal of Atmospheric and Oceanic Technology*, *32*, 1400–1413.

Moum, J. N., & Nash, J. D. (2009). Mixing Measurements on an Equatorial Ocean Mooring. *Journal of Atmospheric and Oceanic Technology*, *26*(2), 317–336. doi: 10.1175/2008JTECHO617.1

Muench, R., Padman, L., Gordon, A., & Orsi, A. (2009). A dense water outflow from the ross sea, antarctica: Mixing and the contribution of tides. *Journal of Marine Systems*, *77*(4), 369–387.

Müller, P., & Liu, X. (2000). Scattering of internal waves at finite topography in two dimensions. Part I: Theory and case studies. *Journal of Physical Oceanography*, *30*, 532–549. doi: 10.1175/1520-0485(2000)030⟨0532:SOIWAF⟩2.0.CO;2

Munk, W. (1966). Abyssal recipes. *Deep-Sea Research and Oceanographic Abstracts*. doi: 10.1016/0011-7471(66)90602-4

Munk, W. (1981). Internal Waves and Small-Scale Processes. In *Evolution of physical oceanography: Scientific surveys in honor of henry stommel.*

Munk, W., & Wunsch, C. (1998a). Abyssal recipes II: Energetics of tidal and wind mixing. *Deep-Sea Research Part I: Oceanographic Research Papers*. doi: 10.1016/S0967-0637(98)00070-3

Munk, W., & Wunsch, C. (1998b). Abyssal recipes II: energetics of tidal and wind mixing. *Deep-Sea Res. Part I*, *45*, 1977-2010.

Nash, J., & Moum, J. (1999). Estimating salinity variance dissipation rate from conductivity microstructure measurements. *J. Atmos. Ocean. Tech.*, *16*, 263-274.

Nash, J. D., Caldwell, D. R., Zelman, M. J., & Moum, J. N. (1999, November). A thermocouple probe for high-speed temperature measurement in the ocean. *Journal of Atmospheric and Oceanic Technology*, *16*, 1474–1482.

Nash, J. D., & Moum, J. N. (2002). Microstructure estimates of turbulent salinity flux and the dissipation spectrum of salinity. *J. Phys. Oceanogr.*, *32*, 2312–2334.

Naveira, A. C., Frajka-Williams, E., Spingys, C. P., Legg, S., Polzin, K. L., Naveira Garabato,

A. C., . . . Meredith, M. P. (2019). Rapid mixing and exchange of deep-ocean waters in an abyssal boundary current. *Proceedings of the National Academy of Sciences of the United States of America*, *116*(27), 13233–13238. doi: 10.1073/pnas.1904087116

Naveira Garabato, A. C., Polzin, K. L., King, B. A., Heywood, K. J., & Visbeck, M. (2004). Widespread Intense Turbulent Mixing in the Southern Ocean. *Science*, *303*, 210–213. doi: 10.1126/science.1090929

Nerem, R. S., Beckley, B. D., Fasullo, J. T., Hamlington, B. D., Masters, D., & Mitchum, G. T. (2018). Climate-change–driven accelerated sea-level rise detected in the altimeter era. *Proceedings of the National Academy of Sciences of the United States of America*, *115*(9). doi: 10.1073/pnas.1717312115

Nikurashin, M., & Ferrari, R. (2010). Radiation and dissipation of internal waves generated by geostrophic motions impinging on small-scale topography: Application to the southern ocean. *Journal of Physical Oceanography*, *40*, 1055–1074. doi: 10.1175/2010JPO4315.1

Nikurashin, M., & Ferrari, R. (2011). Global energy conversion rate from geostrophic flows into internal lee waves in the deep ocean. *Geophysical Research Letters*, *38*. doi: 10.1029/2011GL046576

Nikurashin, M., & Ferrari, R. (2013). Overturning circulation driven by breaking internal waves in the deep ocean. *Geophysical Research Letters*, *40*(12), 3133–3137. doi: 10.1002/grl.50542

Nikurashin, M., Ferrari, R., Grisouard, N., & Polzin, K. L. (2014). The impact of finite-amplitude bottom topography on internal wave generation in the Southern Ocean. *Journal of Physical Oceanography*, *44*. doi: 10.1175/JPO-D-13-0201.1

Nycander, J. (2005). Generation of internal waves in the deep ocean by tides. *Journal of Geophysical Research: Oceans*, *110*. doi: 10.1029/2004JC002487

Oakey, N. S. (1982a). Determination of the rate of dissipation of turbulent energy from simultaneous temperature and velocity shear microstructure measurements. *J. Phys. Oceanogr.*, *12*, 256–271.

Oakey, N. S. (1982b). Determination of the Rate of Dissipation of Turbulent Energy from Simultaneous Temperature and Velocity Shear Microstructure Measurements. *Journal of Physical Oceanography*, *12*, 256–271. doi: 10.1175/1520-0485(1982)012⟨0256:dotrod⟩2.0.co;2

Oka, A., & Niwa, Y. (2013). Pacific deep circulation and ventilation controlled by tidal mixing away from the sea bottom. *Nature Communications*, *4*. doi: 10.1038/ncomms3419

Osborn, T. R. (1974). Vertical profiling of velocity microstructure. *J. Phys. Oceanogr.*, *4*,

109–115.

Osborn, T. R. (1980a). Estimates of the Local Rate of Vertical Diffusion from Dissipation Measurements. *Journal of Physical Oceanography*, *10*(1), 83–89. doi: 10.1175/1520-0485(1980)010{\%}3C0083:EOTLRO{\%}3E2.0.CO;2

Osborn, T. R. (1980b). Estimates of the local rate of vertical diffusion from dissipation measurements. *J. Phys. Oceanogr.*, *10*, 83–89.

Osborn, T. R., & Cox, C. S. (1972a). Oceanic fine structure. *Geophysical & Astrophysical Fluid Dynamics*, *3*(4), 321–345. doi: 10.1080/03091927208236085

Osborn, T. R., & Cox, C. S. (1972b). Oceanic fine structure. *Geophys. Fluid Dyn.*, *3*, 321–345.

Pedregosa, F., Varoquaux, G., Gramfort, A., Michel, V., Thirion, B., Grisel, O., . . . Duchesnay, (2011). Scikit-learn: Machine learning in Python. *Journal of Machine Learning Research*, *12*, 2825–2830.

Perlin, A., & Moum, J. (2012). Comparison of thermal variance dissipation rates from moored and profiling instruments at the equator. *Journal of Atmospheric and Oceanic Technology*, *29*(9), 1347–1362.

Pollmann, F. (2020). Global characterization of the ocean's internal wave spectrum. *Journal of Physical Oceanography*, *50*(7), 1871–1891. doi: 10.1175/JPO-D-19-0185.1

Polzin, K. L., & Ferrari, R. (2004). Isopycnal dispersion in NATRE. *Journal of Physical Oceanography*, *34*. doi: 10.1175/1520-0485(2004)034⟨0247:IDIN⟩2.0.CO;2

Polzin, K. L., Kunze, E., Toole, J. M., & Schmitt, R. W. (2003). The partition of finescale energy into internal waves and subinertial motions. *Journal of Physical Oceanography*, *33*. doi: 10.1175/1520-0485(2003)033⟨0234:TPOFEI⟩2.0.CO;2

Polzin, K. L., & Lvov, Y. (2011). Towards Regional Characterization of the Oceanic Internal Wavefield. *Reviews of Geophysics*, *49*. doi: 10.1029/2010RG000329

Polzin, K. L., Naveira Garabato, A. C., Huussen, T. N., Sloyan, B. M., & Waterman, S. (2014a). Finescale parameterizations of turbulent dissipation. *Journal of Geophysical Research: Oceans*, *119*(2), 1383–1419. doi: 10.1002/2013JC008979

Polzin, K. L., Naveira Garabato, A. C., Huussen, T. N., Sloyan, B. M., & Waterman, S. (2014b). Finescale parameterizations of turbulent dissipation. *Journal of Geophysical Research: Oceans*, *119*(2), 1383–1419. Retrieved from http://dx.doi.org/10.1002/2013JC008979 doi: 10.1002/2013JC008979

Polzin, K. L., Toole, J. M., Ledwell, J. R., & Schmitt, R. W. (1997). Spatial variability of turbulent mixing in the abyssal ocean. *Science*, *276*(5309), 93–96. doi: 10.1126/science.276.5309.93

Polzin, K. L., Toole, J. M., & Schmitt, R. W. (1995). Finescale Parameterizations of Turbulent Dissipation. *Journal of Physical Oceanography*, *25*(3), 306–328. doi: https://doi.org/10.1175/1520-0485(1995)025⟨0306:FPOTD⟩2.0.CO;2

Purkey, S. G., & Johnson, G. C. (2010). Warming of Global Abyssal and Deep Southern Ocean Waters between the 1990s and 2000s: Contributions to Global Heat and Sea Level Rise Budgets. *J. Climate*, *23*, 6336–6351. doi: 10.1175/20

Purkey, S. G., & Johnson, G. C. (2012a). Global contraction of Antarctic Bottom Water between the 1980s and 2000s. *Journal of Climate*, *25*(17), 5830–5844. doi: 10.1175/JCLI-D-11-00612.1

Purkey, S. G., & Johnson, G. C. (2012b). Global Contraction of Antarctic Bottom Water between the 1980s and 2000s. *J. Climate*, *25*, 5830–5844.

Purkey, S. G., & Johnson, G. C. (2013). Antarctic Bottom Water warming and freshening: Contributions to sea level rise, ocean freshwater budgets, and global heat gain*. *Journal of Climate*. doi: 10.1175/JCLI-D-12-00834.1

Purkey, S. G., Johnson, G. C., & Chambers, D. P. (2014). Relative contributions of ocean mass and deep steric changes to sea level rise between 1993 and 2013. *Journal of Geophysical Research: Oceans*, *119*(11). doi: 10.1002/2014JC010180

Purkey, S. G., Johnson, G. C., Talley, L. D., Sloyan, B. M., Wijffels, S. E., Smethie, W., ... Katsumata, K. (2019). Unabated Bottom Water Warming and Freshening in the South Pacific Ocean. *Journal of Geophysical Research: Oceans*, *124*(3), 1778–1794. doi: 10.1029/2018JC014775

Reid, J. L. (1997). On the total geostrophic circulation of the Pacific Ocean: Flow patterns, tracers, and transports. *Progress in Oceanography*, *39*(4), 263–352.

Riser, S. C., Freeland, H. J., Roemmich, D., Wijffels, S., Troisi, A., Belbéoch, M., ... Jayne, S. R. (2016). *Fifteen years of ocean observations with the global Argo array.* doi: 10.1038/nclimate2872

Roemmich, D., Alford, M. H., Claustre, H., Johnson, K. S., King, B., Moum, J., ... Yasuda, I. (2019). On the future of Argo: A global, full-depth, multi-disciplinary array. *Frontiers in Marine Science*, *6*, 439. doi: 10.3389/fmars.2019.00439

Roemmich, D., & Gilson, J. (2009). The 2004-2008 mean and annual cycle of temperature, salinity, and steric height in the global ocean from the Argo Program. *Progress in Oceanography*, *82*. doi: 10.1016/j.pocean.2009.03.004

Roemmich, D., Hautala, S., & Rudnick, D. (1996). Northward abyssal transport through the Samoan passage and adjacent regions. *Journal of Geophysical Research C: Oceans*, *101*(C6), 14039–14055. doi: 10.1029/96JC00797

Roemmich, D., John Gould, W., & Gilson, J. (2012). 135 years of global ocean warming between the Challenger expedition and the Argo Programme. *Nature Climate Change*, *2*. doi: 10.1038/nclimate1461

Rosso, I., Mazloff, M. R., Talley, L. D., Purkey, S. G., Freeman, N. M., & Maze, G. (2020). Water Mass and Biogeochemical Variability in the Kerguelen Sector of the Southern Ocean: A Machine Learning Approach for a Mixing Hot Spot. *Journal of Geophysical Research: Oceans*, *125*(3), 1–23. doi: 10.1029/2019JC015877

Rousseeuw, P. J. (1987). Silhouettes: A graphical aid to the interpretation and validation of cluster analysis. *Journal of Computational and Applied Mathematics*, *20*, 53–65. doi: 10.1016/0377-0427(87)90125-7

Ruddick, B., Anis, A., & Thompson, K. (2000). Maximum likelihood spectral fitting: The Batchelor spectrum. *J. Atmos. Ocean. Tech.*, *17*, 1541-1555.

Rudnick, D. L. (1997). Direct velocity measurements in the Samoan Passage. *Journal of Geophysical Research C: Oceans*, *102*(C2), 3293–3302. doi: 10.1029/96JC03286

Rudnick, D. L., Johnston, T. M., & Sherman, J. T. (2013). High-frequency internal waves near the Luzon Strait observed by underwater gliders. *Journal of Geophysical Research: Oceans*, *118*. doi: 10.1002/jgrc.20083

Schwarz G. (1978). Estimating the dimension of a model. *The annals of statistics*, *6*(2).

Scott, R. B., Goff, J. A., Naveira Garabato, A. C., & Nurser, A. J. (2011). Global rate and spectral characteristics of internal gravity wave generation by geostrophic flow over topography. *Journal of Geophysical Research: Oceans*, *116*. doi: 10.1029/2011JC007005

Scotti, A. (2015). Biases in Thorpe scale estimates of turbulence dissipation Part II: Energetics arguments and turbulence simulations. *J. Phys. Oceanogr.*, *45*(2015), 2522–2543.

Shcherbina, A. Y., D'Asaro, E. A., & Nylund, S. (2018). Observing finescale oceanic velocity structure with an autonomous Nortek acoustic Doppler current profiler. *Journal of Atmospheric and Oceanic Technology*, *35*(2), 411-427. Retrieved from https://doi.org/10.1175/JTECH-D-17-0108.1 doi: 10.1175/JTECH-D-17-0108.1

Shroyer, E. L., Rudnick, D. L., Farrar, J. T., Lim, B., Venayagamoorthy, S. K., Laurent, L. C., ... Moum, J. N. (2016). Modification of upper-ocean temperature structure by subsurface mixing in the presence of strong salinity stratification. *Oceanography*, *29*(2), 62–71. doi:

10.5670/oceanog.2016.39

Simmons, H. L., & Alford, M. H. (2012). Simulating the long-range swell of internal waves generated by ocean storms. *Oceanography*, *25*. doi: 10.5670/oceanog.2012.39

Sloyan, B. M., Wijffels, S. E., Tilbrook, B., Katsumata, K., Murata, A., & Macdonald, A. M. (2013). Deep Ocean Changes near the Western Boundary of the South Pacific Ocean. *Journal of Physical Oceanography*, *43*(10), 2132–2141. doi: 10.1175/JPO-D-12-0182.1

Smeed, D. A., McCarthy, G. D., Cunningham, S. A., Frajka-Williams, E., Rayner, D., Johns, W. E., ... Bryden, H. L. (2014). *Observed decline of the Atlantic meridional overturning circulation 2004-2012.* doi: 10.5194/os-10-29-2014

Smyth, W. D. (1999). Dissipation-range geometry and scalar spectra in sheared stratified turbulence. *J. Fluid Mech.*, *401*, 209–242.

Sonnewald, M., Sonnewald, M., Dutkiewicz, S., Hill, C., & Forget, G. (2020). Elucidating ecological complexity: Unsupervised learning determines global marine eco-provinces. *Science Advances*, *6*(22). doi: 10.1126/sciadv.aay4740

Sonnewald, M., Wunsch, C., & Heimbach, P. (2019). Unsupervised Learning Reveals Geography of Global Ocean Dynamical Regions. *Earth and Space Science*, *6*. doi: 10.1029/2018EA000519

Spingys, C. P., Naveira Garabato, A. C., Legg, S., Polzin, K. L., Abrahamsen, E. P., Buckingham, C. E., ... Frajka-Williams, E. (2021). Mixing and Transformation in a Deep Western Boundary Current: A Case Study. *Journal of Physical Oceanography*, *51*(4), 1205–1222. doi: 10.1175/jpo-d-20-0132.1

Sreenivasan, K. R. (1996). The passive scalar spectrum and the Obukhov-Corrsin constant. *Phys. Fluids*, **8**(1), 189–196.

Stammer, D., & Cazenave, A. (2017). *Satellite altimetry over oceans and land surfaces*. doi: 10.1201/9781315151779

Stanley, G. J., & Saenko, O. A. (2014). Bottom-enhanced diapycnal mixing driven by Mesoscale Eddies: Sensitivity to wind energy supply. *Journal of Physical Oceanography*, *44*. doi: 10.1175/JPO-D-13-0116.1

Steiner, A. K., Ladstädter, F., Randel, W. J., Maycock, A. C., Fu, Q., Claud, C., ... Zou, C. Z. (2020). Observed temperature changes in the troposphere and stratosphere from 1979 to 2018. *Journal of Climate*. doi: 10.1175/JCLI-D-19-0998.1

St. Laurent, L. C., Naveira Garabato, A. C., Ledwell, J. R., Thurnherr, A. M., Toole, J. M., &

Watson, A. J. (2012). Turbulence and diapycnal mixing in drake passage. *Journal of Physical Oceanography*, *42*, 2143–2152. doi: 10.1175/JPO-D-12-027.1

St. Laurent, L. C., Toole, J. M., & Schmitt, R. W. (2001). Buoyancy forcing by turbulence above rough topography in the abyssal Brazil Basin. *Journal of Physical Oceanography*, *31*. doi: 10.1175/1520-0485(2001)031⟨3476:BFBTAR⟩2.0.CO;2

Sverdrup, H. U. (1933). On vertical circulation in the ocean due to the action of the wind with application to conditions within the Antarctic Circumpolar Current. *Discovery Reports*, *VII*.

Takahashi, A., & Hibiya, T. (2018). Assessment of Finescale Parameterizations of Deep Ocean Mixing in the Presence of Geostrophic Current Shear : Results of Microstructure Measurements in the Antarctic Circumpolar Current Region. , 135–153. doi: 10.1029/2018JC014030

Talley, L. D. (2003). Shallow, intermediate, and deep overturning components of the global heat budget. *Journal of Physical Oceanography*. doi: 10.1175/1520-0485(2003)033⟨0530:SIADOC⟩2.0.CO;2

Talley, L. D. (2013). Closure of the global overturning circulation through the Indian, Pacific, and southern oceans. *Oceanography*, *26*(1), 80–97. doi: 10.5670/oceanog.2013.07

Talley, L. D., Feely, R., Sloyan, B., Wanninkhof, R., Baringer, M., Bullister, J., . . . Zhang, J.-Z. (2016). Changes in Ocean Heat, Carbon Content, and Ventilation: A Review of the First Decade of GO-SHIP Global Repeat Hydrography. *Annual Review of Marine Science*. doi: 10.1146/annurev-marine-052915-100829

Talley, L. D., Pickard, G. L., Emery, W. J., & Swift, J. H. (2011). Pacific Ocean. *Descriptive Physical Oceanography*, 303–362. Retrieved from http://linkinghub.elsevier.com/retrieve/pii/B9780750645522100101 doi: 10.1016/B978-0-7506-4552-2.10022-8

Talley, L. D., Sparrow, M., Chapman, P., & Gould, J. (2007). *Hydrographic Atlas of the World Ocean Circulation Experiment (WOCE). Volume 2: Pacific Ocean*.

Tapley, B. D., Bettadpur, S., Ries, J. C., Thompson, P. F., & Watkins, M. M. (2004). GRACE measurements of mass variability in the Earth system. *Science*. doi: 10.1126/science.1099192

Tapley, B. D., Watkins, M. M., Flechtner, F., Reigber, C., Bettadpur, S., Rodell, M., . . . Velicogna, I. (2019). Contributions of GRACE to understanding climate change. *Nature Climate Change*, *9*(5), 358–369. Retrieved from http://dx.doi.org/10.1038/s41558-019-0456-2 doi: 10.1038/s41558-019-0456-2

Tatebe, H., Tanaka, Y., Komuro, Y., & Hasumi, H. (2018). Impact of deep ocean mixing on the climatic mean state in the Southern Ocean. *Scientific Reports*, *8*. doi: 10.1038/s41598-018-32768-6

Thorpe, S. (1977). Turbulence and mixing in a Scottish Loch. *Philos. Trans. R. Soc. London Ser. A*, *286*, 125-181.

Thurnherr, A. M. (2011). Vertical velocity from LADCP data. In *2011 ieee/oes/cwtm 10th working conference on current, waves and turbulence measurement, cwtm 2011.* doi: 10.1109/CWTM.2011.5759552

Thurnherr, A. M., Kunze, E., Toole, J. M., St. Laurent, L., Richards, K. J., & Ruiz-Angulo, A. (2015a). Vertical kinetic energy and turbulent dissipation in the ocean. *Geophysical Research Letters*, *42*(18), 7639–7647. doi: 10.1002/2015GL065043

Thurnherr, A. M., Kunze, E., Toole, J. M., St. Laurent, L., Richards, K. J., & Ruiz-Angulo, A. (2015b). Vertical kinetic energy and turbulent dissipation in the ocean. *Geophys. Res. Lett.*. doi: 10.1002/2015GL065043

Thurnherr, A. M., Visbeck, M., Firing, E., King, B. A., Hummon, J., Krahmann, G., & Huber, B. A. (2010). A Manual For Acquiring Lowered Doppler Current Profiler Data. *The GO-SHIP Repeat Hydrographic Manual: A Collection of Expert Reports and Guidelines*, *14*(134).

Toggweiler, J. R. (1994). The Ocean's Overturning Circulation. *Physics Today*, *47*. doi: 10.1063/1.881425

Toggweiler, J. R., & Samuels, B. (1995). Effect of drake passage on the global thermohaline circulation. *Deep-Sea Research Part I*, *42*. doi: 10.1016/0967-0637(95)00012-U

Toggweiler, J. R., & Samuels, B. (1998). On the ocean's large-scale circulation near the limit of no vertical mixing. *Journal of Physical Oceanography*, *28*. doi: 10.1175/1520-0485(1998)028⟨1832:OTOSLS⟩2.0.CO;2

Tomczak, M., & Godfrey, J. S. (1994). Temperature, salinity, density and the oceanic pressure field. In *Regional oceanography.* doi: 10.1016/b978-0-08-041021-0.50006-0

Trenberth, K. E., & Fasullo, J. T. (2009). Changes in the flow of energy through the Earth's climate system. *Meteorologische Zeitschrift*, *18*. doi: 10.1127/0941-2948/2009/0388

Trenberth, K. E., Fasullo, J. T., & Balmaseda, M. A. (2014). Earth's energy imbalance. *Journal of Climate*, *27*. doi: 10.1175/JCLI-D-13-00294.1

Visbeck, M. (2002). Deep velocity profiling using lowered acoustic Doppler current profilers: Bottom track and inverse solutions. *Journal of Atmospheric and Oceanic Technology*, *19*(5), 794–807. doi: 10.1175/1520-0426(2002)019⟨0794:DVPULA⟩2.0.CO;2

Voet, G., Alford, M. H., Girton, J. B., Carter, G. S., Mickett, J. B., & Klymak, J. M. (2016). Warming and weakening of the abyssal flow through Samoan Passage. *Journal of Physical*

Oceanography, *46*(8), 2389–2401. doi: 10.1175/JPO-D-16-0063.1

von Schuckmann, K., Minière, A., Gues, F., Cuesta-Valero, F. J., Kirchengast, G., Adusumilli, S., ... Zemp, M. (2022). *Heat stored in the Earth system 1960-2020: Where does the energy go?* World Data Center for Climate (WDCC) at DKRZ. Retrieved from https://www.wdc-climate.de/ui/entry?acronym=GCOS_EHI_1960-2020

Von Schuckmann, K., Palmer, M. D., Trenberth, K. E., Cazenave, A., Chambers, D. P., Champollion, N., ... Wild, M. (2016). *An imperative to monitor Earth's energy imbalance.* doi: 10.1038/nclimate2876

Wang, Z., DiMarco, S. F., & Socolofsky, S. A. (2016). Turbulence measurements in the northern gulf of mexico: Application to the deepwater horizon oil spill on droplet dynamics. *Deep Sea Research Part I: Oceanographic Research Papers*, *109*, 40–50.

Warner, S. J., Holmes, R. M., M. Hawkins, E. H., S. Hoecker-Martínez, M., Savage, A. C., & Moum, J. N. (2018). Buoyant gravity currents released from tropical instability waves. *Journal of Physical Oceanography*, *48*(2), 361-382. Retrieved from https://doi.org/10.1175/JPO-D-17-0144.1 doi: 10.1175/JPO-D-17-0144.1

Waterhouse, A. F., MacKinnon, J. A., Nash, J. D., Alford, M. H., Kunze, E., Simmons, H. L., ... Lee, C. M. (2014a). Global patterns of diapycnal mixing from measurements of the turbulent dissipation rate. *Journal of Physical Oceanography*, *44*(7), 1854–1872. doi: 10.1175/JPO-D-13-0104.1

Waterhouse, A. F., MacKinnon, J. A., Nash, J. D., Alford, M. H., Kunze, E., Simmons, H. L., ... Lee, C. M. (2014b, November). Global patterns of diapycnal mixing from measurements of the turbulent dissipation rate. *J. Phys. Oceanogr.*, *44*(7), 1854–1872.

Waterman, S., Naveira Garabato, A. C., & Polzin, K. L. (2013). Internal waves and turbulence in the antarctic circumpolar current. *Journal of Physical Oceanography*, *43*(2), 259–282. Retrieved from http://journals.ametsoc.org/doi/abs/10.1175/JPO-D-11-0194.1 doi: 10.1175/JPO-D-11-0194.1

Waterman, S., Polzin, K. L., Naveira Garabato, A. C., Sheen, K. L., & Forryan, A. (2014, 2014/05/02). Suppression of internal wave breaking in the antarctic circumpolar current near topography. *Journal of Physical Oceanography*, *44*(5), 1466–1492. doi: 10.1175/JPO-D-12-0154.1

Waterman, S., Polzin, K. L., Naveira Garabato, A. C., Sheen, K. L., Forryan, A., Garabato, A. C., ... Forryan, A. (2014). Suppression of internal wave breaking in the antarctic circumpolar current near topography. *Journal of Physical Oceanography*, *44*(5), 1466–1492. doi: 10.1175/JPO-D-12-0154.1

Watkins, M. M., Wiese, D. N., Yuan, D. N., Boening, C., & Landerer, F. W. (2015). Improved methods for observing Earth's time variable mass distribution with GRACE using spherical cap mascons. *Journal of Geophysical Research: Solid Earth*. doi: 10.1002/2014JB011547

Watson, C. S., White, N. J., Church, J., King, M. A., Burgette, R. J., & Legresy, B. (2015). Unabated global mean sea-level rise over the satellite altimeter era. *Nature Climate Change*, *5*. doi: 10.1038/nclimate2635

Whalen, C. B. (2021). Best Practices for Comparing Ocean Turbulence Measurements Across Spatiotemporal Scales. *Journal of Atmospheric & Oceanic Technology*, *38*(4), 837–841. doi: https://doi.org/10.1175/JTECH-D-20-0175.1

Whalen, C. B., MacKinnon, J. A., & Talley, L. D. (2018a). Large-scale impacts of the mesoscale environment on mixing from wind-driven internal waves. *Nature Geoscience*, *11*(11), 842–847.

Whalen, C. B., MacKinnon, J. A., & Talley, L. D. (2018b). Large-scale impacts of the mesoscale environment on mixing from wind-driven internal waves. *Nature Geoscience*, *11*(11), 842–847. Retrieved from http://dx.doi.org/10.1038/s41561-018-0213-6 doi: 10.1038/s41561-018-0213-6

Whalen, C. B., MacKinnon, J. A., Talley, L. D., & Waterhouse, A. F. (2015a). Estimating the Mean Diapycnal Mixing Using a Finescale Strain Parameterization. *Journal of Physical Oceanography*, *45*(4), 1174–1188. doi: 10.1175/JPO-D-14-0167.1

Whalen, C. B., MacKinnon, J. A., Talley, L. D., & Waterhouse, A. F. (2015b, 2015/05/13). Estimating the mean diapycnal mixing using a finescale strain parameterization. *Journal of Physical Oceanography*, *45*(4), 1174–1188. Retrieved from http://dx.doi.org/10.1175/JPO-D-14-0167.1 doi: 10.1175/JPO-D-14-0167.1

Whalen, C. B., Naveira Garabato, A. C., Klymak, J. M., MacKinnon, J. A., Sheen, K. L., de Lavergne, C., ... Sheen, K. L. (2020). Internal wave-driven mixing: governing processes and consequences for climate. *Nature Reviews Earth and Environment*. Retrieved from http://dx.doi.org/10.1038/s43017-020-0097-z doi: 10.1038/s43017-020-0097-z

Whalen, C. B., Talley, L. D., & MacKinnon, J. A. (2012). Spatial and temporal variability of global ocean mixing inferred from Argo profiles. *Geophysical Research Letters*, *39*(17), 1–6. doi: 10.1029/2012GL053196

Whalen, C. B., Talley, L. D., & MacKinnon, J. A. (2012). Spatial and temporal variability of global ocean mixing inferred from argo profiles. *Geophys. Res. Lett.*, *39*(L18612), doi:10.1029/2012GL053196.

WHITEHEAD, J. A. J., & WORTHINGTON, L. V. (1982). The flux and mixing rates of Antarctic bottom water within the North Atlantic. *J Geophys Res*, *87*(C10), 7903–7924. Retrieved from

http://www.scopus.com/inward/record.url?eid=2-s2.0-0020179346&partnerID=tZOtx3y1 doi: 10.1029/jc087ic10p07903

Whitworth, T., Warren, B. A., Nowlin, W. D., Rutz, S. B., Pillsbury, R. D., & Moore, M. I. (1999). On the deep western-boundary current in the Southwest Pacific Basin. *Progress in Oceanography*, *43*(1), 1–54. doi: 10.1016/S0079-6611(99)00005-1

Wiese, D. N., Landerer, F. W., & Watkins, M. M. (2016). Quantifying and reducing leakage errors in the JPL RL05M GRACE mascon solution. *Water Resources Research*, *52*. doi: 10.1002/2016WR019344

Wijffels, S. E., Toole, J. M., & Davis, R. (2001). Revisiting the South Pacific subtropical circulation: A synthesis of World Ocean Circulation Experiment observations along 32°S. *Journal of Geophysical Research: Oceans*, *106*(C9), 19481–19513. Retrieved from http://doi.wiley.com/10.1029/1999JC000118 doi: 10.1029/1999jc000118

Wong, A. P., Wijffels, S. E., Riser, S. C., Pouliquen, S., Hosoda, S., Roemmich, D., . . . Park, H. M. (2020). *Argo Data 1999–2019: Two Million Temperature-Salinity Profiles and Subsurface Velocity Observations From a Global Array of Profiling Floats.* doi: 10.3389/fmars.2020.00700

Wright, C. J., Scott, R. B., Ailliot, P., & Furnival, D. (2014). Lee wave generation rates in the deep ocean. *Geophysical Research Letters*, *41*. doi: 10.1002/2013GL059087

Wunsch, C. (1996). *The Ocean Circulation Inverse Problem*. doi: 10.1017/cbo9780511629570

Wunsch, C., & Ferrari, R. (2004). Vertical mixing, energy, and the general circulation of the oceans. *Annual Review of Fluid Mechanics*, *36*(1), 281–314. Retrieved from http://arjournals.annualreviews.org/doi/abs/10.1146%2Fannurev.fluid.36.050802.122121 doi: 10.1146/annurev.fluid.36.050802.122121

Zhang, H. J., Whalen, C. B., Kumar, N., & Purkey, S. G. (2020). Abyssal Stratification Change in the Southwest Pacific Basin. *Earth and Space Science Open Archive*. doi: 10.1002/essoar.10503674.1

Zhu, Y., & Zhang, R. H. (2019). A modified vertical mixing parameterization for its improved ocean and coupled simulations in the tropical pacific. *Journal of Physical Oceanography*, *49*. doi: 10.1175/JPO-D-18-0100.1